Monocytic niches enable *Mycobacterium Tuberculosis* Persistence in Lymph Nodes

Elya Shamskhou

A dissertation submitted in partial fulfillment

of the requirements for the degree of

Doctor of Philosophy

University of Washington

2026

Reading Committee:

Michael Y. Gerner, Co-chair

Kevin B. Urdahl, Co-chair

Adam Lacey-Hulbert

Chetan Seshadri

Program Authorized to Offer Degree:

Immunology

University of Washington

Abstract

Monocytic niches enable *Mycobacterium Tuberculosis* Persistence in Lymph Nodes

Elya Shamskhou

Co-chairs of the Supervisory Committee:

Michael Y. Gerner

Kevin B. Urdahl

Department of Immunology

Tuberculosis remains a leading cause of infectious mortality worldwide, in part due to the ability of *Mycobacterium tuberculosis* (Mtb) to persist within host tissues despite robust immune activation. While pulmonary infection has historically dominated studies of tuberculosis pathogenesis, emerging evidence suggests that lymphoid tissues play a critical role in shaping disease outcome. This dissertation investigates the lung-draining mediastinal lymph node (medLN) as a central and underappreciated site of Mtb persistence, addressing the paradox that the medLN serves as both the primary site of adaptive immune priming and a long-term bacterial reservoir.

Using complementary approaches including mouse infection models, multiparameter confocal microscopy, flow cytometry, single-cell transcriptomics, and mathematical modeling, this work defines the cellular and spatial mechanisms that enable Mtb survival within the medLN. We identify conventional dendritic cells and monocytes as early carriers of Mtb from the lung to the medLN and show that, by three weeks post-infection, Mtb becomes concentrated within monocytic aggregates that support bacterial persistence. Conventional dendritic cells—particularly cDC1 and inflammatory cDC2 subsets—are required for robust TH1-skewed CD4 T cell priming due to sequential waves of IL-12 production in the medLN during the first 3 weeks

of infection. However, the monocytic niche in the medLN provides a site of bacterial persistence, where overwhelming numbers of Mtb-specific TH1 effector T cells fail to reduce Mtb burden within the medLN, despite effective control in the lung.

These findings reveal a state of functional immunological blindness within the medLN, in which immune activation is uncoupled from immune efficacy. Together, this work redefines lymphoid tissue involvement in tuberculosis pathogenesis, establishes the medLN as a privileged niche for Mtb persistence, and highlights the need for therapeutic and vaccine strategies that target tissue-specific immune constraints rather than immune activation alone.

Table of Contents

List of Figures

List of Tables

Acknowledgements

I would first like to acknowledge my former mentor, Dr. Vinicio de Jesus Perez. Vinicio, thank you for taking me in as a technician and introducing me to academic medicine and scientific research. Those years were foundational to my path, and I am deeply grateful for the opportunity. I also appreciate that you entrusted me with a project co-advised by Dr. Paul Bollyky, the first immunologist I had ever met. Through my interactions with the Bollyky lab, I discovered immunology and was inspired to pursue this field at UW. I am also thankful for the friendships that grew from that time—Mark, Jair, and Mario—who remain dear friends across the globe.

To my thesis advisors, Drs. Michael Gerner and Kevin Urdahl: thank you both for shaping me into the scientist I am today. Michael, your passion for science is unmistakable. The countless hours of one-on-one mentorship over the past six years have meant more than I can express. Through your guidance, I developed technical rigor, scientific confidence, and an honest understanding of the realities of academic science. I could not have asked for a more dedicated mentor. Kevin, you have been a grounding and visionary force in my training. I am continually amazed by the thoughtfulness and depth you bring to our work. Some of the most formative moments of my graduate career came from conversations where you reflected overnight on Mtb persistence, historical studies, or the broader arc of our scientific story, only to return with insights that reshaped our direction. Your breadth of knowledge in tuberculosis and immunology has been aspirational, and I am profoundly grateful for your mentorship.

To my incredible lab mates in both the Gerner and Urdahl labs: I have been fortunate to belong to two supportive and welcoming scientific homes. Whether sharing coffee breaks, celebrating impromptu “matching days,” gathering for happy hour, attending baseball games, or traveling to conferences, these moments built a sense of team and family that sustained me.

I especially want to thank Ada de la Cruz for her tremendous scientific support in the Gerner lab; Jaime Chao and Jessica Huang, who have been alongside me for nearly the entire journey and provided invaluable feedback in lab meetings; and former lab mates Michael Conlon, Miranda Lyons-Cohen, Joey Leal, Jaz Wilson, Brandy Olin, Caleb Stolfzus, Ramya Sivakumar, and Yixuan Wu. In the Urdahl lab, thank you to Daniel Kim, Lindsay Engels, and Sonia Chen. To the “Urdahl kids”—Natsumi Naranjo, Kimberly Foster, and Holly Barrett—thank you for the many thoughtful conversations and shared time in the office.

I am also grateful to Benjamin Gern, Sara Cohen, Courtney Plumlee, Lauren Cross, and Karolina Maciag for their scientific insight and mentorship; to Anuradha Kumar for her essential administrative and managerial support; and to Nicholas Lee for data management assistance.

To my cohort and friends in the Department of Immunology: thank you for the camaraderie and shared growth. I am especially grateful to Heber Lara, my cohort-mate and constant sounding board, for the scientific discussions and adventures along the way; and to Andrew Konecny, whose creativity and critical thinking have inspired and supported me, particularly in recent years. Your friendship has meant more than you know.

To my friends in Seattle: thank you for giving me a community that feels like home. To lifelong friends from childhood and college, thank you for the laughter, adventures, and steadfast presence through every stage of life. Christopher Diamond, Pablo Romano-Grover, Myell Mergaert, Carlos Vivaldo, Stuart Lai, and Adrian Almageur, your support, love, and joy have carried me, especially during difficult seasons.

To my extended family: those here with us, joining from afar, or present in our hearts, thank you for the unconditional love and strong sense of identity you have given me. I am especially grateful to my grandmother, Akhtar Joon, my aunts and uncles, and my cousins who enrich my life. I hope to see you all more often. I love you dearly.

To the Shehata family—Patricia, Ibrahim, and Soraya—thank you for welcoming me so warmly and for your constant love and support. Having you here today reminds me how rich I am in family.

To my brothers, Kian and Jonathan: I love you both deeply. Jonathan, I cherish your presence in my life and the creativity you bring into the world. Kian, though you are my younger brother, you have taught me what it means to live fully and cultivate meaningful relationships. You inspire me every day and it has been a privilege to be your older brother. I wish you great success in your pursuit of knowledge and science.

Laila—my wife, partner, and best friend—during the hardest moments of graduate school, when I questioned whether I could continue, I would still choose this path again because it led me to you. You are the greatest gift of this experience. Sharing a scientific language with you, building a life of adventure together, and dreaming about our future have sustained me. Thank you for listening endlessly about my project, for your thoughtful feedback on my writing and presentations, and for loving me through all of it. I love you.

Finally, to my parents: your sacrifices made this journey possible. You left Iran so that I could grow up with freedom, opportunity, and access to knowledge. I do not take that lightly. Your courage and devotion have shaped every achievement in my life. Because of you, I have been able to pursue science without limits. I cherish every day I have with you. You are the best parents I could have asked for, and I love you beyond words.

Section 1: Introduction

1.1 Tuberculosis disease global burden

Tuberculosis, the respiratory disease caused by *Mycobacterium tuberculosis* (Mtb), continues to be the leading cause of death from a single infectious agent worldwide. According to the 2024 World Health Organization (WHO) Global Tuberculosis Report, there were an estimated 10.8 million cases of TB and 1.2 million deaths attributable to TB disease, resulting in more deaths than COVID-19 during that year[1]. TB incidence is highest in regions of South-East Asia, Africa, and the Western Pacific. Many of these regions are also endemic for other diseases, including HIV, and are disproportionately affected by malnutrition and limited access to sanitary water sources, factors that further increase susceptibility to TB[1]. Understanding TB disease, bacterial persistence, and immune responses to Mtb is critical for the eradication of this disease and for reducing the global TB burden.

1.2 Mycobacteria and Mycobacterium tuberculosis

Mycobacteria are a class of slow-growing, rod-shaped bacilli characterized by a lipid-rich cell envelope and are commonly found in soil and water. While many species exist as harmless environmental saprophytes, several members of the *Mycobacterium* genus have evolved to become major human pathogens[2]. Certain mycobacteria, such as *Mycobacterium tuberculosis* (Mtb) and *Mycobacterium bovis*, cause tuberculous lung disease in humans, while other species, including *Mycobacterium leprae* and *Mycobacterium ulcerans*, are also devastating pathogens. Mtb infection and TB disease are classically lung-centric; however, mycobacteria can infect a wide range of other tissue sites, including skin and wound sites, lymphatic tissues, the spine, and bone[3].

Although *Mycobacterium tuberculosis* is the primary focus of this work, non-tuberculous mycobacteria (NTM) are environmentally derived opportunistic pathogens that can cause disease in both humans and wildlife. NTM include species such as *Mycobacterium abscessus*, *Mycobacterium avium*, and others, and are associated with significant clinical complications, particularly in the context of co-morbidities such as autoimmunity and cystic fibrosis[4,5]. While many NTM infections are benign, a substantial proportion require prolonged antibiotic treatment or surgical resection.

Beyond human infection, livestock and wildlife also serve as important reservoirs for mycobacterial disease, often with severe consequences including mortality and zoonotic transmission. Notably, many mycobacterial infections in wildlife are lymph-centric, with lymph nodes acting as major reservoirs for these pathogens[6,7]. Mycobacteria such as *M. bovis* can spread zoonotically from wildlife and livestock to other animals and humans through ingestion of infected tissues[8,9].

Despite having close pathogenic relatives, Mtb has evolved a specialized secretion pathway, ESX, also known as Type VII secretion. Pathogenomic analyses have identified this secretion system as a critical evolutionary advantage that enhances Mtb pathogenicity and enables it to better withstand host immune defenses, such as inflammasome activation [2,10,11]. While this feature distinguishes Mtb from many of its relatives, mycobacteria as a group continue to pose a substantial threat to global health in humans and other animals.

1.3 Tuberculosis infection and Diagnostics

Tuberculosis is transmitted via the aerosolized route when droplets containing *Mycobacterium tuberculosis* (Mtb) are expelled by an infected individual and subsequently inhaled by an uninfected individual (Fig. 1.1A, graphical schematic). Inhalation of as few as a single Mtb bacillus that reaches the deep airways is sufficient to eventually establish infection and lead to TB disease[12-14]. Based on current understanding, TB is defined as a spectrum of clinical presentations rather than a disease with a linear trajectory, as individuals may transition between infectious and non-infectious states and between symptomatic and asymptomatic disease. The International Consensus for Early TB (ICE-TB) developed a framework to distinguish TB disease from infection based on the presence of macroscopic pathology [15]. These guidelines defined two subclinical and two clinical tuberculosis states based on reported symptoms or signs of TB disease, which can be further subdivided by infection status according to the presence of Mtb.

Diagnosis of TB disease relies on multiple approaches. Currently, there is no gold-standard test for diagnosing TB infection, as available methods are largely based on measurements of host immune responses. Commercially available diagnostic tests include skin tests and interferon-gamma release assays (IGRAs), which measure immune stimulation in response to Mtb antigens

such as purified protein derivative (PPD) and the ESAT-6 and CFP-10 proteins[16]. As noted, these commercially available diagnostic assays are limited to host immune readouts, whereas experimental laboratory-based approaches can directly detect Mtb DNA by quantitative PCR or Mtb proteins by mass spectrometry following smear culture[16,17]. Although these laboratory tests can confirm the presence of Mtb with adequate sensitivity, their reliance on specialized laboratory infrastructure poses significant public health challenges in TB-endemic regions worldwide.

In addition, Mtb replication is slow, and the bacterium has evolved immune-evasion strategies, including its ESX secretion system, that enable it to avoid host detection. Together, immune evasion and the requirement for specialized laboratory facilities contribute to delays in TB diagnosis, further exacerbating public health challenges[18,19].

1.4 Understanding TB immunity in the lung

After inhalation of an Mtb bacillus into the deep terminal airways, lung-resident alveolar macrophages (AMs) are typically the first cell type to phagocytose this pathogen (Fig. 1.1A, deep airways) [20]. Previous work from our laboratory has demonstrated that AMs are not well suited for containment of Mtb, as the bacterium is capable of intracellular replication within these cells [20]. In addition, Mtb avoids immune activation within AMs through inhibition of antigen presentation machinery and disruption of the phagolysosome, allowing Mtb to persist within AMs for several days [20-23].

Approximately one week following infection, monocytes and neutrophils are recruited to the site of infection in the lung (Fig 1.1A). Inflammatory monocytes and neutrophils phagocytose and are infected by Mtb, while neutrophils additionally perform effector functions in an attempt to control bacterial replication. By 9–11 days post-infection, Mtb can disseminate via the lymphatic system to the lung-draining lymph nodes (LN), where phagocytes such as inflammatory monocytes and dendritic cells serve as important carriers of Mtb to these sites (Fig. 1.1A-B) [22,24].

By days 11–14 post-infection, adaptive immune responses are activated within the lung-draining LN and subsequently home to the site of infection in the lung (Fig. 1.1B). In TB, Th1-skewed CD4 T cells are particularly important for protection[25], although unconventional T cells,

natural killer (NK) cells, and B cells are also recruited to the site of infection (Fig. 1.1A, mature granuloma) [26]. At this stage, the lung develops a highly inflammatory milieu driven by recruited myeloid populations; however, Mtb replication continues, and bacterial burden increases.

By weeks 3–4 post-infection, bacterial burden in the lung further increases as continued recruitment of innate immune cells promotes the formation of granulomas, a hallmark of pulmonary TB infection (Fig. 1.1A). TB granulomas consist of a myeloid- and neutrophil-rich core surrounded by a lymphocytic cuff, where B and T cells accumulate but are unable to penetrate the pathogenic core. Although this organized structure disrupts normal lung architecture and function, granuloma formation represents an attempt by the host immune system to contain infection [26-28].

During this period, lymphocytes recruited to the lung and granuloma periphery can also organize into additional structures termed tertiary lymphoid structures. Recent publications have alternatively referred to these structures as bronchus–associated lymphoid tissue or granuloma-associated lymphoid tissue. These structures contain B cell–rich follicles and recruit CD4 T cells and myeloid populations that interact with and activate B cells [29].

In the lung-draining LN, bacterial burden also increases by weeks 3–4 post-infection, and T cell responses are known to wane within this secondary lymphoid organ[30]. Additional studies have demonstrated that, at later time points, LN involvement in sustaining adaptive immune responses is minimal. In Mtb-infected mice treated with busulfan to ablate thymic involvement, activated T cell responses were observed at levels comparable to untreated controls[31]. These findings suggest that the lung, through granuloma formation and the development of tertiary lymphoid structures, is sufficient to sustain adaptive immune responses during chronic infection. Throughout this period, Mtb continues to disseminate, with bacteria detectable in distal sites such as the spleen, bone marrow, and brain by weeks 3–4 post-infection[32].

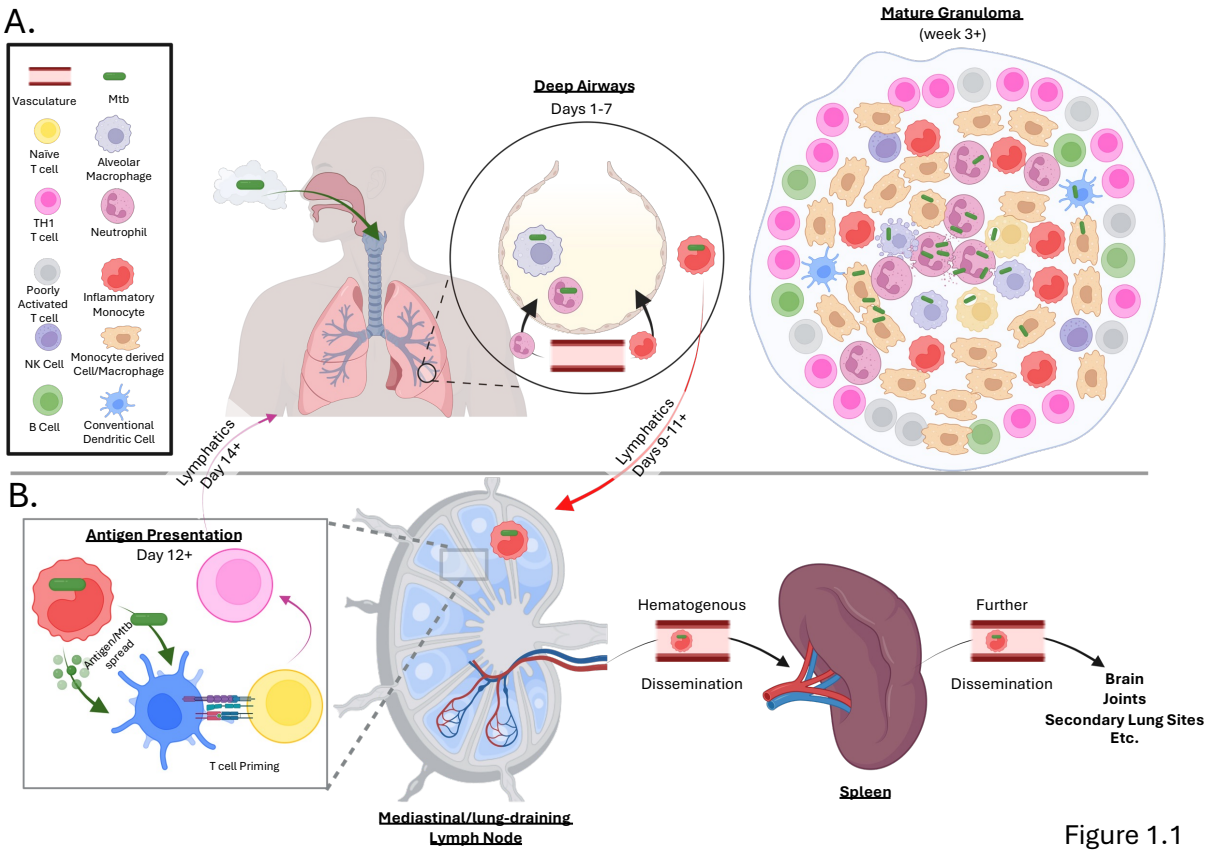

Figure 1.1

Figure 1.1: Mtb infection, progression, and dissemination

(A) Graphical representation of Mtb infection via inhalation of bacilli to deep airways and initial phagocytosis by Alveolar Macrophages, followed by recruitment of inflammatory monocytes and neutrophils to the lung. Mature granuloma formation shown to the right. (B) Representation of dissemination of Mtb from lungs to lung-draining mediastinal lymph node (medLN), with zoom in for spread of antigen/Mtb to conventional dendritic cells and activation of naïve T cells to effector T cells, which return to the primary lung infection site. Mtb further disseminates hematogenously to the spleen and alternate tissue sites such as the brain, joints, distal lung sites, and bone marrow.

1.5 Extra-pulmonary TB Disease and Mycobacterial Reservoirs

As noted above, Mtb (as well as other tuberculous mycobacteria and non-tuberculous mycobacteria) can disseminate beyond the lung and infect a wide range of tissues, including lymph nodes, the spleen, joints, the spine, bone marrow, the brain, and even tissues such as the eye, ear, or skin (Fig. 1.1B) [33,34]. These dissemination events can occur as part of the natural course of infection, and can lead to significant morbidity and mortality, especially when bacteria disseminate to critical tissue sites such as the brain and central nervous system [35]. Importantly, dissemination occurs at higher rates in immunocompromised individuals, although it is also observed in immunocompetent populations[1,36,37]. In a related context, Bacille Calmette–Guérin (BCG), the only widely used clinical vaccine against Mtb, is a live bacterium attenuated by sequential passaging of M. bovis for nearly a decade in the early 1900s[38]. BCG has also been implemented as a standard-of-care therapy for bladder cancer, where it induces localized, tissue-specific inflammation. However, cancer patients frequently receive therapies that carry immunosuppressive side effects, increasing the risk of widespread systemic inflammation and disseminated BCG infection, a condition known as BCGosis[39-41]. This condition can lead to outcomes similar to mycobacterial dissemination during infection, including granulomatous inflammation at extrapulmonary sites such as lymph nodes, which mycobacteria often infect. Although these events are currently rare, they are associated with severe morbidity and can be fatal in susceptible populations with immunocompromised co-morbidities. Similarly, the increasing prevalence of autoimmune diseases and the expanding use of immunotherapies that can induce temporary or sustained immunodeficiency[42]. Thus, careful consideration of disseminated TB disease and systemic mycobacterial infection will be critical for improving patient outcomes against TB, but also in contexts where the immune system is compromised by immunotherapy.

1.6 Tuberculosis outcomes and LN Involvement

Outcomes following TB diagnosis can include successful treatment with antibiotics or self-cure, resulting in a shift from clinical to subclinical disease based on the resolution of symptoms and signs or reduced infectiousness. Alternatively, mortality from TB disease is most often associated with post-primary disease, representing reactivation following an initial period of

containment or subclinical TB. While primary TB disease allows an individual to persist through the formation of granulomatous lesions in the lungs and facilitates dissemination of Mtb, post-primary disease associated with death is frequently characterized by obstructive lobular pneumonia, caseous necrosis, and chronic fibrocaseous disease[43].

Importantly, these divergent disease outcomes are associated with distinct patterns of involvement of the lung-draining lymph nodes. Early pathological studies conducted by Anton Ghon, and later corroborated by others, described tuberculous lesions in extrapulmonary sites, including lymph nodes. While the primary lesion, referred to as the Ghon focus or Ghon complex, represents the initial site of infection in the lung, Mtb can disseminate and establish lesions in additional tissues. In a 1904 post-mortem pathological study, Ghon identified numerous lesions in the lungs and alternative tissue sites of children who had died from TB or other causes[44,45]. Through this work, Ghon classified TB disease into seven subdivisions reflecting the extent of dissemination and reported that 7.6% of children had no detectable lung lesions yet exhibited prominent lesions in other tissues, most frequently within the lung-draining mediastinal lymph node (medLN). subsequent investigators reported similar findings across additional patient cohorts[46-49]. Collectively, this body of work described a relationship between unilateral or bilateral lesions in the lung and involvement of the corresponding mediastinal lymph nodes, such that lesion presence within a given lung lobe correlated with activation or persistence of Mtb within the associated medLN [44]. More recent studies have further characterized the association between medLN involvement and subclinical or latent TB infection (LTBI)[50]. These reports describe case studies of patients with PET/CT-positive lung-associated lymph nodes in the absence of detectable pulmonary TB disease, findings that closely parallel Ghon's historical observations.

Taken together, the historical and contemporary literature linking TB outcomes, including treatment, containment, and mortality, with mediastinal lymph node involvement raises fundamental questions regarding the role of the medLN in Mtb persistence, questions first highlighted by Ghon and colleagues over a century ago.

1.7 Secondary lymphoid organs and their role in immune response generation

While the blood vasculature delivers oxygen and nutrients and maintains tissue homeostasis through waste removal, the lymphatic system is responsible for the circulation and maintenance of interstitial fluids throughout the vertebrate body. Together, these circulatory systems coordinate lymphocyte trafficking from primary lymphoid organs - where immune cells originate in the bone marrow and thymus - to secondary lymphoid organs (SLOs) such as the spleen and lymph nodes, where immune responses to external stimuli, including pathogens, are initiated. Adaptive and innate lymphocytes recirculate through both the blood and lymphatic systems, often transporting information from peripheral non-lymphoid tissues in the form of antigens, immune cells, and inflammatory or molecular signals[51].

Lymph nodes are highly organized SLOs that enable immune surveillance of peripheral tissues, including the lung. These tissues are densely vascularized and composed of heterogeneous stromal populations, including high endothelial venules (HEVs), vascular endothelium, and lymphatic vessels, which collectively facilitate rapid lymphocyte entry, exit, and sampling of circulating networks. Stromal cells and immune cells such as dendritic cells (DCs) secrete chemokines that maintain lymph node architecture during homeostasis. Chemokine axes including CCL19/CCL21/CCR7 are critical for positioning T cells and DCs within the lymph node cortex, while CXCL12/CXCR4 and CXCL13/CXCR5 regulate B cell follicle formation and germinal center organization [52,53].

During infection, lymph nodes function as focal sites for adaptive immune education through antigen presentation by migratory phagocytes, including conventional dendritic cells (cDCs) and monocytes (Fig. 1.1B). These cells acquire antigen and inflammatory signals in peripheral tissues and relay this information to adaptive and innate immune populations through direct and proximal interactions within the lymph node microenvironment. Antigen capture and early inflammatory responses occur within lymphatic sinuses populated by macrophages and resident cDCs, particularly near the subcapsular sinus, where immune cells initiate responses to limit pathogen dissemination[54,55].

Upon maturation, cDCs migrate to the central T cell zone to initiate adaptive immune responses, followed by coordinated B cell follicle activation between B cells, T follicular helper

(Tfh) cells, and antigen-presenting cells[56]. These processes rely on chemokine gradients that are preserved during inflammation. CCR7 signaling is essential for myeloid cell migration to draining lymph nodes, while CXCL9/CXCL10/CXCR3 supports recruitment of activated effector T cells to pathogen-rich regions. In parallel, CXCR4 and CXCR5 signaling coordinates germinal center formation, while the CCL2/CCR2 axis regulates myeloid trafficking to sites of infection and, during dissemination, to draining lymph nodes[51].

In addition to immune activation, lymph nodes function as barriers to pathogen spread[57,58] while simultaneously serving as gateways for dissemination to distal sites[59]. During infection, lymph nodes undergo rapid structural reorganization that can impair homeostatic functions such as lymphocyte trafficking and tissue surveillance[60,61]. Given that mycobacterial infections frequently target lymph nodes and other SLOs as sites of persistent infection, understanding how these highly organized tissues are altered from early pathogen trafficking through chronic infection is critical, particularly in response to highly infectious pathogens such as Mtb.

1.8 Myeloid cell biology during Mtb infection

While Mtb infects multiple myeloid cell subtypes across tissues during infection, intracellular recognition of Mtb occurs through pathogen-associated molecular patterns (PAMPs). Of particular importance, toll-like receptors (TLRs) are transmembrane pattern-recognition receptors containing extracellular leucine-rich repeat domains that detect these PAMPs. Mtb is recognized by several TLRs through bacterial components[62,63] including cell wall constituents and proteins associated with the PE and ESX secretion systems[64,65]. These components are sensed by TLR1, TLR2, TLR4, TLR6, TLR8, and TLR9[66,67], leading to downstream intracellular activation. Among these, TLR2, TLR4, and TLR9 are most associated with recognition of Mtb-derived ligands. Engagement of TLRs induces inflammatory responses[68] through MyD88-dependent signaling pathways, resulting in activation of MAPK signaling, IL-1, TNF, and other downstream processes[66]. In antigen-presenting myeloid cells, this signaling promotes cellular maturation and enhances migration, antigen processing, and antigen presentation to adaptive immune cells.

In addition to being the first cell to phagocytose Mtb in the lung, previous studies have identified alveolar macrophages as permissive to high bacterial burdens and capable of

providing a favorable intracellular environment for Mtb replication and pathogenesis[20,21]. Following early phagocytosis by alveolar macrophages, monocytic and granulocytic populations are recruited to the lung, amplifying local inflammation. Granulocytic responses include the accumulation of neutrophils and, to a lesser extent, eosinophils. Neutrophils are particularly important, as they drive feed-forward recruitment loops, contribute to tissue damage, and form the core of granulomas during later stages of infection[69]. These granuloma cores often become necrotic and can develop into cavitary lesions that reduce viable lung tissue, contributing to mortality in post-primary TB and loss of bacterial control in animal models. Monocytic populations recruited to the lung display phenotypic heterogeneity throughout infection. Early responding cells that phagocytose Mtb are typically inflammatory monocytes (iMOs) derived from the bone marrow and recruited via inflammation-induced myelopoiesis[22,24]. Due to their plasticity, these monocyte-derived populations can differentiate in response to local environmental cues and have been described in the literature as monocyte-derived macrophages, monocytic phagocytes, interstitial macrophages, or, in this work, monocyte-derived cells (MCs). These cells are found both within granulomas and in less inflamed lung regions with reduced neutrophil infiltration.

In addition to monocytes and macrophages, plasmacytoid dendritic cells (pDCs) have been reported as important producers of type I interferons in the lung, likely promoting recruitment of innate immune cells, particularly neutrophils. Although relatively rare, pDCs can act as potent sources of cytokines that initiate downstream recruitment cascades [70].

Similar monocytic phenotypes have been described in secondary lymphoid organs such as the mediastinal lymph node (medLN) and spleen, where these cells exhibit variable expression of innate markers including Ly6C, CD11b, CCR2, CD64, and CD11c[22,71,72]. Many of these markers are associated with interferon-related pathways and functional specialization of monocytes, including inflammatory signaling, antigen presentation, and differentiation toward macrophage lineages.

Shortly after inflammatory monocytes are recruited to the lung and phagocytose Mtb, these cells transport bacteria to the medLN (Fig. 1.1B). Some studies have also reported Mtb transport by dendritic cells, although at substantially lower frequencies during early

infection[24,72]. Within the medLN, conventional dendritic cells (cDCs) play a central role in activating adaptive immune responses, either by presenting antigen acquired from other Mtb-harboring innate cells or by directly presenting antigen while containing bacteria (Fig. 1.1B) [71,72]. Migratory cDCs arriving from the lung further expand the antigen-presenting pool within this secondary lymphoid organ. While prior studies have examined relationships between cDCs and monocytes in the medLN and their respective roles in T cell priming, many relied on ex vivo systems or focused primarily on lung-derived antigen-presenting cells. Advances in lineage-specific markers and lineage-reporter mouse models now provide opportunities to more precisely define the innate immune compartment within the medLN during Mtb infection.

1.9 CD4 T cell heterogeneity in Mtb immunity

Adaptive immunity plays a central role in the control and protection against *Mycobacterium tuberculosis* (Mtb) infection. In particular, T cells are essential for reducing bacterial burden, as demonstrated by the severe susceptibility observed in HIV-infected patients with T cell deficiency and in T cell–depleted animal models[73-77].

Direct recognition of infected phagocytes and subsequent signaling from T cells to myeloid cells, including monocytes and macrophages, is critical for cellular clearance of Mtb[78]. As described in a recent review, T cell–phagocyte interactions occur through a sequence of coordinated signals that first recruit phagocytes, then promote their survival, and ultimately deliver activation cues that drive antimicrobial effector functions[79]. Among these signals, interferon-gamma (IFNγ) derived from T cells is a key mediator of phagocyte activation and mycobacterial control. The importance of IFNγ is supported by studies in IFNγ-deficient mice and in human cohorts with defects in IFNγ or IFNγ receptor signaling [80-83], although its efficacy has been shown to vary across murine models [84].

IFNγ signaling induces nitric oxide synthase 2 (iNOS), leading to the production of reactive nitrogen and oxygen species with antimicrobial activity[85-87]. However, iNOS expression alone does not necessarily correlate with bacterial clearance. Recent studies have demonstrated additional immunomodulatory roles for nitric oxide, including nitrosylation of key components of T cell signaling [88-92] and induction of hypoxia-driven bacterial dormancy through activation of the Mtb DosR regulon[93-96]. These findings suggest that while IFNγ is a critical component of

protective immunity, additional signals are required for effective Mtb control. Indeed, other T cell–derived mediators, including TNF[97], IL-2[98], GM-CSF[99,100], and CD40L[101], also contribute to phagocyte activation, highlighting the importance of heterogeneous T cell effector responses during infection.

While protective Th1 cells localize to sites of Mtb infection, substantial heterogeneity exists within the CD4 T cell compartment during Mtb infection, including Th17[102] and Th22[103] subsets, T follicular helper (Tfh) cells that support B cell responses[29], and regulatory T cells (Tregs)[104]. While this list is not exhaustive and additional phenotypes such as Th2 cells may arise under specific conditions or co-infections, these subsets represent the most established CD4 T cell fates implicated in Mtb immunity.

IL-17–producing Th17 cells are detected during Mtb infection and can confer protection[102,105,106]. Although IL-17 is dispensable for natural protection against most Mtb strains[107], it can enhance protection in vaccination settings[102,108,109]. IL-17 and IL-22 produced by Th17 cells promote immune cell recruitment and activation[110], including recruitment of Th1 CD4 T cells[102], though dysregulated IL-17 responses can drive pathogenic neutrophilia and tissue damage[111].

Th22 responses are an additional T helper subtype that is activated against Mtb infection and has been detected in animal and patient cohort studies[103,112,113]. IL-22 can directly inhibit Mtb growth[114] and promote recruitment of monocytes and macrophages[115]. In parallel, Tfh cells coordinate B cell activation and germinal center responses, and Tfh and Tfh-like cells have been identified in both secondary lymphoid organs and tertiary lymphoid structures during Mtb infection[29]. Conversely, regulatory T cells limit excessive inflammation and tissue damage but can also suppress protective Th1 responses[104,116].

Collectively, these diverse CD4 T cell populations provide overlapping but non-redundant effector functions that shape the trajectory of Mtb infection. Yet a defining feature of Mtb immunity is its temporal and spatial complexity: adaptive responses are delayed relative to other respiratory pathogens due to the slow transport of bacteria from the lung to the lung-draining mediastinal lymph node (medLN)[117]. Although naïve T cell priming occurs in the medLN during early infection, T cell responses wane in this compartment over time[30]. While both

infected and uninfected myeloid cells can present antigen to naïve T cells in the medLN[24,71,72,118], the lung sustain T cell activity during chronic infection, where granulomas and tertiary lymphoid structures support continued adaptive immunity[31]. These dynamic shifts in the location and quality of T cell responses underscore a fundamental question: which cellular mediators sustain protective immunity at the site of infection, and which fail to do so? Classical CD8 T cells are increasingly recognized as critical contributors to this sustained lung response, encompassing both classically restricted populations capable of cytotoxic killing and IFNγ production, and non-classical subsets that bridge innate and adaptive immunity. Yet the relative contributions of these populations, and the conditions under which they confer meaningful protection, remain incompletely resolved.

1.10 Classical and non-classical CD8 T cell subsets in Mtb immunity

CD8 T cells represent an additional arm of interferon-gamma (IFNγ)–producing T cells implicated in immune responses to Mtb infection. Early mouse studies suggested a limited role for CD8 T cells in protection against Mtb[77,119]. However, classically restricted CD8 T cells can recognize MHC class Ia–presented Mtb peptides and produce IL-2, TNF, and IFNγ, thereby delivering activating signals to immune cells and infected phagocytes[120]. CD8 effector T cells, along with natural killer (NK) and NKT cells, also secrete cytotoxic molecules such as granzymes, perforins, and granulysin that can directly kill Mtb-infected cells[121,122].

While mouse models have provided limited support for CD8 T cell–specific effector mechanisms, and human cohort studies remain constrained in their ability to assess CD8 T cell function in TB, non-human primate studies have identified an important role for both CD8β - classical, and CD8α-non-classical T cells[74,75]. These cells contribute to protection during early Mtb infection by limiting initial bacterial establishment, dissemination, and downstream disease progression[74].

Non-classical CD8 T cell populations, including invariant natural killer T (iNKT) cells, γδ T cells, and mucosal-associated invariant T (MAIT) cells, recognize non-peptide antigens presented by non-classical MHC molecules[123,124]. These populations have been detected in Mtb-infected individuals and implicated in resistance to Mtb infection within patient cohorts in endemic regions[125,126]. Such cells recognize mycobacterial lipid antigens and other non-peptidic

components, providing an additional mode of pathogen detection that bridges innate and adaptive immunity. In mouse models, MAIT cell expansion has been shown to delay early T cell priming in lung-draining lymph nodes, yet these cells can confer protection during later stages of chronic infection through IL-17 production[127].

Together, both classical and non-classical CD8 T cell populations contribute to protective immunity during Mtb infection through complementary cytokine-mediated and cytotoxic effector functions.

1.11 B cell responses in Mtb Infection

B cells represent an important arm of the adaptive immune response, producing antibodies that mediate opsonization, neutralization, and complement activation, and also functioning as antigen-presenting cells (APCs) for T cells. These roles have been implicated in Mtb infection, where B cells can present antigen to generate Mtb-specific CD4 T cell responses[128,129] and produce antibodies that enhance detection and cytotoxicity of Mtb-infected cells[130-132].

Despite these potential protective functions, relatively few mycobacteria-reactive antibody variants are detected within the lung, whereas such antibodies are more abundant in the serum[129]. Notably, protective antibody variants have been identified through Fc-engineering and screening approaches, where specific Fc–Fab combinations enhance early neutrophil activation and antimicrobial activity[133]. These findings suggest that antibody-mediated protection against Mtb may depend on specific qualitative features rather than overall antibody abundance.

Historically, however, the contribution of B cells to protection against Mtb has remained inconclusive. Multiple B cell depletion studies across mouse models, non-human primates, and human cohorts have reported limited or no impact on disease outcome[131,134-137], despite marked increases in B cell numbers during infection. Collectively, these observations indicate that while B cells and antibodies can contribute to immune responses against Mtb and represent a potential avenue for therapeutic intervention, naturally induced B cell responses during Mtb infection are not sufficient or essential mediators of protection.

1.12 Immunization efforts against Mtb

As natural immunity does not confer sterilizing protection against Mtb, vaccination strategies are critical for eradicating TB disease. The oldest vaccine against *Mycobacterium tuberculosis* (Mtb), Bacille Calmette–Guérin (BCG), was generated in the early twentieth century through serial attenuation of *Mycobacterium bovis* over approximately a decade[38]. This live-attenuated vaccine remains the global standard for TB prevention and, in combination with public health interventions and improved sanitation, has contributed to TB eradication in many regions. However, despite widespread use of BCG, large portions of the global population remain susceptible to Mtb infection. BCG is most effective during infancy and demonstrates reduced efficacy against primary infection in adults[138].

Proposed mechanisms underlying BCG-mediated protection concern the overlap between the BCG and Mtb antigen repertoires, enabling the generation of cross-reactive T cell memory responses at distal sites of BCG administration, as well as inducing innate immune memory (trained immunity)[139]. As discussed previously, BCG, like other mycobacteria, localizes to and persists within lymphatic tissues such as lymph nodes, where adaptive immune responses are initiated. Following recognition by pattern recognition receptors, including TLRs, BCG induces innate inflammation and is subsequently presented to T cells. BCG-induced CD4 T cell responses have been shown to accelerate early immune events, including translocation of alveolar macrophages from the lung parenchyma to the interstitium and subsequent transfer of Mtb from alveolar macrophages to monocytes and neutrophils [140]. BCG also induces polyfunctional CD4 T cell responses in both animal models and human studies, with memory T cells detectable as early as three weeks post-vaccination but waning by approximately fourteen months[141].

In addition to CD4 T cell responses, BCG-induced CD8 T cell immunity contributes to protection, as demonstrated by reduced Mtb control in CD8 T cell depletion studies[74,75]. Beyond adaptive immunity, BCG localizes to the bone marrow and induces trained innate immunity, a phenomenon similarly observed with fungal-derived β-glucans, whereby epigenetic reprogramming of innate progenitors enhances responses to subsequent pathogenic stimuli[142].

Several alternative vaccination strategies are currently under investigation. In addition to BCG revaccination, MTBVAC, a live-attenuated vaccine candidate, is undergoing phase II clinical

trials and has demonstrated safety comparable to BCG with enhanced Th1 CD4 T cell responses[143,144]. Other approaches aim to augment or build upon BCG-mediated immunity through recombinant BCG formulations, subunit vaccines, or viral vectors designed to boost pre-existing immune responses[145]. With multiple candidates advancing through clinical trials, these interventions hold promise for improving protection against a pathogen that remains a formidable global health challenge. Despite advances in both innate and adaptive immunity research, the fundamental mechanisms underlying BCG-mediated protection, and how to optimize or extend this protection, remain incompletely understood. Elucidating these mechanisms will be critical for improving current vaccination strategies against Mtb.

1.13 Summary

Mtb, like other mycobacteria, requires specific cellular niches to support survival, replication, and dissemination, and has co-evolved with mammals as a means of pathogen survival. Prior work has suggested that this niche likely involves a dynamic innate immune cell population that is permissive to bacterial persistence, mounts limited inflammatory responses, and remains relatively undetected by adaptive immunity. While substantial effort has focused on defining how Mtb is sensed by the immune system and how host responses are coordinated, a complete understanding of protective and sterilizing immunity remains lacking, as underscored by the inability to substantially improve upon a century-old live-attenuated vaccine.

Defining the cellular and anatomical niches that support Mtb persistence is therefore critical. Identification of these niches may reveal new targets for intervention aimed at improving immune detection and bacterial sterilization, thereby reducing disease progression, dissemination within the host, and transmission at the population level.

Section 2: Dissertation Objectives and Significance

The medLN as a site of Mtb persistence

This dissertation investigates a central and unresolved question in tuberculosis immunology: how Mtb persists within the lung-draining medLN, the primary site of adaptive immune response initiation. While lymph nodes are classically viewed as organs that coordinate protective immunity, clinical and experimental evidence suggests that they can also serve as reservoirs of persistent infection. The studies presented here aim to define the cellular, spatial, and temporal mechanisms that allow Mtb to survive within this immunologically active tissue.

In **Section 4**, we address this question using complementary in vivo approaches including mouse models of aerosol infection, multiparameter confocal microscopy, flow cytometry, mathematical modeling, and single-cell transcriptomics. We identify cDCs and monocytes as early carriers of Mtb from the lung to the medLN, where they initiate antigen presentation and T cell priming. As infection progresses, however, we observe the formation of monocyte-derived cellular aggregates harboring multiple bacilli that persist long-term within the medLN. Through transcriptional profiling and spatial analysis, we define this structure as a specialized monocytic niche enriched for inflammatory, metabolic, and tissue-repair programs that nonetheless fails to eliminate bacteria. Mathematical modeling further reveals that, beyond initial dissemination, the medLN supports substantial local Mtb replication. Finally, we show that while IL-12–producing cDC subsets are essential for early Mtb-specific CD4 T cell activation, these monocytic aggregates become functionally invisible to T cells at later stages. We also demonstrate that BCG vaccination limits bacterial burden and monocytic niche formation without preventing initial trafficking to the medLN, indicating that this tissue is a site of immune control against Mtb.

In **Section 5**, we interrogate whether shifting key components of the adaptive immune response can overcome Mtb persistence within the medLN. To directly test whether enhanced TH1 immunity can disrupt the monocytic niche, we supplement infected hosts with ex vivo–polarized, Mtb-specific TH1 CD4 T cells during critical windows of niche establishment. While this approach significantly reduces bacterial burden in the lung, Mtb persistence within the medLN remains largely unaffected, despite partial disruption of monocytic aggregates. These

findings reveal a striking tissue-specific limitation of otherwise protective adaptive immune mechanisms.

Collectively, this dissertation identifies a monocyte-derived niche that provides a permissive environment for Mtb persistence, most prominently within the lung-draining medLN but also detectable at the primary site of infection in the lung. Although this niche is attenuated by BCG vaccination, its persistence highlights the need for additional strategies to target infected myeloid populations and the tissues that harbor them. Future directions, explored in **Section 6**, include identifying targetable monocyte-intrinsic pathways, promoting immune responses in alternative anatomical sites, and extending these findings to other mycobacterial infections and chronic inflammatory diseases such as cancer, where similar myeloid-dominated niches emerge. By redefining the medLN as both a site of immune initiation and a reservoir of bacterial persistence this work demonstrates that immune activation and immune efficacy can become uncoupled within lymphoid tissues. Thus, we reveal a fundamental limitation of current vaccine and immunotherapeutic strategies that focus primarily on amplifying TH1 responses. Understanding how Mtb exploits monocytic niches in lymph nodes provides a conceptual framework for developing interventions that target not only immune responses, but also the cellular and anatomical contexts in which pathogens persist.

Section 3: Materials and Methods

This section was adapted from the STAR Methods sections of my first-author manuscript "Monocytic Niches Enable Mycobacterium tuberculosis Persistence in Lymph Nodes", with additional methods related to sections 5 and 6.*

Mice

C57BL/6, C3H/FeJ, B6.129S(C)-Batf3^{tm1Kmm}/J (BATF3$^{-/-}$) and B6.SJL mice were purchased from Jackson Laboratories (Bar Harbor, ME). BATF3$^{-/-}$ mice have been previously described[146]. B6.Cg-Xcr1$^{tm2(HBEGF/Venus)Ksho}$ (XCR1-Venus)[147,148] mice were provided by the RIKEN BRC through the National BioResource Project of the MEXT, Japan, and were redistributed by Dr. Mark Headley (Fred Hutchinson Cancer Center) with permission from RIKEN BRC. B6.129S6(C)-*Zbtb46*$^{tm1.1Kmm}$/J (Zbtb46-GFP) mice[148,149] were also kindly provided by Dr. Mark Headley. ESAT-6 TCR Transgenic (C7) mice were provided by Dr. Eric Pamer (Memorial Sloan Kettering Cancer Center, New York, NY) and have been described previously[117]. Ag85B TCR Transgenic (P25) mice have been previously described[150]. B6(Cg)-*Ifnar1*$^{tm1.2Ees}$/J (IFNaR$^{-/-}$) mice were provided by Dr. Michael Gale (University of Washington). Mice with ESAT-6 TCR-Transgenic T cells on a CD45.1 background were generated in house by crossing ESAT-6 TCR Tg mice with B6.SJL mice, with genotypic confirmation through blood phenotyping by flow cytometry. CD11c-Cre mice (Jackson Laboratories) were crossed to IRF4$^{fl/fl}$ mice (Jackson Laboratories) to generate CD11c-Cre;IRF4$^{fl/fl}$ mice.

All mice were housed in specific pathogen free conditions in individually ventilated cages with a maximum density of 5 mice per cage, and negative pressure ventilation and air filtering provided by either Seattle Children's Research Institute (SCRI) or the University of Washington, South Lake Union campus. Animals were monitored by full-time staff, and given access to food and water ad libitum, with a 12 hour light/dark cycle, maintained at 22-25 degrees Celsius. All mice were of normal health and immune status, and were naïve of treatment, procedure, or invasive testing prior to experiment start. Experiments were performed in compliance of the Animal Care and Use Committee at SCRI or the University of Washington, as appropriate, and all experiments were conducted with sex and age-matched mice (male and female mice between the ages of 8-16 weeks old). The influence of sex was not assessed.

For experiments involving Zbtb46-DTR bone marrow (Section 5), diphtheria toxin receptor (DTR) is expressed under the DC-lineage-specific Zbtb46 promoter, allowing depletion of DCs with DT treatment. DT was intraperitoneally administered in phosphate-buffered saline (PBS) at 20 ng/g bodyweight.

Mycobacterium tuberculosis (Mtb)

For use in murine infections, Mtb H37Rv infections were performed with and without a transformed mCherry reporter plasmid driven by the pMSP12 promoter, as previously described[20,151]; Mtb SA161 was provided by Ian Orme (Colorado State University)[152]. Virulence of these strains are maintained by periodic passage in mice.

Table 3.1: Materials:

REAGENT or RESOURCE	SOURCE	IDENTIFIER
Antibodies		
BUV563 anti-mouse CD11c	BD (clone HL3)	749040; RRID: AB_2873434
BUV805 anti-mouse CD86	BD (Clone 2331 (FUN-1))	741946; RRID:AB_2871258
BV421 anti-mouse CD45.2	Biolegend (clone 104)	109832; RRID:AB_2565511
BV480 anti-mouse SiglecF	BD (Clone E50-2440)	746668; RRID:AB_2743940
BV510 anti-mouse SIRPa	BD (Clone P84)	740159; RRID:AB_2739912
BV605 anti-mouse Ly6G	Biolegend (clone A20)	127639; RRID:AB_2565880
BV650 anti-mouse XCR1	Biolegend (clone ZET)	148220; RRID:AB_2566410
BV711 anti-mouse PDL1	BD (Clone 10F.9G2)	563369; RRID:AB_2738163
BV785 anti-mouse B220	Biolegend (clone RA3-6B2)	103246; RRID:AB_11218795
PE anti-mouse CD88	Biolegend (Clone 20/70)	135806; RRID:AB_2243735
PerCP-ef710 anti-mouse CD64	Invitrogen (clone (X54-5/7.1))	46-0641-82; RRID:AB_2735016
PE-Cy7 anti-mouse CD26	Biolegend (Clone H194-112)	137810; RRID:AB_2564312
APC anti-mouse CD45	Biolegend (clone 30-F11)	103112; RRID:AB_312977
AF700 anti-mouse Ly6C	Biolegend (Clone HK1.4)	128024; RRID:AB_10640119
APCeF780 anti-mouse MHCII	Ebio (clone M5/114.15.2)	47532182; RRID:AB_1548783
APC anti-mouse CD88	Biolegend (Clone 20/70)	135807; RRID:AB_10899415
AF488 anti-mouse CCR2	R&D (clone 475301)	FAB5538G; RRID:AB_3651044
PerCP-Cy5.5 anti-mouse CD88	Biolegend (Clone 20/70)	135813; RRID:AB_2750209

BV421 anti-mouse BCL6	BD (Clone K112-91)	563363; RRID:AB_2738159
BUV395 anti-mouse KLRG1	BD (clone 2F1)	740279; RRID:AB_2740018
BUV661 anti-mouse CD8	BD (clone 53-6.7)	750023; RRID:AB_2874241
BUV737 anti-mouse CD3	BD (clone 17A2)	612803; RRID:AB_2870130
BUV805 anti-mouse CD4	BD (clone GK1.5)	612900; RRID:AB_2827960
BV510 anti-mouse CD45.1	Biolegend (clone A20)	110741; RRID:AB_2563378
BV510 anti-mouse CD90.1	Biolegend (clone OX-7)	202535; RRID:AB_2562643
BV605 anti-mouse Ki67	Biolegend (Clone 16A8)	652413; RRID:AB_2562664
BV711 anti-mouse CD44	Biolegend (clone IM7)	103057; RRID:AB_2564214
BV785 anti-mouse Tbet	Biolegend (clone 4B10)	644835;RRID:AB_2721566
Primary anti-mouse IRF4	Biolegend (clone IRF4.3E4)	646402; RRID:AB_2563110
AF555 anti-mouse TCF1	CST (Clone C63D9)	17404S; RRID:AB_2798895
PE-Cy7 anti-mouse PD1	Biolegend (clone RMP1-30)	109110; RRID:AB_572017
AF700 anti-mouse pS6	CST (Clone D57.2.2E)	27036S; RRID:AB_2798937
APC ef780 anti-mouse CD25	Invitrogen (clone PC61.5)	47-0251-82; ; RRID:AB_1272179
BV711 anti-mouse MHCII	BD (clone M5/114.15.2)	563414; RRID:AB_2738191
PerCP-Cy5.5 anti-mouse B220	Biolegend (clone RA3-6B2)	103236; RRID:AB_893354
PerCP-Cy5.5 anti-mouse NK1.1	Biolegend (clone PK136)	108728; RRID:AB_2132613
PerCP-Cy5.5 anti-mouse CD11b	Biolegend (clone M1/70)	101228; RRID:AB_893232
PerCP-Cy5.5 anti-mouse CD11c	Biolegend (clone HL3)	117328; RRID:AB_2129641
AF488 anti-mouse TCF1	Cell Signaling (clone C63D9)	6444s; RRID:AB_2797627

APC anti-mouse CD45.2	Biolegend (clone 104)	109814; RRID:AB_389211
Biotin anti-mouse SIRPa	Invitrogen (clone P84)	13-1721-82; RRID:AB_2573352
BV421 anti-mouse CD45.1	Biolegend (clone A20)	110732; RRID:AB_2562563
BV480 anti-mouse CD11c	BD (clone N418)	746392; RRID:AB_2743706
eF506 anti-mouse Ki67	Invitrogen (clone SolA15)	69-5698-82; RRID:AB_2574235
PE anti-mouse CD64	Biolegend (clone X54-5/7.1)	139304; RRID:AB_10612740
BV421 anti-mouse CD64	Biolegend (clone X54-5/7.1)	139309; RRID:AB_2562694
R718 anti-mouse Ki67	BD (clone SolA15)	567292; RRID:AB_2916041
APC anti-mouse IL-12p40/IL-23	Biolegend (clone C15.6)	505206; RRID:AB_315370
R718 anti-mouse B220	BD (clone RA3-6B2)	567381; RRID:AB_2916576
R718 anti-mouse CD3	Biolegend (clone 17A2)	567296; RRID:AB_2916539
APCeF750 anti-mouse CD3	Biolegend (clone 17A2)	100247; RRID:AB_2572117
BV421 anti-mouse CD3	Biolegend (clone 17A2)	100228; RRID:AB_2562553
AF488 anti-mouse CD11c	Biolegend (clone N418)	117311; RRID:AB_389306
APCeF750 anti-mouse B220	Biolegend (clone RA3-6B2)	103259; RRID:AB_2572108
Primary anti-mouse pS6	CST (clone 2F9)	4856S; RRID:AB_2181037
Secondary rabbit anti-mouse AF750	Invitrogen	A-21039; RRID:AB_2535711
APC anti-mouse MerTK	Biolegend (clone 2B10C42)	151507; RRID:AB_2650738
AF488 anti-mouse VCAM1	Biolegend (clone 429 (MVCAM.A))	105710; RRID:AB_493427
BV421 anti-mouse CD68	BD (clone FA-11)	566389; RRID:AB_2739021
AF555 anti-mouse CD68	Abcam (clone EPR20545)	AB280860

Primary anti-mouse MHCII	Biolegend (clone M5/114.15.2)	107602; RRID:AB_313317
FITC anti-mouse Mtb	Abcam	ab20962; RRID:AB_445945
AF488 anti-mouse p120	Santa Cruz (Clone 6H11)	sc23873; RRID:AB_2086394
primary anti-iNOS	Thermo Fisher (clone C-11)	14-5920-82; RRID:AB_2572890
RB704 anti-mouse Ki67	BD (clone SolA15)	570280; RRID:AB_3685635
Rb744 anti-mouse CD3	BD (clone 17A2)	570561; RRID:AB_3685845
Rb780 anti-mouse B220	BD (clone RA3-6B2)	569207; RRID:AB_3684868
MPO	Abcam (CloneEPR20257)	ab208670; RRID:AB_2864724
Bacterial and virus strains		
Mycobacterium tuberculosis H37Rv	Obtained from Joel Ernst (NYU)	ATCC 27294
M. tuberculosis H37Rv mCherry	Generated in house	N/A
M. tuberculosis SA161	Provided by Ian Orme	Clinical Isolate from patient
Barcoded *M. tuberculosis* H37Rv	Obtained from David Sherman (UW)	N/A
BCG-Pasteur	ATCC	ATCC 35734
Chemicals, peptides, and recombinant proteins		
Mix-n-Stain CF Dye Antibody Labeling Kits	Biotium	Cat# 92433-92339
DY-395XL-NHS-Ester	Dyomics	295XL-01A
Ovalbumin-488	Invitrogen	O34781
Cell Trace Violet	Invitrogen	C34557
Middlebrook 7H9 broth	BD Difco	Cat# 271310
Middlebrook 7H10 agar	BD Difco	Cat# 262710
OADC supplement	BD Difco	Cat# 212240
Tween-80	Sigma-Aldrich	Cat# 9005-65-6
DNase I	Sigma-Aldrich	Cat# 10104159001
Dispase II	Sigma-Aldrich	Cat# 04942078001
Collagenase P	Sigma-Aldrich	Cat# 11213857001
Isoflurane	Henry Schein	N/A
Zombie UV Fixable Viability Dye	BioLegend	Cat# 423107
BD Cytofix	BD Biosciences	Cat# 554655
OCT Compound	Tissue-Tek, Fischer Scientific	Cat# 23-730-571

Sucrose	Sigma-Aldrich	Cat# 57-50-1
Critical commercial assays		
MagniSort Mouse Naïve CD4+ T Cell Isolation Kit	Thermo Fisher Scientific	Cat# 8804-6824-74
CellTrace Violet	Thermo Fisher Scientific	Cat# C34557
eBioscience Intracellular Fixation & Permeabilization Kit	Thermo Fisher Scientific	Cat# 88-8824-00
NEBNext Ultra DNA Library Prep Kit for Illumina	New England Biolabs	Cat#E7103
NEBNext Multiplex Oligos for Illumina	New England Biolabs	Cat#E6440S
AMPure XP beads	Beckman Coulter	Cat# A63880
SMART-Seq v4 Ultra Low Input RNA Kit	Takara Bio	Cat# 88-8824-00
Nextera XT DNA Library Prep Kit	Illumina	Cat# FC-131-1096
LymphoLyte	Cedarlane	Cat# CL5035
Deposited data		
Mycobacterium tuberculosis Co-opts Monocytic Niches to Evade Immunity in Lymph Nodes	Gene Expression Omnibus (GEO)	GSE309019
Experimental models: Organisms/strains		
Mouse: C57BL/6J	Jackson Laboratory	JAX:000664
Mouse: C3H/FeJ	Jackson Laboratory	JAX:000658
Mouse: B6.129S(C)-Batf3tm1Kmm/J (BATF3−/−)	Jackson Laboratory	JAX:013755
Mouse: B6.SJL-Ptprca Pepcb/BoyJ (CD45.1)	Jackson Laboratory	JAX:002014
Mouse: B6.Cg-Xcr1tm2(HBEGF/Venus)Ksho (XCR1-Venus)	RIKEN BRC	RBRC09485
Mouse: B6.129S6(C)-Zbtb46tm1.1Kmm/J (Zbtb46-GFP)	Provided by Dr. Mark Headley	JAX:027618
Mouse: ESAT-6 TCR Transgenic (C7)	Provided by Dr. Eric Pamer	JAX:035728
Mouse: Ag85B TCR Transgenic (P25)	Previously described	JAX:011005
Mouse: B6(Cg)-Ifnar1tm1.2Ees/J (IFNaR−/−)	Provided by Dr. Michael Gale	JAX:028288
Mouse: ESAT-6 TCR Transgenic (C7) x Bt.SJL (C7 CD45.1)	This study	NA
Software and algorithms		
Cell Ranger v7.1.0	10x Genomics	RRID:SCR_017344
Seurat	Satija Lab	RRID:SCR_016341
SingleR	Bioconductor	RRID:SCR_023730
clustifyr	Bioconductor	RRID:SCR_023718
rrvgo	Bioconductor	RRID:SCR_023725
slingshot	Bioconductor	RRID:SCR_017012

STAR aligner v2.4.2a	Dobin et al.	RRID:SCR_004463
HTSeq	Anders et al.	RRID:SCR_005514
Picard Tools	Broad Institute	RRID:SCR_006525
Imaris	Bitplane	RRID:SCR_007370
FlowJo	BD Biosciences	RRID:SCR_008520
Other		
Glas-Col Aerosol Infection Chamber	Glas-Col	Glas-Col Aerosol Infection Chamber
gentleMACS Dissociator	Miltenyi Biotec	gentleMACS Dissociator
Cytek Aurora	Cytek Biosciences	Cytek Aurora
Leica SP8 Confocal Microscope	Leica Microsystems	Leica SP8 Confocal Microscope
10x Chromium Controller	10x Genomics	10x Chromium Controller
Illumina NextSeq 500	Illumina	Illumina NextSeq 500
Illumina NovaSeq X	Illumina	Illumina NovaSeq X
Illumina NextSeq 2000	Illumina	Illumina NextSeq 2000
Glas-Col Aerosol Infection Chamber	Glas-Col	Glas-Col Aerosol Infection Chamber

Method Details:

Conventional dose Mtb aerosol infections

All infections were done with stocks of either Mtb H37Rv mCherry or Mtb SA161, as previously described[153]. To perform conventional dose aerosolized infections, mice were placed in a Glas-Col aerosol infection chamber, and ~100 CFU were deposited directly into their lungs. The nebulization cycle was set to 45 minutes followed by 45 minutes of cloud decay. To confirm infectious dose, 2 mice from each infection were immediately sacrificed. Lungs were harvested and homogenates were plated on 7H10 plates for CFU counting after ~3 weeks of growth.

Ultra-low dose Mtb Aerosol Infections

Bar-coded H37Rv Mtb was used for all infections[14]. Mtb stocks were grown in Middlebrook 7H9 with OADC supplement and 0.05% Tween-80 at 37℃ with constant agitation to an OD = 1. Cultures were filtered through a 5µm filter to remove clumps and aliquots were frozen at -80℃. Frozen filtered stocks were thawed and titered side by side with stocks used for conventional dose infection to determine how to dilute the ULD stocks with the goal of leaving 37% of mice uninfected. Mice were placed in a Glas-Col aerosol infection chamber and 5mL of diluted Mtb was injected into the nebulizer of the infection chamber. The nebulization cycle was set to 45 minutes followed by 45 minutes of cloud decay. For analysis, uninfected mice were excluded from plots shown.

Barcoded Sequencing

Mice were infected with a pool of 50 bar-coded strains. Sequencing of bacterial bar-codes has been previously described[69]. Briefly, genomic DNA was pre-amplified with pooled barcoded primers before libraries were prepared with NEBNext Ultra DNA Library Prep Kit for Illumina (New England Biolabs) using the AMPure XP reagent (AgenCourt Bioscience) for size selection and cleanup. The NEBNext Multiplex Oligos for Illumina (New England Biosciences) were used to barcode DNA libraries and enabled multiplexing of 96 libraries per sequencings run. Samples were sequenced using the NextSeq 500 Mid Output v2 kit (Illumina) at the University of Washington Northwest Genomics Center. Read alignment was carried out using a custom processing pipeline that has been previously described.

CFU Determination

Mouse tissues (right lung, left lung, LN) were individually homogenized in an M tube (Miltenyi) containing BS+0.05% Tween-80. Homogenates were diluted and plated onto 7H10 plates. Plates were incubated at 37 degrees Celsius for a minimum of 21 days before CFU enumeration.

Naïve cell isolation and adoptive transfers

Spleens and lymph nodes (LNs) were harvested from C7 mice and enriched for naïve CD4 T cells using the MagniSort™ Mouse Naïve CD4+ T cell isolation Kit (Thermo Fisher, #8804-6824-74). For flow cytometry experiments, isolated naïve CD4 T cells were labeled with Cell Trace Violet (Thermo Fisher, #C34557) following manufacturer kit protocol. Cells were confirmed for naïve phenotype and congenic markers, counted, washed and resuspended in sterile PBS, then intravenously injected into recipient mice at indicated timepoints. In all adoptive transfer experiments, host mice received ~10^6 naïve C7 cells.

Th1 polarization and adoptive transfers

CD4 T cells from the indicated TCR transgenic mice (Tg.WT (CD90.1$^+$), Tg.KO (CD90.1$^+$, CD45.1$^+$) and OTII (CD45.1$^+$)) were negatively enriched from spleens using EasySep magnetic microbeads (STEMCELL). T cells were Th1 polarized by culturing 1.6 × 10^6 transgenic T cells with 8.3 × 10^6irradiated splenocytes from C57/Bl6 mice (post-CD3-negative selection by EasySep) per 2ml well at 37°C with 5% CO2. 5 µg/ml of ESAT-6 or OVA peptide, 10 ng/ml IL-12, and 10 µg/ml of anti–IL-4 antibody (R&D Systems) were added to RP10 media at day 0. On day 3, cells were split 2:1, and 10 ng/ml IL-12 added (R&D Systems). On day 5, Th1 cells were intravenously injected into C57BL/6 CD45.2$^+$ recipient mice at the indicated timepoints.

OVA-488 Intratracheal Labeling

OVA-488 was used from Thermo Fisher (O34781) and reconstituted to 2 mg/mL according to manufacturer recommendation in sterile PBS. Reagent was diluted fresh 1:2 in PBS on the day of administration, to yield a dose of ~33ug/50 uL. Mice were anesthetized via isoflurane until sufficient to induce deep breathing, after which they were hung up on a rubber band by their teeth to displace their tongue by forceps and administer the reagent. Mice were held in this position until the reagent solution was inhaled and monitored until awakened.

BCG Immunizations

BCG-Pasteur was used for all studies. BCG was cultured in Middlebrook 7H9 with OADC supplement plus 0.05% Tween-80 at 37℃ with constant agitation for five days. BCG was back diluted in 7H9 for two days and grown to an OD of 0.2-0.5. Bacteria were diluted in PBS and mice were injected subcutaneously with 10^6 CFU in 200µL. BCG was diluted and plated on 7H10 plates and plates were counted for CFU after 21 days to confirm dose of immunization. After immunization, mice were rested for 8 weeks prior to Mtb infection.

Single cell suspensions from mouse tissue

Lungs and LNs were harvested from sacrificed mice at indicated timepoints and placed into cold RPMI buffer containing 10% fetal bovine serum (FBS) with DNase I (100 µg/ml; Sigma-Aldrich), Dispase II (800 µg/ml; Sigma-Aldrich), and Collagenase P (200 µg/ml; Sigma-Aldrich). Lungs were homogenized using a gentleMACS dissociator (MilTenyi Biotec), while LNs were individually dissociated by sharp forcep disruption in a 24 well plate. Homogenized samples were incubated for 30 min at 37C with periodic manual disruption, then filtered through a 100 uM cell strainer and RBC lysed using RBC lysing buffer (Thermo), then resuspended in FACS buffer (PBS +2.5% FBS +0.1% NaN3). Blood cells were harvested by cardiac puncture, and isolated using LymphoLyte, following manufacturer protocol.

Antibody Staining

Single cell suspensions were first washed in PBS and then incubated with 50 µl Zombie UV viability dye (BioLegend) for 10 min at room temperature in the dark. Viability dye was immediately quenched by the addition of 100 µl of a surface antibody cocktail diluted in 50% FACS buffer/50% 24G2 Fc block buffer using saturating levels of antibodies. Surface staining was performed for 20 min at 4°C. Then, the cells were washed once with FACS buffer and fixed overnight with the eBioscience Intracellular Fixation and Permeabilization kit (Thermo Fisher). The following day, cells were permeabilized with the provided permeabilization buffer, incubated for 60 min at 4°C with 100 µl of an intracellular antibody cocktail diluted 1:100 in permeabilization buffer, and washed with FACS buffer. Cells were analyzed on the Cytek Aurora.

Confocal Microscopy

For confocal imaging, PFA-fixed and sectioned LN tissues were imaged as previously described using a Leica SP8 microscope[56]. Briefly, isolated LN tissues were fixed using BD Cytofix (BD

Biosciences) diluted 1:3 in PBS for 20–24 h at 4°C then dehydrated with 30% sucrose solution for 24–48 h at 4°C. LNs were then embedded in an OCT compound (Tissue-Tek) and stored at −20°C. LNs were sectioned on a Thermo Fisher Scientific Micron HM550 cryostat into 20-µm sections and stained as previously described[56]. A Leica SP8 tiling confocal microscope equipped with a 40× 1.3 NA oil objective was used for image acquisition. All raw imaging data was processed and analyzed using Imaris (Bitplane).

Histocytometry

Histocytometry analysis was performed as previously described[56,154]. Briefly, multiparameter confocal images were corrected for fluorophore spillover using the built-in Leica Channel Dye Separation module. Single stained controls were acquired using UltraComp eBeads (Invitrogen) that were incubated with fluorescently conjugated antibodies and then mounted on slides with Fluormount-G slide mounting media (Thermo Fisher Scientific). All images were visualized and analyzed using Imaris (Bitplane). For analysis of myeloid aggregates, a combinatorial myeloid channel was created using CD11c and Sirpα signals using the Imaris XT channel arithmetic module, and this sum myeloid channel was used for myeloid isosurface object creation without cell splitting but including region growing. Aggregates were then filtered by volume, where surfaces below 10000 um^3 were excluded. Mtb surfaces were created by using mCherry signal, where these isosurface objects were used for visual clarity in representative overview images. C7 isosurface objects were created on congenic CD45.1 signal for analysis of Ki67, pS6, and Tbet expression by mean fluorescence intensity. Clustering analysis was performed by creating isosurfaces on CD45.1 or CD45.2 congenic signal without cell splitting. Surfaces were then filtered by volume, and surfaces exceeding 2500 voxels (defining dense clusters representing ∼3 or more cells) were included for density analysis. IL-12 surfaces were determined by masking IL-12p40 signal in T cell cluster surfaces, then analyzed for Zbtb46-GFP, SIRPa, or XCR1-Venus expression. Density analyses were performed by calculating number of isosurfaces per LN volume, where LN volume was calculated by manually creating a surface over the entire LN area across Z stacks.

Single cell RNA-sequencing

Single cell suspensions were generated from medLN, blood, and lung samples as described above prior to Mtb infection and at days 0, 15 and 28 post-Mtb infection from pools of 8-10 mice for each suspension/condition. Cells were resuspended in 200 µl MACS buffer (PBS containing 2.5% FBS plus 1 mM EDTA), filtered through a 70 µm filter, and run on a FACS AriaII (BD) sorter. To collect parenchymal cells for single-cell RNA sequencing, alveolar macrophages (AM, SiglecF$^+$ Autofluorescence$^+$) were sorted separately into one collection tube to account for autofluorescence in the IV label channel, and all other IV-negative cells were sorted into a separate collection tube. After sorting, AMs were included in respective lung samples (Mtb-infected or uninfected). Mtb-infected and uninfected bystander (mCherry$^+$ and mCherry$^-$) samples were harvested separately. After one round of washing with ice-cold DPBS, cells were resuspended to 1000 cells/µl in DPBS, and ~8000 cells were inputted into the 10X Genomics pipeline following the manufacturer's recommendations. After the generation of cDNA following the manufacturer's protocol, samples were centrifuged through two sequential rounds of 0.2 µm SpinX (Costar) columns to sterilize the sample for removal from the BSL3 facility and subsequent library generation. Libraries were sequenced by Psomagen (Rockville, MD) on an Illumina NovaSeq X platform, with 300M reads per sample.

Alignment and processing of single cell RNAseq data

10X chromium 3'-derived scRNAseq sequence reads were aligned to the 10X Genomics pre-built mouse reference genome mm10-2020-A, assigned to individual cells by barcode, and unique molecular identifiers (UMI) summarized using the 10X Cell Ranger 7.1.0 software package.

The Seurat R package was used for initial QC filtering and integration. First, a filtering step was applied across all samples, requiring all passing cells to have UMIs mapped to at least 500 distinct genes and fewer than 5% of UMIs mapped to mitochondrial genes. Genes detected in fewer than three cells per mouse were excluded from further analysis.

The Seurat integration pipeline[155] was then applied to correct for batch effects, normalizing for cell numbers via sctransform for findmarkers within Seurat[156], and aligning cells across conditions, including all combinations of tissues, timepoints, and infection statuses. UMAP clustering was determined using Seurats FindNeighbor and FindCluster functions using a resolution of 0.5. Cell type annotations were refined using SingleR package and ImmGen Fine

reference annotations[157,158] by mapping cluster-specific gene expression profiles to curated immune cell gene signatures, enabling high-resolution classification of immune cell subsets in the single-cell RNA-seq dataset. These annotations were then refined using curated gene set lists and top markers and aligned with our flow cytometry cell type annotations (iMO, MC, cDC). Correlation annotation gene expression analysis and plots were generated using clustifyr package[159]. Pearson (centered delta of gene expression) correlation was performed on genes excluding common low-informative genes (mt-, ribosomal, hemoglobin, etc.) to best identify correlations and differences between cell types.

To quantify changes in cell type proportion over time, total numbers of cells per sample were calculated and normalized to cells per thousand per sample. Negative-binomial linear models, appropriate for zero-inflated count data, were fit and used to calculate P values using the R glm.nb function.

DEG analysis was performed using sctransform values to normalize for different read depth between samples, using cutoffs of log2FC > 0.5 and adjusted p value (FDR) < 0.05. These DEGs were then run for mSigDB Hallmark and Gene Ontology: Biological Processes (GO:BP) gene set enrichment analysis (GSEA). GO:BP GSEA was then reduced to parent terms using rrvgo package to minimize redundancy of terms[160]. For GO:BP reduced bubble plots, up to 5 leading edge genes were shown based on over-representation across GO terms within each parent term.

Pseudotime slingshot analysis was performed on monocyte subsets as shown (S.2F) to determine trajectory, with pMO and iMO1 cell clusters set as origins based on prior annotations and timepoint meta data[161]. Pseudotime scores were then mapped onto the original UMAP space to represent trajectories.

The mouse Mtb Innate Atlas DEG and GSEA data sets are publicly available for exploration and use at https://eshamskh-mouse-mtb-innate-atlas.share.connect.posit.cloud . Primary data can be found at GSE309019.

MC Gene Signature Scoring

First, the top 50 genes from FindMarkers (Seurat) across ImmGenGroup cell types were determined and isolated for MC cells (Table 3.2). To quantify cross-species enrichment of the murine MC gene signature in human datasets, we first converted mouse genes to their human

orthologues using a one-to-one orthology mapping (Ensembl BioMart), restricting to high-confidence protein-coding genes. Genes without clear orthologues or mapping to multiple human genes were excluded to avoid inflation of signature size. The resulting humanized MC gene set was then intersected with the expressed gene matrix of the human RNA-seq/scRNA-seq dataset. Signature scores were calculated on a per-cell (or per-sample) basis using a rank-based module scoring approach implemented in Seurat (AddModuleScore), which computes the average expression of the signature genes subtracted by the aggregated expression of matched control gene bins to account for gene expression distribution biases. Scores were subsequently z-scored across cells for visualization and downstream comparative analyses between clinical groups.

Bulk RNA sequencing

MedLNs, lungs, and blood of interest were harvested and processed into single cell suspensions, stained with cell surface markers, and sorted (gating schemes in Fig. S6F) from individual mice on days 0, 15, and 25 post-Mtb infection. 200 cells for each condition was sorted on an Aria II (BD Biosciences) directly into reaction buffer from the SMART-Seq v4 Ultra Low Input RNA Kit for Sequencing (Takara). Reverse transcription was performed followed by PCR amplification to generate full-length amplified cDNA, as previously described[162]. Sequencing libraries were constructed using the NexteraXT DNA sample preparation kit with unique dual indexes (Illumina) to generate Illumina-compatible barcoded libraries. After the generation of libraries following the manufacturer's protocol, samples were centrifuged through two sequential rounds of 0.2 µm SpinX (Costar) columns to sterilize the sample for removal from the BSL3 facility. Libraries were pooled and quantified using a Qubit Fluorometer (Life Technologies). Sequencing of pooled libraries was carried out on a NextSeq 2000 sequencer (Illumina) with paired-end 59-base reads using NextSeq P2 sequencing kits (Illumina) with a target depth of 5 million reads per sample. Base calls were processed to FASTQs on BaseSpace (Illumina) and a base call quality-trimming step was applied to remove low-confidence base calls from the ends of reads. The FASTQs were aligned to the GRCm38 mouse reference genome using STAR v.2.4.2a, and gene counts were generated using htseq-count. QC and metrics analysis was performed using the Picard family of tools (v1.134). Gene counts were filtered and normalized

from raw counts by trimmed-mean of M values (TMM) normalization and filtered for genes expressed with at least one count per million total reads in at least 10% of the total number of libraries. Further downstream analysis was performed using publicly available RNAseq toolkits. Gene signatures were derived from previous work[70], and generated alongside heatmap data tables by inputting DEG data into the BIOMEX toolkit[163].

Primary data can be found on GEO.

Quantification and Statistical Analysis

Statistical tests were selected based on appropriate assumptions with respect to data distribution and variance characteristics. Statistical details of experiments can be found in the figure legends. No statistical methods were used to predetermine sample size. The statistical significance of differences in mean values was determined by the appropriate test, as denoted in the figure legends $****$, $p \leq 0.0001$; $***$, $p \leq 0.001$; $**$,$p \leq 0.01$; and $*$, $p \leq 0.05$ or otherwise noted.

Mathematical Modeling Details:

Calculating total number of circulating monocytes

Total concentration of white blood cells in mice is assumed at 5×10^3 cell/ul of blood based on prior study[164]. Monocytes represent about 1% of WBCs[164]. The total blood volume in mice is dependent on weight and has been calculated to be 7.8 mL per 100 g of body weight[164]. A mouse of 20g weight then has 1.5 mL of blood, and thus, ~0.8×10^6 monocytes in circulation. Based on our measurements (we did not weigh the mice), this is a slight overestimate as we find 0.3×10^5 monocytes in B6 mice (**Fig. S7H**). The half-life time of murine circulating monocytes is estimated at about 17 hours or removal rate of $d_B = ln(2)/(17/24) \approx 1/day$[164].

Modeling sIVs of monocytes in circulation and their migration to medLN

To quantify kinetics of monocyte migration from the blood to medLN we developed a mathematical model that tracks labeling of cells with different Abs administered at different times. In our basic model (**Fig. S3E**), we assume that monocytes in circulation are produced at a

rate p from the bone marrow, and that cells in circulation migrate to various tissues and/or die at a rate d_B with m_{BN} being the rate of cell migration from blood to medLN. In our experiments, we only label circulating cells with one Ab, administered at $\tau 1$ time prior to sampling time T; therefore, in this model we track the dynamics of cells unlabeled and labeled with sIVs Ab in the blood (B_u and B_l, respectively) and in the LN (N_u and N_l, respectively):

$$\frac{\mathrm{d}B_u}{\mathrm{d}t} = p - (d_B + m_{BN})B_u - l(t)B_u, \quad (1)$$

$$\frac{\mathrm{d}N_u}{\mathrm{d}t} = m_{BN}B_u - d_N N_u, \quad (2)$$

$$\frac{\mathrm{d}B_l}{\mathrm{d}t} = l(t)B_u(t) - (d_B + m_{BN})B_l, \quad (3)$$

$$\frac{\mathrm{d}N_l}{\mathrm{d}t} = m_{BN}B_l - d_N N_l, \quad (4)$$

where initially all cells are unlabeled and in the simplest model, at the steady state, $B_u(0) = p/(m_{BN} + d_B)$, $N_u(t0) = mp/(d_N(m_{NB} + d_B))$, and $B_l(0) = N_l(0) = 0$ where time starts from Mtb infection and sampling is done at time T. This is different from a typical set-up of the original sIVs study where time is counted backwards from the time of sampling[54]. In the model, $l(t)$ is the function describing pulse labeling by sIVs Abs:

$$l(t) = \begin{cases} r_l, & \text{if } T + \tau_1 \le t \le T + \tau_1 + \Delta\tau_1, \\ 0, & \text{otherwise,} \end{cases} \quad (5)$$

where $T + \tau 1$ is the time of 1st Ab injection, $\Delta\tau 1$ is the duration of labeling (typically, 20-30 min given the half-life time of the Ab), and r_l is the rate of labeling of the cells by the Ab. In our experiments $\tau 1 = -24$ h $= -1$ d.

In previous studies involving sIVs, Ab-labeled cells were typically sampled once; however, in our experiments, we injected labeling Ab at several times, typically 1 day prior to tissue sampling, e.g., at $T = 0, 14$, etc days since Mtb infection. Therefore, the basic model (eqns. (1)–(4)) needs to be solved for every sampling time T. By assuming that labeling of circulating cells with

the sIVs Ab occurs rapidly and by knowing the number of circulating cells at time of Ab injection ($T + \tau 1$) given in eqn. (1) (with $l(t) = 0$) the dynamics of Ab-labeled cells in circulation and LN is then:

$$\frac{\mathrm{d}B_l}{\mathrm{d}t} = -m_{BN}B_l, \quad (6)$$

$$\frac{\mathrm{d}N_l}{\mathrm{d}t} = m_{BN}B_l - d_N N_l, \quad (7)$$

where $t \in (0, -\tau 1)$ and $B_l(0) = B_u(T + \tau 1)$ (from eqn. (1)) and $N_l(0) = 0$. The number of sIVs+ myeloid cells in the LN is $N_l(-\tau 1)$ and can be calculated iteratively for different values of the sampling time T.

In our analyses, we found that a model that assumes a constant rate of monocyte migration from the blood to the medLN does not adequately describe the sIVs data; to allow for the rate of monocyte migration to change with time, we adopt a previous approach that assumed that the migration rate is constant in a given time interval but may vary between time intervals:

$$m_{BN}(t) = \begin{cases} m_{BN_1}, & \text{if } 0 \text{ days} \leq t < 10 \text{ days}, \\ m_{BN_2}, & \text{if } 10 \text{ days} \leq t < 25 \text{ days}, \\ m_{BN_3}, & \text{otherwise.} \end{cases} \quad (8)$$

The choice of the time intervals where the rate of migration is changing is semi-arbitrary as long as changes occur in between experimental measurements; we chose them to allow for change in the rapid increase in the migration rate from uninfected state to 10-14 days post Mtb infection, and then small decline in the migration rate after 22-25 days post-infection.

Modeling Mtb dissemination from the lung to medLN

To describe the dynamics of Mtb-infected cells in the lung and mediastinal medLN (medLN) we adopted mathematical models recently developed to describe dissemination of Mtb bacilli from the lung to medLN and spleen after a conventional dose infection(Cross et. al., In Prep). In the

simplified version of the model, we track the number of Mtb-infected (myeloid) cells in the lung and medLN assuming that infected cells in the medLN migrate from the lung, and that growth in the number of Mtb-infected cells is described by logistic model:

$$\frac{\mathrm{d}I_L}{\mathrm{d}t} = r_L(1 - I_L/K_L) - m_{LN}I_L, \quad (9)$$

$$\frac{\mathrm{d}I_N}{\mathrm{d}t} = r_N(1 - N/K_N)I_N\theta(I_N - I_{N_{cr}}) + m_{LN}I_L, \quad (10)$$

where I_L and I_N are the number of Mtb-infected myeloid cells in the lung and medLN at time t after infection, respectively, r_i and K_i denote the rate of Mtb replication and carrying capacity of Mtb in the i^{th} tissue, $\theta(x)$ is a shifted Heaviside function defined as $\theta(x) = 0$ if $x < 1$ and $\theta(x) = 1$, otherwise, medLN is the rates of Mtb-infected cell migration from the lung to medLN. In the model, infection starts with infected cells in the lung ($I_L(0) = I_0$) but not the medLN ($I_N(0) = 0$).

We found that the logistic model (eqns. (9)–(10)) did not accurately describe the data, in part, because the logistic model predicts reaching a steady state over time while the actual number of Mtb-infected cells peaked at 21 days and declined afterwards (S. 7J), most likely due to an immune response. We therefore formulated an alternative model that takes this into account (**Fig. S3F**).

Adaptive immune responses can control Mtb numbers several weeks post-infection[165]. Because in our studies, we lacked fine-grained measurements of Mtb- specific T cell response dynamics in the lung and medLN (only timed transfers were used), here we propose a simple model previously shown to describe immune dynamics following vaccination or influenza virus infection in humans[166]. We thus assume that immune response E expands exponentially after exposure and suppresses Mtb replication as $f(E) = 1/(1 + (hE)^n)$:

$$\frac{\mathrm{d}I_L}{\mathrm{d}t} = \frac{(r_L+\delta_L)I_L}{1+h^nE(t)^n} - \delta_L I_L - m_{LN}I_L, \quad (11)$$

$$\frac{\mathrm{d}I_N}{\mathrm{d}t} = \left[\frac{(r_N+\delta_N)I_N}{1+h^nE(t)^n} - \delta_N I_N\right]\theta(I_N - I_{N_{cr}}) + m_{LN}I_L, \quad (12)$$

where $E = e^{\rho t}$ and for simplicity we set $\rho = 0.6/\text{day}167$. We define time $T_E = -\ln(h)/\rho$ as the time when immune response is at half maximal capacity to inhibit growth of the bacteria.

To describe migration of Mtb+ myeloid cells from the lung to medLN that had been stained with OVA-488 we used model-predicted number of Mtb+ cells in the lung (eqn. (11)) at time $T + \tau_O$ where $\tau_O = -24$ h is the time of OVA-488 administration prior to sampling at time T :

$$\frac{\mathrm{d}I_L^o}{\mathrm{d}t} = -m_{LN}I_L^o, \quad (13)$$

$$\frac{\mathrm{d}I_N^o}{\mathrm{d}t} = m_{LN}I_L^o - \delta_N I_N^o, \quad (14)$$

where $t \in (0, -\tau_0)$ and $\tau_O = -24$ h is the time of labeling of lung-localized myeloid cells with OVA-488 and ${I_L}^O(0) = I_L(T + \tau_O)$ (from eqn. (11)) and ${I_N}^O(0) = 0$. The number of Mtb+ myeloid cells that had migrated from the lung to medLN in $-\tau_O$ time is ${I_N}^O(-\tau_O)$ and can be calculated iteratively for different values of the sampling time T.

In fitting models to data on migration of Mtb+ myeloid cells, we found that models with a constant rate of migration of cells from the lung to the medLN generally did not fit the data very accurately. This was in part because the ratio of lung-to-medLN migrating myeloid cells to total number of myeloid cells in the lung was non-linearly dependent on the time since infection. Therefore, we assumed that the rate of migration of Mtb+ cells from the lung to medLN change with time since infection. Similarly to our previous work[168], we allow for the migration rate to be constant in a given time interval $(t_i, t_i + 1)$ but change between different time intervals that are determined by times when experimental measurements were taken:

$$m_{LN}(t) = \begin{cases} m_{LN_1}, & \text{if } 0 \text{ days} \leq t < 15 \text{ days}, \\ m_{LN_2}, & \text{if } 15 \text{ days} \leq t < 22 \text{ days}, \\ m_{LN_3}, & \text{if } 22 \text{ days} \leq t < 30 \text{ days}, \\ m_{LN_4}, & \text{otherwise.} \end{cases} \tag{15}$$

Fitting models to data

To fit models to data, we log-transformed the data and model predictions and minimized the sum of squared residuals (SSR). Data or model predictions on the number of cells that were below a limit of 1 we set to be equal to this limit. We compared alternative models using either F-test (for nested models) or AIC (for non-nested models). In most cases we attempted to fit the least number of parameters, e.g., by fixing some parameters to values found in the literature (e.g., the rate of monocyte migration/death from the blood to other tissues). Note that because we assumed that the rates of cell migration are constant in a given time period but change between time periods, the model predicted changes in the number of myeloid cells migrating from the blood (Fig. 4.S.7H) or the lung (Fig. 4.S.7J) or to medLN to appear oscillatory. Modeling the migration rate to be dependent on time would require additional parameters and was not pursued.

Declaration of generative AI and AI-assisted technologies in the writing process

During the preparation of this work the authors used ChatGPT from OpenAI to proofread portions of the text for grammatical accuracy. After using this tool/service, the authors reviewed and edited the content as needed and take full responsibility for the content of the published article.

Table 3.2: MC Gene Signature scores (mtb pos/neg)

Signature	Rank	Mouse_Gene	Human_Gene
MC_Mtb_pos_top50	1	Tmem178	TMEM178A
MC_Mtb_pos_top50	2	8430430B14Rik	NA
MC_Mtb_pos_top50	3	Cst7	CST7
MC_Mtb_pos_top50	4	Orm1	NA
MC_Mtb_pos_top50	5	Mmp2	MMP2
MC_Mtb_pos_top50	6	Saa3	NA
MC_Mtb_pos_top50	7	Tnfsf15	TNFSF15
MC_Mtb_pos_top50	8	Ak4	AK4
MC_Mtb_pos_top50	9	Plpp3	NA
MC_Mtb_pos_top50	10	Nos2	NOS2
MC_Mtb_pos_top50	11	Gpnmb	GPNMB
MC_Mtb_pos_top50	12	Sdc1	SDC1
MC_Mtb_pos_top50	13	Slc1a2	SLC1A2
MC_Mtb_pos_top50	14	Gdpd1	GDPD1
MC_Mtb_pos_top50	15	Inhba	INHBA
MC_Mtb_pos_top50	16	Il12a	IL12A
MC_Mtb_pos_top50	17	Myo10	MYO10
MC_Mtb_pos_top50	18	C1s1	NA
MC_Mtb_pos_top50	19	Procr	PROCR
MC_Mtb_pos_top50	20	H2-M2	NA
MC_Mtb_pos_top50	21	Htra1	HTRA1
MC_Mtb_pos_top50	22	Asb11	ASB11
MC_Mtb_pos_top50	23	Vcam1	VCAM1
MC_Mtb_pos_top50	24	Cd38	CD38
MC_Mtb_pos_top50	25	Gm40932	NA
MC_Mtb_pos_top50	26	Tst	TST
MC_Mtb_pos_top50	27	Clmp	CLMP
MC_Mtb_pos_top50	28	Bvht	NA

MC_Mtb_pos_top50	29	Adgb	ADGB
MC_Mtb_pos_top50	30	Mcoln2	MCOLN2
MC_Mtb_pos_top50	31	Slc7a2	SLC7A2
MC_Mtb_pos_top50	32	Plxna1	PLXNA1
MC_Mtb_pos_top50	33	Clec4e	CLEC4E
MC_Mtb_pos_top50	34	Btbd16	BTBD16
MC_Mtb_pos_top50	35	C1ra	C1R
MC_Mtb_pos_top50	36	Acsl1	ACSL1
MC_Mtb_pos_top50	37	Dpys	DPYS
MC_Mtb_pos_top50	38	Src	SRC
MC_Mtb_pos_top50	39	Cfb	CFB
MC_Mtb_pos_top50	40	Ms4a7	MS4A7
MC_Mtb_pos_top50	41	Fzd1	FZD1
MC_Mtb_pos_top50	42	AA467197	C15orf48
MC_Mtb_pos_top50	43	Acp5	NA
MC_Mtb_pos_top50	44	Olfr111	OR5V1
MC_Mtb_pos_top50	45	Best1	BEST1
MC_Mtb_pos_top50	46	Fblim1	FBLIM1
MC_Mtb_pos_top50	47	Ptges	PTGES
MC_Mtb_pos_top50	48	Il1a	IL1A
MC_Mtb_pos_top50	49	Tnfaip8l3	TNFAIP8L3
MC_Mtb_pos_top50	50	Ksr2	KSR2
MC_Mtb_neg_top50	1	C1qa	C1QA
MC_Mtb_neg_top50	2	C1qc	C1QC
MC_Mtb_neg_top50	3	C1qb	C1QB
MC_Mtb_neg_top50	4	Itga9	ITGA9
MC_Mtb_neg_top50	5	Plxdc2	PLXDC2
MC_Mtb_neg_top50	6	Lyz1	LYZ
MC_Mtb_neg_top50	7	Mafb	MAFB
MC_Mtb_neg_top50	8	Cd81	CD81

MC_Mtb_neg_top50	9	Pltp	PLTP
MC_Mtb_neg_top50	10	Ccr5	CCR5
MC_Mtb_neg_top50	11	Vcam1	VCAM1
MC_Mtb_neg_top50	12	Timp2	TIMP2
MC_Mtb_neg_top50	13	Mmp14	MMP14
MC_Mtb_neg_top50	14	Saa3	NA
MC_Mtb_neg_top50	15	Myo1e	MYO1E
MC_Mtb_neg_top50	16	Frmd4b	FRMD4B
MC_Mtb_neg_top50	17	Cmklr1	CMKLR1
MC_Mtb_neg_top50	18	Cd38	CD38
MC_Mtb_neg_top50	19	Arhgap10	ARHGAP10
MC_Mtb_neg_top50	20	Snx24	SNX24
MC_Mtb_neg_top50	21	Creb5	CREB5
MC_Mtb_neg_top50	22	Sdc4	SDC4
MC_Mtb_neg_top50	23	Abca1	ABCA1
MC_Mtb_neg_top50	24	Tma16	TMA16
MC_Mtb_neg_top50	25	Gatm	GATM
MC_Mtb_neg_top50	26	Slc7a8	SLC7A8
MC_Mtb_neg_top50	27	Mitf	MITF
MC_Mtb_neg_top50	28	Sash1	SASH1
MC_Mtb_neg_top50	29	Cd14	CD14
MC_Mtb_neg_top50	30	Cfb	CFB
MC_Mtb_neg_top50	31	Sh3pxd2b	SH3PXD2B
MC_Mtb_neg_top50	32	Klrb1b	KLRB1
MC_Mtb_neg_top50	33	Lmna	LMNA
MC_Mtb_neg_top50	34	Il18bp	IL18BP
MC_Mtb_neg_top50	35	Rgs1	RGS1
MC_Mtb_neg_top50	36	Ly6a	NA
MC_Mtb_neg_top50	37	Ppargc1b	PPARGC1B
MC_Mtb_neg_top50	38	Sod2	SOD2

MC_Mtb_neg_top50	39	Aoah	AOAH
MC_Mtb_neg_top50	40	Axl	AXL
MC_Mtb_neg_top50	41	Tbxas1	TBXAS1
MC_Mtb_neg_top50	42	Procr	PROCR
MC_Mtb_neg_top50	43	Rab7b	NA
MC_Mtb_neg_top50	44	Adap2	ADAP2
MC_Mtb_neg_top50	45	Acsl1	ACSL1
MC_Mtb_neg_top50	46	H2-Eb1	HLA-DRB5
MC_Mtb_neg_top50	47	Rab20	RAB20
MC_Mtb_neg_top50	48	Parvb	PARVB
MC_Mtb_neg_top50	49	Fth1	FTH1
MC_Mtb_neg_top50	50	Mertk	MERTK

Section 4: Monocytic Niches Enable *Mycobacterium Tuberculosis* in Lymph Nodes

This section has been adapted from my first-author manuscript. We thank members of the Gerner and Urdahl laboratories for insightful discussions and project support, particularly Ada de la Cruz, Daniel Kim, Kim Foster, Dat Mai, and Natsumi Naranjo.

Elya A. Shamskhou[1,2], Fergal J. Duffy[1], Lauren M. Cross[1], Courtney R. Plumlee[1], Benjamin H. Gern[1,3,4], Holly W. Barrett[1], Alan H. Diercks[1], Sara B. Cohen[1], Ramya Sivakumar[2], John D. Aitchison[1,4], Vitaly V. Ganusov[5], Kevin B. Urdahl[1,2,4*], Michael Y. Gerner[2*]

1. Center for Global Infectious Disease Research, Seattle Children's Research Institute, Seattle, WA, USA
2. Department of Immunology, University of Washington, Seattle, WA, USA
3. Department of Global Health, University of Washington, Seattle, WA, USA
4. Department of Pediatrics, University of Washington, Seattle, WA, USA
5. Host-Pathogen Interactions Program, Texas Biomedical Research Institute, San Antonio, TX, USA

*Correspondence: gernermy@uw.edu; kevin.urdahl@seattlechildrens.org

Summary:

Lung-draining mediastinal lymph nodes (medLNs) are critical for *Mycobacterium tuberculosis* (Mtb) pathogenesis, serving as initiating sites of protective T cell responses and, paradoxically, as sites of long-term pathogen persistence. We examined myeloid and CD4 T cell response dynamics in medLNs after aerosol Mtb infection. Early dissemination occurred via monocytes and IL-12-producing conventional dendritic cells (cDCs), which harbored single bacilli and initiated Th1 priming within the T cell zone. Thereafter, cDC migration and Th1 priming declined, and medLNs became dominated by large monocyte-derived aggregates containing multiple bacilli, which persisted into late infection. Despite inducing proinflammatory and bactericidal signaling pathways, these aggregates weren't recognized by Mtb-specific T cells and failed to clear Mtb, forming an immunologically 'blind' niche. BCG vaccination reduced Mtb burden and niche establishment, without altering myeloid trafficking or T cell priming. Thus, Mtb persists in medLNs within specialized monocytic niches exhibiting classical immune pathways that are insufficient for sterilizing control.

4.1 Introduction

Tuberculosis remains a leading cause of global mortality, recently reclaiming its position as the world's deadliest infectious disease caused by a single pathogen, *Mycobacterium tuberculosis* (Mtb)[1]. While pulmonary infection has dominated research focus, Mtb pathogenesis extends far beyond the lung, including secondary lymphoid organs and other tissues[26]. Studies in mice have shown that Mtb first disseminates to the lung-draining mediastinal lymph node (medLN) beginning around eight days post-infection[30,32,118]. This seeding of the medLN triggers local initiation of T cell responses, which are essential for immune control[24,30,32,72,118,169]. Paradoxically, lung-draining lymph nodes often become a preferred site for Mtb persistence[45]. Historical human post-mortem studies from the pre-antibiotic era frequently recovered Mtb from lung-draining lymph nodes even when prior lung lesions appeared sterilized[46]. In human TB and non-human primate models, Mtb can even form granulomatous lesions within LNs that mimic those in the lung[170,171]. How these opposing processes — robust immune activation and persistent infection – can be supported within the same lymphoid organ represents a critical yet understudied aspect of TB pathogenesis.

Previous studies have suggested that initial transport of bacteria from lungs to lymph nodes is mediated by inflammatory monocytes (iMOs)[24], whereas conventional dendritic cells (cDCs) elicit T cell priming after acquiring Mtb antigens from these transporting iMOs[22,24,71,72]. However, the classical phenotypic markers used for binary classification or depletion of specific innate populations have proven insufficient to faithfully capture myeloid cell diversity or to isolate effects to select subsets[22,172-175]. Emerging evidence suggests that inflammatory conditions further blur conventional phenotypic boundaries, with cDC2 populations acquiring monocyte-like characteristics upon type I interferon stimulation, termed inflammatory cDC2s (inf-cDC2s)[174-176]. These inf-cDC2s express markers typically associated with inflammatory monocytes (CD64, CCR2, Ly6C) while also acquiring potent IL-12 production capacity typically associated with cDC1s[175], challenging simplified models of myeloid cell function during infection.

This cellular complexity is particularly relevant given the heterogeneous nature of CD4 T cell responses during Mtb infection. Recent work has identified functionally distinct T cell populations ranging from highly differentiated effector cells to less-differentiated stem-like cells, each with unique trafficking patterns and protective capacities[177-181]. While cDCs are recognized as the principal antigen-presenting cells for T cell priming[24,71,72,182], the specific cDC subsets that instruct different T cell fates remain unresolved. Moreover, work in vaccination and cutaneous infection models demonstrated that the spatial organization of innate cells within lymphoid organs generates distinct microenvironments specialized in promoting effector versus memory precursor T cell development[51,154,162,182], suggesting that tissue architecture critically shapes adaptive immune outcomes. Whether similar microenvironments arise during Mtb infection in the medLN and how they influence *de novo* T cell priming and effector fate decisions remains unknown.

The temporal dimension adds another layer of complexity to this process. Initiation of T cell priming has been shown to occur within the first few weeks of infection[169]. These activated T cells are sufficient to sustain continued responses throughout the course of infection[31], indicating potent generation of progenitor cells. Yet, certain vaccination studies have also suggested that initiation of effector versus memory progenitor states can be temporally encoded, with early activated cells preferentially generating effector cells while those activated later driving memory responses[183]. Whether the development of highly differentiated effector versus less-differentiated progenitor T cells occurs at distinct timepoints of Mtb infection, where the balance of available antigen and inflammatory cytokines is altered, has not been studied. Furthermore, how prior immune status, such as BCG vaccination, modulates this balance remains unknown. While BCG limits disseminated Mtb infection[184,185], its effects on LN-localized myeloid cell states and on naïve T cell priming within infected LNs have not been defined.

The limited understanding of how this critical immunological site functions across stages of infection underscores a fundamental paradox: How can lung-draining LNs both initiate protective immunity and provide a niche for long-term pathogen persistence? One explanation is that T cell priming and microbial persistence are spatiotemporally distinct events, supported by different cell types, tissue niches, and stages of infection. To address this, we combined

mouse models of aerosol Mtb infection with advanced imaging, multiparameter flow cytometry, single-cell transcriptomics, and mathematical modeling to dissect the spatial and temporal dynamics of infection and T cell priming in the medLN. We show that Mtb infection progressed through distinct temporal phases. The early phase (2-3 weeks) was characterized by initial dissemination of Mtb into medLNs via both iMOs and migratory cDCs, with cDCs driving potent Th1 priming amid widespread inflammatory cytokine signaling. By 3–4 weeks, however, the medLN underwent a striking structural transformation, with generation of large aggregates of monocyte-derived cells harboring multiple bacilli and occupying large portions of the parenchyma, including the T cell zone. These cells exhibited strong induction of inflammatory and microbicidal pathways yet failed to clear Mtb and persisted into late infection. Notably, T cells specific for major immunodominant antigens were unable to efficiently recognize infected monocytic aggregates. Lastly, BCG immunization perturbed monocytic niche formation and Mtb replication in medLNs without affecting initial lung-to-medLN trafficking or *de novo* T cell priming. Together, these findings demonstrate that despite a brief but robust window of T cell priming and inflammation, Mtb establishes a persistent, immunologically privileged myeloid niche within the very organs tasked with eliciting protective adaptive immune responses, reflecting an advanced strategy for immune evasion.

4.2 Results

4.2.1 Kinetics and Spatial Architecture of Mtb Infection in the medLN.

To define the myeloid landscape harboring Mtb in the medLN, we infected C57BL/6 mice with mCherry-expressing Mtb (H37Rv; 50-100 CFU) and performed a longitudinal analysis of infected cells by flow cytometry. Myeloid populations were defined as neutrophils ($Ly6G^{+}$), inflammatory monocytes (iMOs; $CD88^{+}SIRP\alpha^{+}CD64^{+}CD26^{LO}Ly6C^{HI}$), more differentiated monocyte-derived cells (MCs; $CD88^{+}SIRP\alpha^{+}CD64^{+}CD26^{LO}Ly6C^{INT\text{-}LO}$), and cDCs ($CD88^{-}CD26^{+}CD11c^{+}MHCII^{+}$), including resident ($CD11c^{HI}MHCII^{INT}$) and migratory ($CD11c^{INT}MHCII^{HI}$) subsets, further subdivided into cDC1 ($XCR1^{+}$) and cDC2 ($SIRP\alpha^{+}CCR2^{INT\text{-}LO}$) (Fig. S.1A).

Mtb dissemination from the lungs to the medLN has been reported as early as day 8 post-infection when assessed by culture[30,118]. By flow cytometry, however, Mtb-infected ($mCherry^{+}$) cells in the medLN could be reliably detected by day 15 post-infection (Fig. 1A, S.1A). Between

days 15 and 22, the number of infected medLN cells increased approximately ten-fold before plateauing at subsequent timepoints (days 28 and beyond), consistent with prior medLN CFU studies[30]. At day 15, Mtb was detected in cDCs (both cDC1 and cDC2) and iMOs (Fig. 1B). By contrast, at later timepoints (day 22 and 28), the infected cell compartment shifted markedly, with reduced cDC representation and a corresponding increase in iMOs and MCs (Fig. 1B). This redistribution was not explained by changes in the overall composition of innate cells in the medLN, as total numbers of cDCs, iMOs, and MCs were maintained or increased across these timepoints (Fig. S.1B). In contrast to the medLN, lung infection was characterized by preferential early infection of alveolar macrophages and neutrophils[20], underscoring tissue-specific features of myeloid infection dynamics. Notably, we observed a similar temporal transition in the representation of iMOs and MCs within Mtb-infected lungs, though this shift was less pronounced than in the medLNs, and cDCs remained a consistently minor infected population (Fig. S.1C). In line with prior reports[24,173-175,186], these myeloid populations also exhibited distinct levels of CCR2 expression (Fig. S.1A), with highest levels on iMOs and more heterogeneous expression among MCs and cDC2s.

We next studied the spatiotemporal dynamics of medLN infection using multiparameter confocal microscopy. At day 15 post-infection, individual Mtb bacilli were detected within dispersed myeloid cells ($CD11c^{+/-}SIRP\alpha^{+/-}$), which were primarily localized within the T cell zone (Fig. 1C). By contrast, just one week later (day 22 and after), we observed a dramatic expansion in bacterial burden (Fig. 1D), with bacilli now predominantly contained within large multicellular myeloid cell aggregates ($CD11c^{+}SIRP\alpha^{+}$) distributed throughout the T cell zone (Fig. 1C–F). These infected aggregates persisted for at least 110 days post-infection, suggesting the establishment of a long-lived niche for Mtb within the medLN (Fig. S.1D). Similar myeloid cell aggregates containing intracellular Mtb antigens (PPD staining) also formed in the T cell zone when using a more physiologically relevant ultra-low-dose (ULD; 1-3 CFU per mouse) infection model[14] (Fig. S1E), indicating that this phenotype is independent of infectious dose.

We further examined medLNs at day 34 post-infection in C3HeB/FeJ mice infected with a W-Beijing Mtb strain SA161. In this model, all mice infected with 50-100 CFU develop at least one large necrotic lung granuloma[69,187], characterized by dense $MPO^{+}CD11b^{HI}$ neutrophil aggregates

and loss of p120^{+} alveolar epithelium within the lesion (Fig. S.1F). We again observed similar myeloid cell aggregates containing Mtb antigens throughout the medLN T cell zone (Fig. S.1F), suggesting this biology is conserved across mouse and Mtb genotypes with different pulmonary pathologies.

Because CD11c and SIRPα can be expressed by both cDCs and monocyte-derived populations, we next used Zbtb46-GFP reporter mice to definitively trace cDC-lineage cells[149]. At day 15 post-infection, approximately 45% of Mtb bacilli in the medLN were localized within GFP^{+} cDCs, whereas only ~20% of Mtb^{+} were contained within GFP^{-} SIRPα^{+} cells, indicating cells of monocytic/macrophage origin (Fig. 1G–H). By day 22 and 28, however, the majority of Mtb bacilli were instead found within GFP^{-} SIRPα^{+} cells, while fewer than 10% of Mtb were within GFP^{+} cDCs. This temporal redistribution was also observed by flow cytometry (Fig. 1I–J).

Together, these data define at least two stages of Mtb infection within medLN myeloid cells. The first phase (~ day 15) is characterized by dispersed infiltration of the T cell zone by cDCs and MOs harboring single or few bacilli. This is followed by a second phase marked by the formation of monocyte-derived aggregates throughout the medLN parenchyma and especially the T cell zone and a concurrent increase in bacterial burden within these cells. The long-term persistence of these aggregates suggests they represent a stable niche for Mtb.

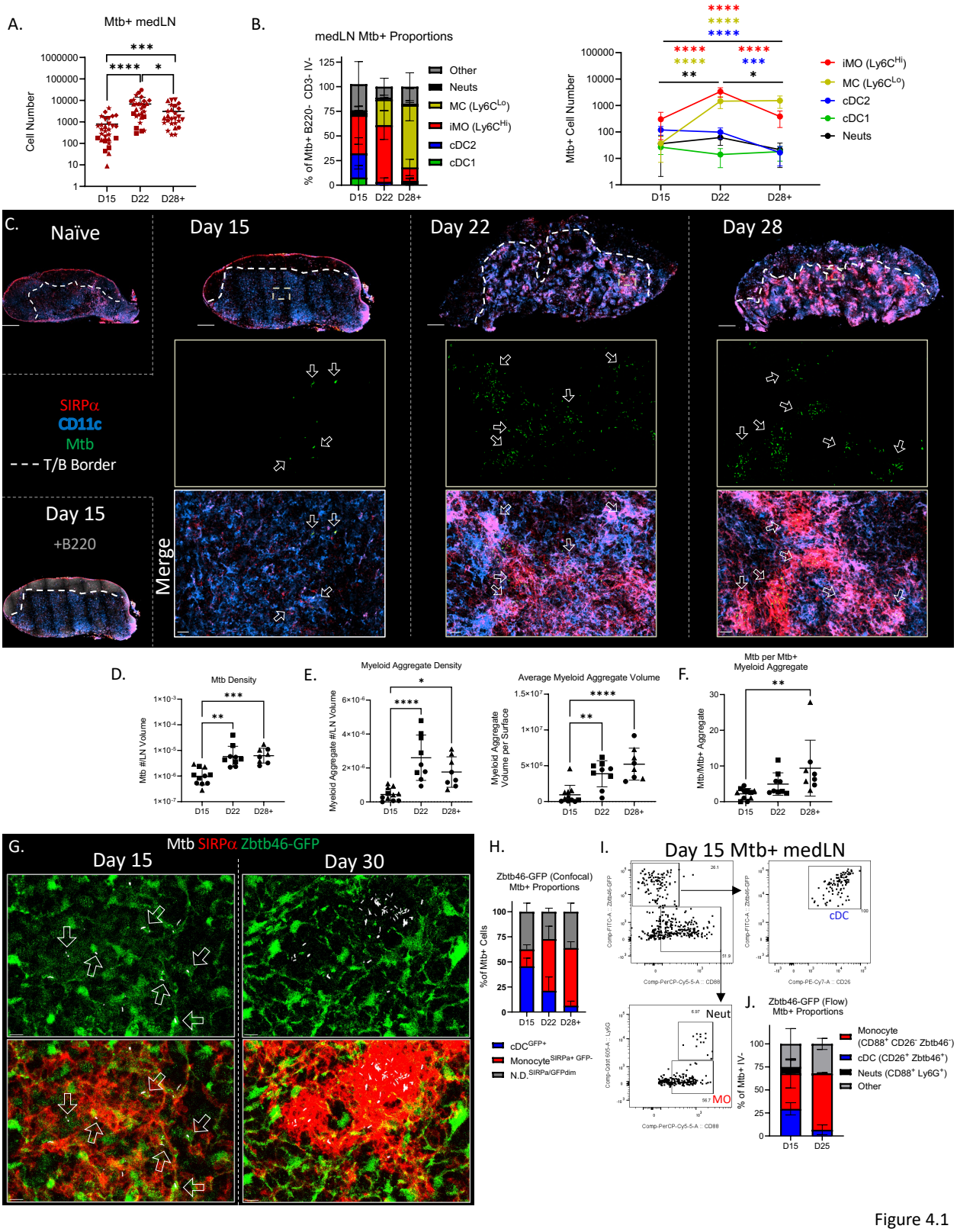
A.
Mtb+ medLN
Cell Number
D15 D22 D28+
B.
medLN Mtb+ Proportions
% of Mtb+ B220- CD3- IV-
Other
Neuts
MC (Ly6C^Lo)
iMO (Ly6C^Hi)
cDC2
cDC1
Mtb+ Cell Number
iMO (Ly6C^Hi)
MC (Ly6C^Lo)
cDC2
cDC1
Neuts
C.
Naïve
Day 15
Day 22
Day 28
SIRPα
CD11c
Mtb
T/B Border
Day 15
+B220
Merge
D.
Mtb Density
Mtb #/LN Volume
E.
Myeloid Aggregate Density
Myeloid Aggregate #/LN Volume
Average Myeloid Aggregate Volume
Myeloid Aggregate Volume per Surface
F.
Mtb per Mtb+ Myeloid Aggregate
Mtb/Mtb+ Aggregate
G.
Mtb SIRPα Zbtb46-GFP
Day 15
Day 30
H.
Zbtb46-GFP (Confocal) Mtb+ Proportions
%of Mtb+ Cells
cDC^GFP+
Monocyte^SIRPa+ GFP-
N.D.^SIRPa/GFPdim
I.
Day 15 Mtb+ medLN
cDC
Neut
MO
J.
Zbtb46-GFP (Flow) Mtb+ Proportions
% of Mtb+ IV-
Monocyte (CD88+ CD26- Zbtb46-)
cDC (CD26+ Zbtb46+)
Neuts (CD88+ Ly6G+)
Other
D15 D25

Figure 4.1

Figure 4.1: Mtb infection is initially harbored in cDCs and monocytes, and later in multicellular monocytic aggregates in the medLN

(A-F) C57Bl/6 mice were infected with Mtb H37Rv.mCherry at 50-100 CFU. (A-B) Flow cytometry analysis of medLNs from days 15 to 28+ (28-33) p.i. (A) Graphs shown reflect absolute numbers of innate cells per tissue, with gating strategy found in Fig. S1A. (B) Proportion of Mtb^+ innate cells in the medLN shown as a fraction of $B220^-CD3^-IV^-Mtb^+$ events. Cell numbers are shown as mean with 95% confidence intervals. Data represent 6 independent experiments, identified by symbol shape where applicable (N=26-30 mice). (C-F) Confocal microscopy of myeloid cells in naïve and Mtb-infected medLNs at D15-D28+ (C), with quantification of Mtb density (D), myeloid aggregate density and volume (E), and Mtb bacilli per Mtb^+ myeloid aggregate (F). Data represent 3 independent experiments, identified by symbol shape (N=7-11 mice). The T/B border (dotted line) was defined based on B220 staining (example in bottom left). Arrows indicate infected cells or aggregates. Scale bars: 300 µM (zoom-out); 20 µM (zoom-in). (G-J) Zbtb46-GFP mice (N=5) were infected with aerosolized Mtb H37Rv mCherry at ~100 CFU. (G-H) Imaging of D15 and D28+ p.i. medLNs. Mtb surfaces were assigned to cDCs ($Zbtb46\text{-}GFP^+$) or MOs ($Zbtb46\text{-}GFP^-$ $SIRP\alpha^+$). Not determined (N.D.) indicates dim Zbtb46-GFP or SIRPa signals. Scale bars: 10 µM. (I-J) Flow cytometry analysis and quantification of D15 and D25 p.i. Zbtb46-GFP medLNs, identifying Mtb-infected cDCs ($Zbtb46\text{-}GFP^+CD88^-CD26^+$) and Monocytes ($CD88^+$ $Zbtb46\text{-}GFP^-$). Statistical results for significance were measured by Kruskal-Wallis Test with Dunn's Multiple Comparisons (A, D) or ordinary one-way ANOVA using multiple comparisons with Tukey's Correction (B, E, F).

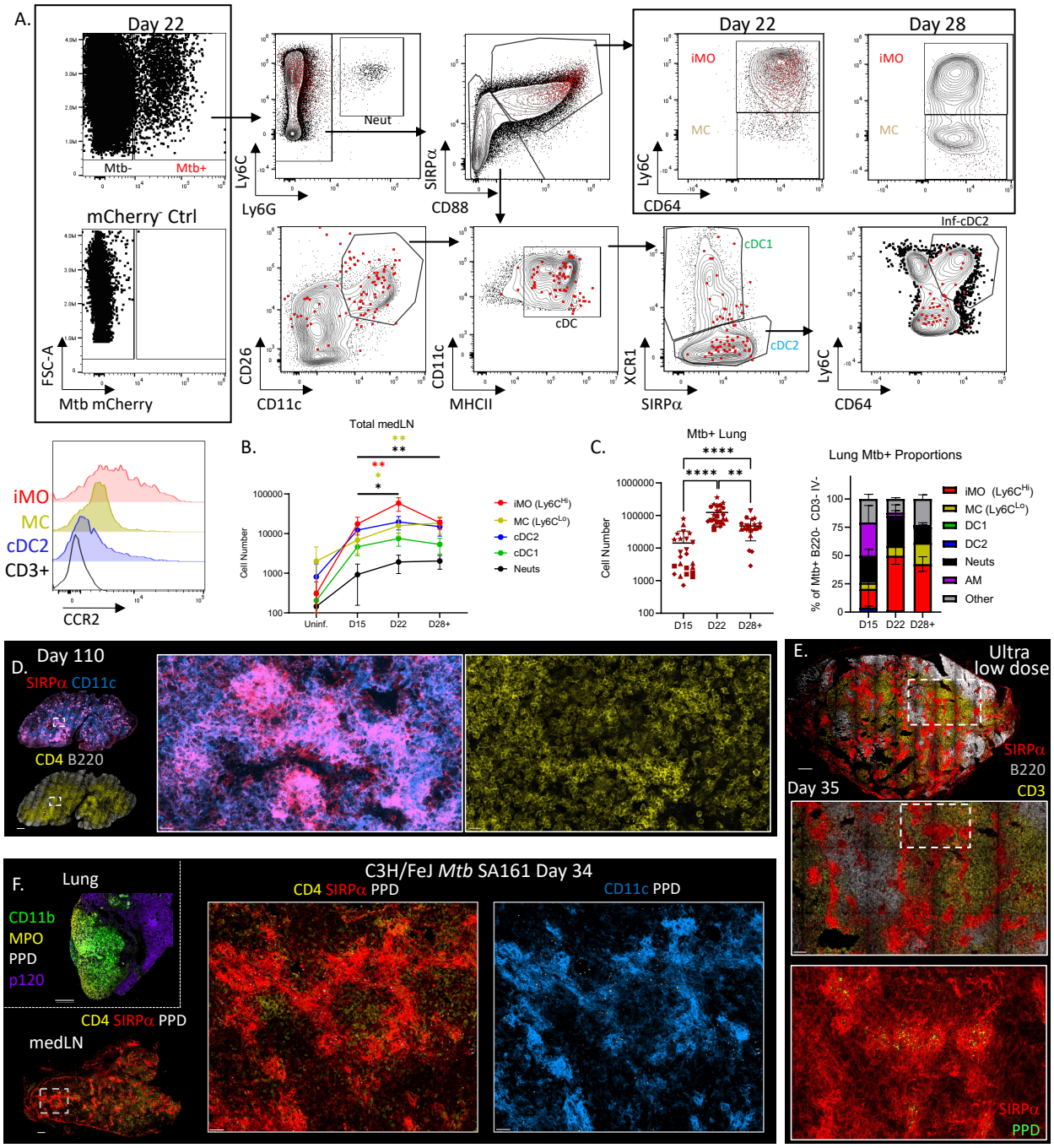
A.
Day 22
Mtb-
Mtb+
mCherry- Ctrl
FSC-A
Mtb mCherry
Ly6G
Ly6C
Neut
SIRPα
CD88
Day 22
Day 28
iMO
MC
Ly6C
CD64
CD26
CD11c
CD11c
MHCII
cDC
cDC1
cDC2
XCR1
SIRPα
Inf-cDC2
Ly6C
CD64
iMO
MC
cDC2
CD3+
CCR2
B.
Total medLN
Cell Number
Uninf.
D15
D22
D28+
iMO (Ly6C^Hi)
MC (Ly6C^Lo)
cDC2
cDC1
Neuts
C.
Mtb+ Lung
Cell Number
D15
D22
D28+
Lung Mtb+ Proportions
% of Mtb+ B220- CD3- IV-
iMO (Ly6C^Hi)
MC (Ly6C^Lo)
DC1
DC2
Neuts
AM
Other
D15
D22
D28+
D.
Day 110
SIRPα CD11c
CD4 B220
E.
Ultra low dose
SIRPα
B220
CD3
Day 35
F.
Lung
CD11b
MPO
PPD
p120
CD4 SIRPα PPD
medLN
C3H/FeJ Mtb SA161 Day 34
CD4 SIRPα PPD
CD11c PPD
SIRPα
PPD

Figure 4.S.1

Figure 4.S.1: Mtb infections across mouse models reflect dynamic changes in innate cell populations

Data related to Fig. 1. (A-D). (A) Gating strategy for Mtb^- (black contour plot) and Mtb^+ (red dot plot) innate cells. D22 medLN sample shown, unless otherwise noted, with prior gating on Lymphocytes/Single Cells/Live/IV^-/$B220^-$/$CD3^-$. CCR2 histograms show expression in indicated populations for D15 medLN. (B) Absolute total innate cell numbers per medLN; shown as mean with 95% confidence intervals. (C) Flow cytometry enumeration of Mtb^+ innate cells in lung samples from D15 to D28+ p.i. Proportion of Mtb^+ innate cells in the medLN shown as a fraction of $B220^-CD3^-IV^-Mtb^+$ events and reflect innate gating as in Fig. S1A, with additional gating for alveolar macrophages (AM) characterized as $SiglecF^+$ $CD11c^+$. (D) Confocal microscopy of medLN at D110 p.i., visualizing myeloid cells (CD11c, SIRPa) and T/B cell zones (B220, CD4). Scale bars: 20 uM. (E) Representative ultra-low-dose (ULD) infected medLN at D35 p.i. showing myeloid aggregates (SIRPα), T/B cell zones (B220, CD3), and Mtb (PPD). (F) C3H/FeJ mouse infected at D34 p.i. with SA161 Mtb strain (50-100 CFU), showing linked lung and medLN tissues. Lung tissue shows neutrophils (MPO), myeloid cells (CD11b), Mtb antigen (PPD), and epithelium (p120). MedLN shows myeloid cells (SIRPa), T zone (CD4), and Mtb antigen (PPD). Statistical results for significance were measured by or ordinary one-way ANOVA (B) using multiple comparisons with Tukey's Correction or by Kruskal-Wallis Test with Dunn's Multiple Comparisons (C).

4.2.2 A Cross-Organ, Cross-Timepoint Atlas of Innate Cell Dynamics During Mtb Infection

To better define how innate cells change across tissues during Mtb infection, we next generated a single-cell transcriptional atlas spanning lung, medLN, and blood at early (day 15) and later (day 28) stages of infection, two timepoints associated with distinct cellular and structural features in the medLN, alongside naïve baselines (day 0). We profiled both Mtb-infected ($mCherry^{+}$) and uninfected bystander ($mCherry^{-}$) parenchymally localized (IV^{-}) innate immune cells from the lung and medLN. In the blood, we assessed only uninfected cells due to rarity of Mtb-infected populations. This yielded 93,145 high-quality cells for downstream analysis. Cell identities were assigned using ImmGen-based references with manual label refinement informed by curated lineage markers consistent with prior flow cytometry analysis (Fig. 2A, Fig. S2A; Table S.1).

In uninfected ($mCherry^{-}$) cells, each tissue exhibited distinct and temporally dynamic phenotypes. In the lung, naïve samples contained relatively few monocytes identified by expression of Nr4a1, Csf1r, Ly6c2, Ccr2, Fcgr1, whereas by day 28 there was pronounced enrichment of inflammatory monocyte 2 (iMO2) cells ($Ly6c2^{Int}Ccr2^{Int}Ly6i^{Hi}$) and the emergence of monocyte-derived cells (MCs). MCs expressed Mitf and Sirpa along with MHC and C1q-associated genes, a signature linked to tissue-regenerative interstitial macrophages during Mtb infection[188-190] and reported as a biomarker for TB disease in patients[191] (Fig. 2A, Fig. S2A–C).

In the medLN, naïve samples were dominated by cDC populations, including resident ($Ccr7^{-}$ $Fscn1^{-}$) and migratory ($Ccr7^{+}Fscn1^{+}$) cDC1s ($Irf8^{+}Xcr1^{+}Clec9a^{+}$) and cDC2s ($Irf4^{+}$ $Xcr1^{-}$), and $Irf4^{-}Irf8^{-}Cd11b^{-}$ DCs (here termed transitional DCs)[192] (Fig. 2A, S.2C). By day 15, however, the medLN composition shifted toward monocytic dominance, with expansion of iMO1, iMO2, and MC populations, suggesting early recruitment of blood-derived myeloid cells into the lymph node. Consistent with this, in the blood, uninfected cells were dominated by circulating monocyte subsets, including iMO1 ($Ly6c2^{Hi}Ccr2^{Hi}$), iMO2, iMO3 ($Ly6c2^{LO}Ccr2^{LO}$), and patrolling monocytes (pMOs, $Pou2f2^{+}Ly6c2^{-}$), alongside neutrophils and a smaller representation of cDC2s. Notably, iMO3 cells increased at day 15, followed by expansion of iMO2 cells at day 28, suggesting sustained monocytosis throughout infection (Fig. 2A, S.2B).

Analysis of Mtb-infected (mCherry$^+$) cells revealed pronounced tissue- and time-dependent transitions. In the lung, infected cells at day 15 were dominated by alveolar macrophages (AMs) and neutrophils, along with with monocyte-derived populations, but with minimal representation of cDCs. By day 28, infected lungs showed expansion of iMO2s and, to a lesser extent, MCs (Fig. 2A–B). By contrast, infected medLNs at day 15 contained a heterogeneous mixture of iMOs, MCs, and cDCs, consistent with flow cytometry and imaging analyses. By day 28, the infected medLN compartment became overwhelmingly dominated by iMO2s and MCs, with a marked reduction in infected cDCs, indicating a transition from early cDC involvement to monocyte-derived dominance.

To confirm that the monocyte-derived populations observed by scRNA-seq corresponded with the monocytic aggregates observed by imaging and flow cytometry, we examined lineage-associated transcriptional features. Compared to iMO1 and iMO2 cells, MCs showed reduced expression of Ly6c2 and Ccr2 (Fig. S.2C), consistent with loss of circulating monocyte characteristics and with surface marker flow-based profiles (Fig. S.1A). In contrast, infected MCs, and to a lesser extent iMO2s, exhibited increased expression of Cd68, Vcam1, and Mertk, genes associated with phagocytic capacity and tissue residency[193,194] (Fig. S.2D). These transcriptional features were mirrored at the protein level, as MerTK, VCAM1, and CD68 were enriched within the multicellular aggregates observed in the medLN by confocal microscopy (Fig. S.2E).

To assess potential developmental relationships within the monocyte lineage, we performed Slingshot trajectory analysis[161] on all monocytic cells across tissues (Fig. S.2F). This revealed a continuum of circulating to tissue-associated states. Pseudotime starting points were defined as naïve pMOs and iMO1s[195]. Notably, iMO3 cells, enriched in blood at day 15, also demonstrated low pseudotime scores, consistent with an early myelopoietic response to infection. In contrast, iMO2s occupied intermediate positions, and MCs displayed the highest pseudotime scores, suggesting the latter represent the most differentiated monocyte derived cell population.

Together, these data define a temporally coordinated remodeling of Mtb-infected myeloid niches across lung and medLN characterized by early recruitment of inflammatory monocytes and monocyte-derived cells that dominate infected compartments at later stages. Notably, this

transition occurs more rapidly in the medLN than in the lung. While cDCs transiently contribute to early medLN infection, they are progressively excluded as monocyte-derived aggregates establish dominance.

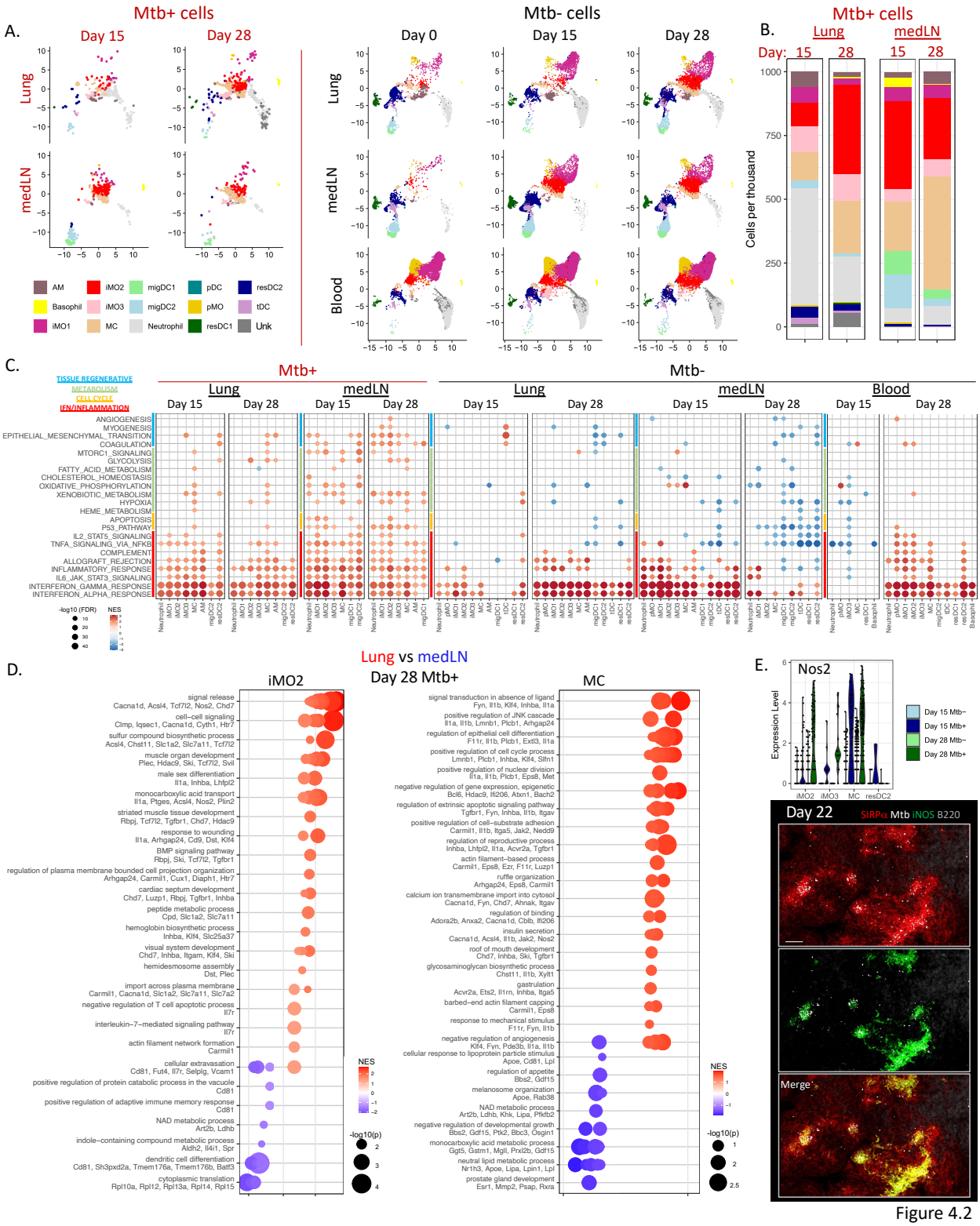
A.
Mtb+ cells
Day 15
Day 28
Lung
medLN
Mtb- cells
Day 0
Day 15
Day 28
Lung
medLN
Blood
AM
Basophil
iMO1
iMO2
iMO3
MC
migDC1
migDC2
Neutrophil
pDC
pMO
resDC1
resDC2
tDC
Unk
B.
Mtb+ cells
Lung
medLN
Day: 15 28 15 28
Cells per thousand
C.
Mtb+
Mtb-
Lung
medLN
Blood
Day 15
Day 28
TISSUE REGENERATIVE
METABOLISM
CELL CYCLE
IFN/INFLAMMATION
ANGIOGENESIS
MYOGENESIS
EPITHELIAL_MESENCHYMAL_TRANSITION
COAGULATION
MTORC1_SIGNALING
GLYCOLYSIS
FATTY_ACID_METABOLISM
CHOLESTEROL_HOMEOSTASIS
OXIDATIVE_PHOSPHORYLATION
XENOBIOTIC_METABOLISM
HYPOXIA
HEME_METABOLISM
APOPTOSIS
P53_PATHWAY
IL2_STAT5_SIGNALING
TNFA_SIGNALING_VIA_NFKB
COMPLEMENT
ALLOGRAFT_REJECTION
INFLAMMATORY_RESPONSE
IL6_JAK_STAT3_SIGNALING
INTERFERON_GAMMA_RESPONSE
INTERFERON_ALPHA_RESPONSE
-log10 (FDR)
NES
D.
Lung vs medLN
Day 28 Mtb+
iMO2
MC
signal release
Cacna1d, Acsl4, Tcf7l2, Nos2, Chd7
cell–cell signaling
Clmp, Iqsec1, Cacna1d, Cyth1, Htr7
sulfur compound biosynthetic process
Acsl4, Chst11, Slc1a2, Slc7a11, Tcf7l2
muscle organ development
Plec, Hdac9, Ski, Tcf7l2, Svil
male sex differentiation
Il1a, Inhba, Lhfpl2
monocarboxylic acid transport
Il1a, Ptges, Acsl4, Nos2, Plin2
striated muscle tissue development
Rbpj, Tcf7l2, Tgfbr1, Chd7, Hdac9
response to wounding
Il1a, Arhgap24, Cd9, Dst, Klf4
BMP signaling pathway
Rbpj, Ski, Tcf7l2, Tgfbr1
regulation of plasma membrane bounded cell projection organization
Arhgap24, Carmil1, Cux1, Diaph1, Htr7
cardiac septum development
Chd7, Luzp1, Rbpj, Tgfbr1, Inhba
peptide metabolic process
Cpd, Slc1a2, Slc7a11
hemoglobin biosynthetic process
Inhba, Klf4, Slc25a37
visual system development
Chd7, Inhba, Itgam, Klf4, Ski
hemidesmosome assembly
Dst, Plec
import across plasma membrane
Carmil1, Cacna1d, Slc1a2, Slc7a11, Slc7a2
negative regulation of T cell apoptotic process
Il7r
interleukin–7–mediated signaling pathway
Il7r
actin filament network formation
Carmil1
cellular extravasation
Cd81, Fut4, Il7r, Selplg, Vcam1
positive regulation of protein catabolic process in the vacuole
Cd81
positive regulation of adaptive immune memory response
Cd81
NAD metabolic process
Art2b, Ldhb
indole–containing compound metabolic process
Aldh2, Il4i1, Spr
dendritic cell differentiation
Cd81, Sh3pxd2a, Tmem176a, Tmem176b, Batf3
cytoplasmic translation
Rpl10a, Rpl12, Rpl13a, Rpl14, Rpl15
NES
-log10(p)
signal transduction in absence of ligand
Fyn, Il1b, Klf4, Inhba, Il1a
positive regulation of JNK cascade
Il1a, Il1b, Lmnb1, Plcb1, Arhgap24
regulation of epithelial cell differentiation
F11r, Il1b, Plcb1, Ext3, Il1a
positive regulation of cell cycle process
Lmnb1, Plcb1, Inhba, Klf4, Sftn1
positive regulation of nuclear division
Il1a, Il1b, Plcb1, Eps8, Met
negative regulation of gene expression, epigenetic
Bcl6, Hdac9, Ifi206, Atxn1, Bach2
regulation of extrinsic apoptotic signaling pathway
Tgfbr1, Fyn, Inhba, Il1b, Itgav
positive regulation of cell–substrate adhesion
Carmil1, Il1b, Itga5, Jak2, Nedd9
regulation of reproductive process
Inhba, Lhfpl2, Il1a, Acvr2a, Tgfbr1
actin filament–based process
Carmil1, Eps8, Ezr, F11r, Luzp1
ruffle organization
Arhgap24, Eps8, Carmil1
calcium ion transmembrane import into cytosol
Cacna1d, Fyn, Chd7, Ahnak, Itgav
regulation of binding
Adora2b, Anxa2, Cacna1d, Cblb, Ifi206
insulin secretion
Cacna1d, Acsl4, Il1b, Jak2, Nos2
roof of mouth development
Chd7, Inhba, Ski, Tgfbr1
glycosaminoglycan biosynthetic process
Chst11, Il1b, Xylt1
gastrulation
Acvr2a, Ets2, Il1rn, Inhba, Itga5
barbed–end actin filament capping
Carmil1, Eps8
response to mechanical stimulus
F11r, Fyn, Il1b
negative regulation of angiogenesis
Klf4, Fyn, Pde3b, Il1a, Il1b
cellular response to lipoprotein particle stimulus
Apoe, Cd81, Lpl
regulation of appetite
Bbs2, Gdf15
melanosome organization
Apoe, Rab38
NAD metabolic process
Art2b, Ldhb, Khk, Lipa, Pfkfb2
negative regulation of developmental growth
Bbs2, Gdf15, Ptk2, Btc3, Osgin1
monocarboxylic acid metabolic process
Ggt5, Gstm1, Mgll, Prxl2b, Gdf15
neutral lipid metabolic process
Nr1h3, Apoe, Lipa, Lpin1, Lpl
prostate gland development
Esr1, Mmp2, Psap, Rxra
E.
Nos2
Expression Level
iMO2
iMO3
MC
resDC2
Day 15 Mtb–
Day 15 Mtb+
Day 28 Mtb–
Day 28 Mtb+
Day 22
SIRPα Mtb iNOS B220
Merge

Figure 4.2

Figure 4.2: Defining transcriptional transitions in the Mtb-infected myeloid compartment

Lungs, medLNs, and blood from mice (N=16 for D15 and 28; N=3 for D0) were sorted for Mtb mCherry^{+} and bystander mCherry^{-} myeloid cells for 10X single cell RNAseq at D0, D15, and D28 p.i. (50-100 CFU) (A) UMAP clustering color coded by myeloid phenotype for each tissue type, timepoint, and infection status. (B) Proportion plots of indicated Mtb-infected cell types in the medLN and lung. (C) mSigDB Hallmark GSEA for selected pathways by cell type, infection, and timepoint, as compared to D0 for each cell type/tissue. Colored bars indicate curated groupings for selected pathways related to interferon signaling and inflammation (red), cell cycle (orange), metabolism (green), and tissue regeneration (cyan). (D) GO:BP GSEA pathway enrichment of Mtb-infected iMO2s and MCs at D28, comparing lung versus medLN. Top shared leading edge genes are shown under each parent term. (E) Nos2 expression among indicated Mtb^{+} and Mtb^{-} medLN populations and confocal microscopy of iNOS expression at D22 p.i. Scale bar: 20 μM.

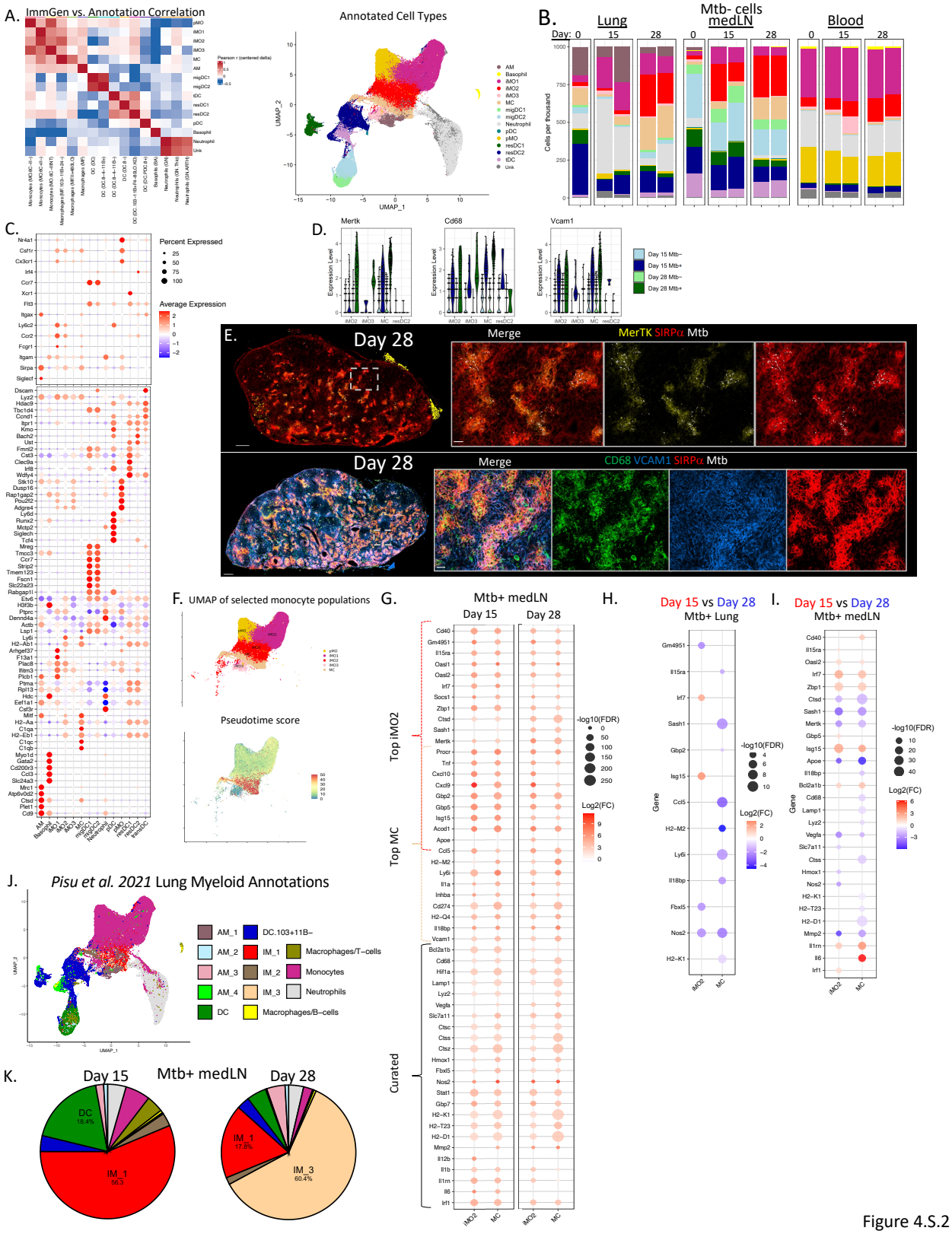
A. ImmGen vs. Annotation Correlation
Annotated Cell Types
B.
Lung
Mtb- cells medLN
Blood
Day: 0
15
28
Cells per thousand
C.
Percent Expressed
Average Expression
D.
Mertk
Cd68
Vcam1
Expression Level
Day 15 Mtb−
Day 15 Mtb+
Day 28 Mtb−
Day 28 Mtb+
E.
Day 28
Merge
MerTK SIRPα Mtb
CD68 VCAM1 SIRPα Mtb
F. UMAP of selected monocyte populations
Pseudotime score
G.
Mtb+ medLN
Day 15
Day 28
Top iMO2
Top MC
Curated
-log10(FDR)
Log2(FC)
H.
Day 15 vs Day 28
Mtb+ Lung
I.
Day 15 vs Day 28
Mtb+ medLN
J.
Pisu et al. 2021 Lung Myeloid Annotations
AM_1
AM_2
AM_3
AM_4
DC
DC.103+11B−
IM_1
IM_2
IM_3
Macrophages/T−cells
Monocytes
Neutrophils
Macrophages/B−cells
K.
Mtb+ medLN
Day 15
Day 28
DC
18.4%
IM_1
56.3
IM_1
17.8%
IM_3
60.4%

Figure 4.S.2

Figure 4.S.2: Proportions and pathway changes across tissue and time during Mtb infection

Data related to Fig. 2 (A) Pearson correlation plot for ImmGen data browser (X-axis) and curated (Y-axis) annotations (left). UMAP of all cells color coded based on curated cell type annotations (right). (B) Proportion plots of Mtb^- 'bystander' cells for indicated timepoints and tissues, with replicate samples shown. (C) Curated genes (Top) and Top 5 DEGs (bottom) for each innate cell type used for characterization. (D-E) Markers selectively upregulated by Mtb-infected MCs compared to other populations. (E) Scale bar: 200 µM (zoom-out), 20 µM (zoom-in). (F) UMAP (top) and pseudotime (bottom) analysis of monocyte subclusters (pMO, iMO1, iMO2, iMO3, MC) used for trajectory analysis. Pseudotime scores plotted on the overall UMAP space (bottom). (G-I) Top DEGs for Mtb-infected iMO2s and MCs versus D0 counterparts, and additional curated genes related to mSigDB Hallmark pathway GSEA, showing medLN Mtb-infected iMO2 and MC populations D15 and D28 vs D0 (G) or D15 vs D28 for lung (H) and medLN (I). log2FC>0.5, FDR<0.05. (J-K) Lung myeloid annotations transferred from Pisu et al. 2021 projected onto the overall UMAP (J) and proportion plots for Mtb-infected medLN at D15 and D28 (K).

4.2.3 Differential Gene Expression and Pathway Enrichment Reveal Functional Remodeling of Monocytic Populations

To define the functional programs associated with infection across tissues, we examined differentially expressed genes (DEGs) relative to naïve (day 0) baselines separately for Mtb-infected (mCherry$^+$) and uninfected bystander (mCherry$^-$) cells, followed by pathway-level Gene Set Enrichment Analysis (GSEA). This approach revealed marked tissue- and time-dependent remodeling of inflammatory and metabolic pathways in both infected and uninfected subsets (Fig. 2C; Data S.1–2). Among uninfected bystander cells in the lung, myeloid populations showed limited transcriptional changes on day 15, followed by pronounced enrichment of interferon-associated and inflammatory pathways by day 28. A similar pattern was observed in the blood, with minimal transcriptional changes at day 15 but prominent induction of IFN-I and IFN-II responses, TNFα signaling, IL6/JAK/STAT3 signaling, complement, and inflammatory response pathways by day 28, consistent with the emergence of systemic inflammation at this later timepoint. In contrast, in the medLN, uninfected bystander cells exhibited robust enrichment of inflammatory cytokine signaling pathways, including IFN-I, IFN-II, and TNFα, already at day 15. Notably, by day 28, several of these pathways, including TNFα signaling and p53-associated programs, were attenuated relative to naïve controls, indicating induction of a transient inflammatory state within the medLN.

When examining Mtb-infected populations relative to naïve cells, we observed markedly elevated induction of inflammatory pathways that were apparent in both lungs and medLNs at day 15 and day 28 (Fig. 2C), indicating robust pathogen sensing and associated inflammatory cytokines in both organs. Hypoxia was also induced in infected MCs and iMO2s. Some tissue-specific differences did emerge, with the infected medLN cells showing enrichment of xenobiotic metabolism and p53-associated pathways, and induction of tissue remodeling and repair pathways on day 28. We also observed temporal shifts in metabolic pathway induction. Oxidative phosphorylation and mTORC1 signaling were preferentially enriched in infected MCs at day 15, whereas glycolysis, hypoxia, fatty acid metabolism, and heme metabolism pathways were more prominent at day 28 of infection.

These pathway-level findings were supported by DEG analysis of the two most abundant Mtb-infected populations, iMO2s and MCs (Fig. S.2G). Compared to naïve cells, infected cells in both the lung and medLN upregulated genes associated with interferon responsiveness (Nos2, Gbp2, Gbp7, Cxcl9, Cxcl10), antigen presentation (H2-K1, H2-Ab1, H2-M2, H2-Q4), hypoxia and metabolic adaptation (Hif1a, Slc7a11, Fabp5, Acod1), and immune regulation (Il18bp, Cd274, Inhba). Comparison of DEGs between timepoints demonstrated that in the lung, infected iMO2s and MCs exhibited relatively limited transcriptional differences between day 15 and day 28, with the later timepoint characterized by modest increases in interferon-associated genes, particularly within MCs (Fig. S2H). In the medLN, infected cells displayed a temporal shift in transcriptional programs (Fig. S2I). Genes enriched at day 15 included interferon-stimulated genes (Isg15, Irf1, Irf7, Oasl2, Zbp1), inflammatory mediators (Il6, Il1rn, Il15ra), and activation and survival markers (Cd40, Bcl2a1b). By day 28, medLN-infected cells showed DEGs associated with wound healing (Vegfa, Mertk, Sash1), phagocytosis and efferocytosis (Cd68, Lyz2, Ctsd, Ctss, Lamp1), and metabolic adaptation (Apoe, Slc7a11, Nos2).

We also examined tissue-specific differences between lung and medLN infected iMO2s and MCs at a matched timepoint, day 28 (Fig. 2D). Gene Ontology (Biological Process) enrichment analysis (GO:BP) demonstrated that in the lung, MCs were preferentially enriched for cell signaling and cell cycle–associated pathways, while iMO2s showed greater enrichment for wound response and tissue development pathways. In contrast, in the medLN, infected iMO2s and MCs were enriched for metabolic pathways, including NAD metabolism, monocarboxylic acid processing, and neutral lipid metabolism, consistent with metabolic reprogramming during Mtb infection[196]. Together, these data highlight tissue-specific differences in myeloid cells during infection.

We observed robust induction of IFN-γ–associated genes within infected medLN populations. In particular, Nos2 (encoding iNOS), an IFN-γ induced effector which mediates bactericidal activity and Mtb control but can also regulate inflammation[80,89,197], was upregulated in infected MCs and iMO2s at day 15 and 28 (Fig. 2E, S.2G). Immunofluorescence microscopy confirmed abundant iNOS within Mtb-containing myeloid aggregates in the medLN (Fig. 2E). Thus, despite

the well-established role of IFN-γ signaling in Mtb control[82,84,198], it's induction in the medLN is insufficient for bacterial clearance.

Consistent with our findings, prior single-cell analyses of lung myeloid cells during Mtb infection identified an infected interstitial macrophage population (IM_3) characterized by high Nos2 expression and signatures of iron metabolism[190]. We found transcriptional concordance between the MC population defined here and the previously described IM_3s, and these cells constituted the dominant infected cell population by day 28 (Fig. S.2J-K). Notably, the prior study demonstrated that IM_3 cells harbored Mtb expressing a DosR stress-response reporter[95,96], suggesting that the MCs identified here may similarly support bacterial persistence.

Collectively, these data demonstrate that Mtb infection induces a temporally structured myeloid response within the medLN. Early infection (day 15) is characterized by largescale induction of inflammatory cytokine and interferon-associated programs across both infected and bystander populations. By day 28, this inflammatory state is attenuated and replaced by a transcriptional program enriched for metabolic adaptation, hypoxia, and tissue remodeling within Mtb-infected myeloid aggregates, consistent with establishment of a persistent, pathogen-permissive niche. These shifts appear temporally different from those in the lung, which demonstrate progressive increases in inflammation across examined timepoints.

4.2.4 Tracking Infected Cell Origin and Mtb Replication in the medLN

We next aimed to define the anatomical source of Mtb-infected myeloid cells in the medLN, particularly during the exponential phase of bacterial growth and the emergence of myeloid aggregates. To track myeloid cell migration from the lung and blood to the medLN during infection, we combined intratracheal[199] and serial-intravascular (sIVs)[54,200,201] labeling strategies to distinguish lung-derived and blood-derived cells within the medLN parenchyma (Fig. 3A). Ovalbumin–Alexa-Fluor-488 (OVA-488) was administered intratracheally 24 hours prior to tissue harvest to label lung myeloid cells that subsequently migrated to the medLN, while two temporally separated intravenous CD45.2 antibody injections (24 hours and 5 minutes before euthanasia) distinguished cells entering the medLN via the blood vasculature. This approach

enabled identification of medLN parenchymal cells (BV421$^-$) that had recently migrated either from the lung (OVA-488$^+$) or from circulation (APC$^+$) (Fig. 3B, Fig. S3A–C)[54,200,202].

Infection resulted in a 5-10 fold increase in the number of OVA-488$^+$ myeloid cells migrating from the lung to medLN over a 24h period, though only a minor fraction of these cells (1-2%) harbored Mtb (mCherry$^+$) (Fig. 3C). The number of lung-to-medLN migrating myeloid cells modestly increased but remained stable over the course of infection, peaking by day 30 with nearly 10^4 myeloid cells migrating in 24h (Fig. 3C). In contrast, the number of blood-derived myeloid cells (APC$^+$) entering medLN during the 24h labeling period increased nearly 1000-fold relative to naïve controls, becoming evident by day 15 post-infection, peaking at day 22, and declining by day 30 (Fig. 3D). A modestly larger fraction of blood-derived cells was Mtb-infected (~0.5–10%) compared with lung-derived cells. Because most blood-derived cells are unlikely to be infected before entering the medLN, these data suggest that large numbers of myeloid cells are recruited from the blood, followed by a small subset becoming infected locally. Consistent with this, the absolute numbers of blood-derived Mtb-infected cells remained relatively low throughout infection, accounting on average for ~3% of all Mtb-infected cells in the medLN.

Analysis of cellular phenotypes for lung-derived populations revealed temporal shifts in composition. Early day 15 medLN seeding involved both iMOs and cDCs carrying Mtb from the lungs, similar to the total Mtb-infected cells in the medLN (Fig. 3E-G). However, at later timepoints (after day 22), most lung-derived Mtb-infected cells were comprised of MCs (Fig. 3E), while uninfected lung-derived cells still included large numbers of cDC2 (Fig. S.3D). sIVs-labeled blood-derived Mtb-infected cells showed similar patterns, with early involvement of both cDCs and iMOs, and with enhanced MC enrichment at later timepoints (Fig. 3F, 3G). The presence of sIVs-labeled cDCs in infected and uninfected fractions may reflect partial labeling of perivascular cDCs[60] or inflammation-induced DCpoiesis[55], the latter being consistent with our scRNA-seq data revealing circulating and transitional cDCs during infection (Fig. 2A).

These findings indicate that bacterial transport to the medLN occurs relatively infrequently and does not directly correlate with the rapid rise in bacterial burdens in the medLN. To formally assess the contribution of lung-derived Mtb-infected myeloid cells to medLN infection, we

developed a mathematical model incorporating cell migration and bacterial replication (Fig. 3H, Methods eqns (11)-(15)). The initial model permitted Mtb replication in the lung and migration of Mtb-infected cells from the lung to medLN and was fit to experimentally measured cell numbers. Because detection of infected cells was limited at early timepoints, we used models with less constrained fits to capture the observed dynamics.

The best-fitting model accurately recapitulated the accumulation, peak, and early decline in the number of Mtb^+ myeloid cells in the lung (Fig. S.3E), and required lung-to-medLN migration rates to vary over time in a step-like manner (Fig. S.3F). However, when applied to a medLN model where Mtb^+ cells accumulated in the medLN solely through migration from the lung without local replication (i.e., replication rate r_N=0/day), this failed to accurately reproduce the rapid rise in the number of Mtb^+ cells from days 15 to 22 post-infection (Fig. 3I). We therefore extended the model to allow for Mtb replication within the medLN. We found that incorporating relatively high Mtb replication rates (r=0.5-0.7/day or doubling times of 29-33 hours) enabled the model to closely match the observed medLN infection dynamics (Fig. 3I). Notably, this estimated rate of Mtb replication in the medLN was similar to that in the lung (Fig. 3I, S3E).

These modeling results align with our medLN microscopy observations which revealed early (day 15) detection of single Mtb bacilli within individual cells, followed at later timepoints by the accumulation of myeloid aggregates containing numerous bacilli. Together, these findings support a model in which initial Mtb dissemination to medLNs occurs via relatively low-frequency trafficking from the lung by cDCs and iMOs, followed by monocyte recruitment from the blood and substantial local bacterial replication within monocyte-derived aggregates.

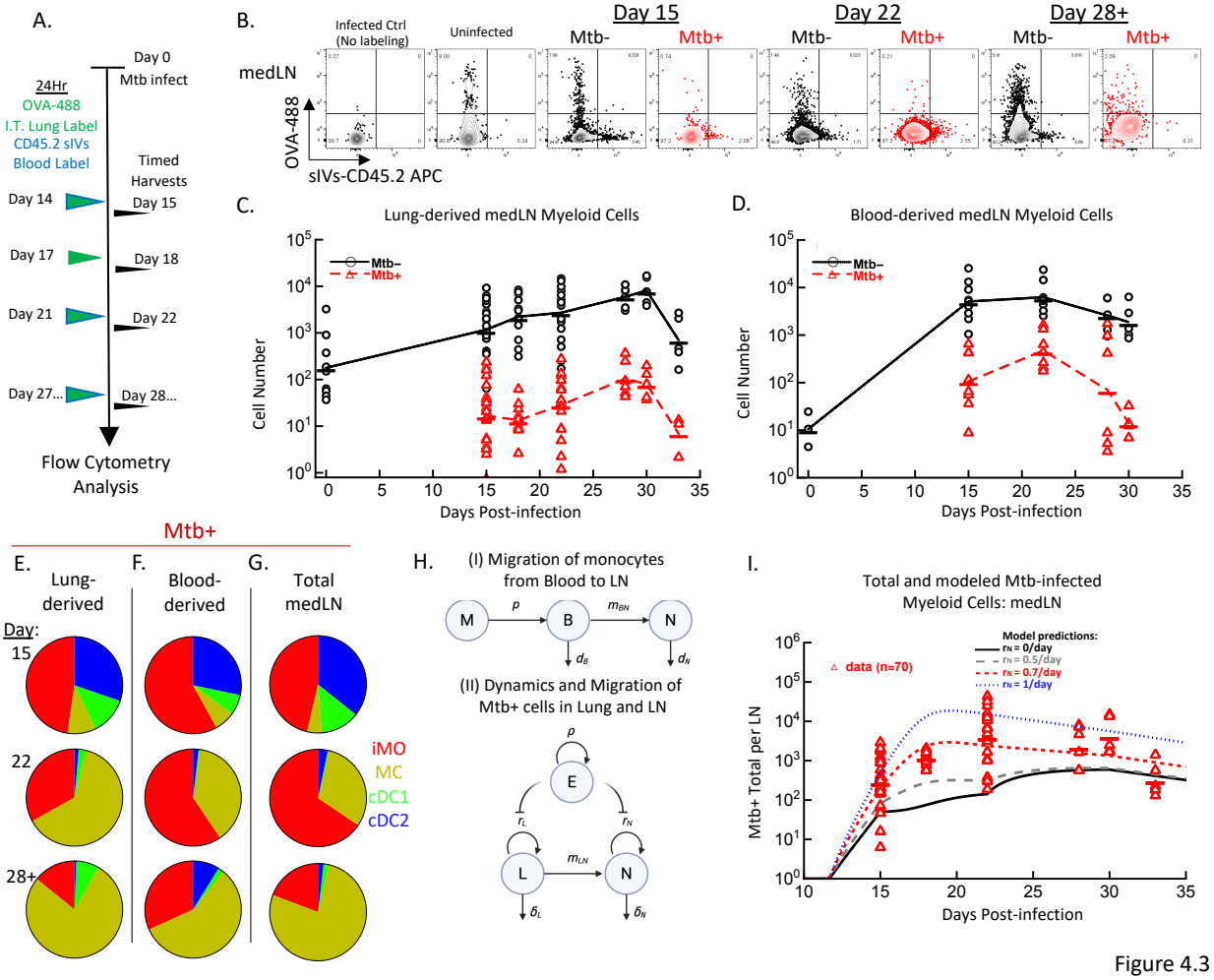
A.
Day 0
Mtb infect
24Hr
OVA-488
I.T. Lung Label
CD45.2 sIVs
Blood Label
Timed
Harvests
Day 14
Day 15
Day 17
Day 18
Day 21
Day 22
Day 27...
Day 28...
Flow Cytometry
Analysis
B.
Infected Ctrl
(No labeling)
Uninfected
Day 15
Day 22
Day 28+
Mtb-
Mtb+
medLN
OVA-488
sIVs-CD45.2 APC
C.
Lung-derived medLN Myeloid Cells
Cell Number
Days Post-infection
D.
Blood-derived medLN Myeloid Cells
Cell Number
Days Post-infection
Mtb+
E.
Lung-
derived
F.
Blood-
derived
G.
Total
medLN
Day:
15
22
28+
iMO
MC
cDC1
cDC2
H.
(I) Migration of monocytes
from Blood to LN
M
B
N
(II) Dynamics and Migration of
Mtb+ cells in Lung and LN
E
L
N
I.
Total and modeled Mtb-infected
Myeloid Cells: medLN
data (n=70)
Model predictions:
Mtb+ Total per LN
Days Post-infection

Figure 4.3

Figure 4.3: Tracking myeloid cell dynamics to the medLN from the lung and blood during Mtb infection

(A) Schematic of lung (OVA-488) and blood (CD45.2 APC) IV labeling 24 hours prior to harvest. (B) Concatenated flow plots of lung- or blood-derived Mtb^- (black) and Mtb^+ (red) myeloid cells in the medLN. Plots represent experimental replicates, with data from 5 mice concatenated per timepoint. Concatenated populations include iMO, MC, cDC1, and cDC2 populations. (C-D) Quantification of lung- or blood-derived Mtb^- or Mtb^+ innate cell numbers at timepoints indicated- days 15-28+ (28-33) p.i. (E-G) Pie charts showing the average proportion of each cell type for total, lung-, or blood-derived Mtb-infected cells in medLN. Flow cytometry plots (B) and proportions (E-G) generated using concatenated data from each experiment. (H) Schematics of mathematical models of myeloid cell dynamics in Mtb-infected mice. (H.i) Modeling of blood monocyte migration to medLN, assuming monocytes are generated in the bone marrow (M) at a rate of *p* and migrate from circulation to the medLN at rate m_{BN} (see eqns. (1)-(8)), with consideration for cell death/migration in blood (d_B) and medLN (d_N). (H.ii) Modeling of Mtb^+ myeloid cells replication at rate r_L and r_N in the lung and medLN, respectively, including migration, immune response (E) at rate ρ, and death rate of Mtb^+ cells in lung (δ_{NL}) and medLN (δ_N). (see eqns. (11)-(15)). (I) Model fits to predict the number of Mtb^+ myeloid cells in the medLN at different assumed rates of Mtb replication in the medLN r_N. Model with r_N = 0/day assumes no Mtb replication in the medLN. Lines are the model predictions (see Table S.3 for model parameters). Data shown represents 3 (D-G) or 6 (B-C, I) independent experiments.

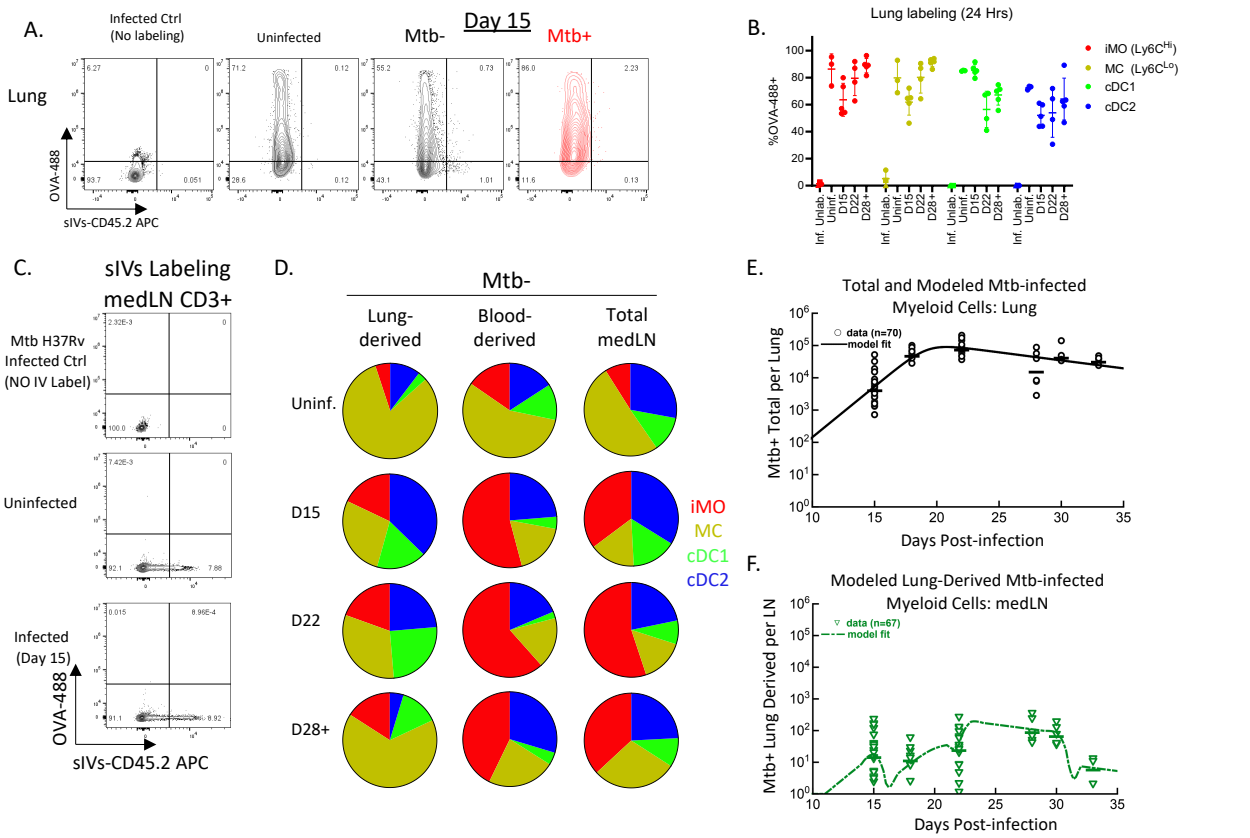

Figure 4.S.3

Figure 4.S.3: Myeloid cell labeling of the lung and blood during Mtb infection

Data related to Fig. 3. (A) Flow plots of lung- or blood-derived Mtb$^-$ (black) and Mtb$^+$ (red) myeloid cells in the lung 24 h after labeling. Data concatenated from 5 mice. Concatenated populations included iMOs, MCs, cDC1s, and cDC2s. (B) Quantification of intratracheal labeling efficiency (OVA-488+) on parenchymal (IV-label$^-$) cells. (C) Gating strategy for identifying lung-derived and blood-derived cells. MedLN T cells (CD3$^+$) are shown. (D) Pie charts show the average proportion of each cell type in total, lung- or blood-derived uninfected Mtb$^-$ cells (calculated using concatenated data from each experiment). (E-F) Predictions of the best fit model of the lung-derived Mtb+ myeloid cells in the lung (E) and for total Mtb+ cells in the medLN (F). Symbols show data from 6 experiments and line denotes the best model prediction (see Table 3 for model parameters).

4.2.5 Narrow Window of Mtb-Specific T Cell Priming in the medLN

Effector $CD4^+$ T cells are critical for Mtb control[165], with ESAT-6–specific $CD4^+$ T cell priming in the medLN initiating ~10 days after aerosol infection and peaking around three weeks, coincident with bacterial dissemination to this organ[30,32,118]. Despite stable medLN bacterial burdens thereafter (Fig. 1A), T cell priming subsequently declines[31], raising the question of how evolving antigen presentation landscapes, shaped by shifts in cDCs and the formation of monocytic aggregates, impact T cell priming and effector differentiation.

To investigate this, we adoptively transferred naïve $CD4^+$ TCR-transgenic cells specific for ESAT-$6_{3–15}$ (C7 line)[117] into congenic recipients at different timepoints post-infection. Tissues were harvested 2 or 3 days later and analyzed by confocal microscopy or flow cytometry, respectively (Fig. 4A). Unlike conventional adoptive transfer experiments that track cumulative T cell responses from the time of infection, this timed transfer strategy captures the capacity of the medLN microenvironment at defined timepoints to support *de novo* T cell priming and differentiation. At day 15 post-infection, C7 cells in the medLN showed robust proliferation, with extensive CTV dye dilution and clonal expansion (Fig. 4B-C). This was accompanied by increased IRF4 and pS6 expression, indicating increased TCR signaling[203,204] (Fig. 4D-E). Day 15 activated C7 cells also underwent efficient Th1 effector differentiation, denoted by increased Tbet and CD25 expression in the divided cells (Fig. 4F-G, S.4A). However, just 1-2 weeks later (days 22 and 28), we observed a marked decline in T cell proliferation, as well as IRF4 and pS6 expression, indicating reduced T cell priming (Fig. 4B-E). We also noted impaired Th1 effector differentiation, reflected by decreased frequencies of $Tbet^+CD25^+$ and $Tbet^+TCF1^-$ highly differentiated effector cells (Fig. 4F-G, S.4A). Diminished PD1 expression was also noted (Fig. S.4B). Activated T cells across examined timepoints did not extensively upregulate KLRG1 or BCL6 expression, indicating lack of differentiation into terminal effector[177,180] or T follicular helper (T_{FH})[205] lineages after three days of priming (Fig. S.4C-E). We observed similar temporal patterns of activation and differentiation in Ag85B-specific CD4 T cells following adoptive transfer of P25 TCR-transgenic cells[150] (Fig. S.4F), as well as in endogenous CD4 and CD8 T cell responses (Fig. S.4G), indicating that these changes were not restricted to a single antigen specificity. Furthermore, similar or even lower levels of C7 T cell activation and differentiation

were observed in the spleen, suggesting a broader failure of lymphoid organs to support effective priming at later stages of infection (Fig. S.4H).

Visualization of medLN T cell responses by microscopy confirmed these temporal changes in T cell activation. At day 15, when innate cells harbored single bacilli, we observed robust C7 cell clustering with strong pS6 and Ki67 staining, indicating potent T cell activation (Fig. 4H-J). In contrast, later timepoints dominated by infected monocytic aggregates showed reduced T cell numbers, diminished clustering, and lower Ki67 expression. While transferred C7 cells were directly juxtaposed to myeloid aggregates containing multiple Mtb bacilli, these T cells lacked pS6 staining, indicating ineffective recognition of antigen despite physical proximity to heavily-infected myeloid cells (Fig. 4H). Similar reductions in T cell priming at late (day 26) timepoints were also observed in the ULD infection model (Fig. 4K-L, Fig S.4I). Impaired T cell activation persisted until at least day 50 (Fig. S.4J), indicating a prolonged shutdown of the tissue's capacity to support T cell priming. Although B cell infiltration occurred around some myeloid aggregates, as previously described[206], most infected aggregates remained in direct contact with both endogenous and C7 T cells, suggesting that physical access was not the dominant limiting factor (Fig. S.4J). These findings demonstrate a narrow temporal window for efficacious T cell priming in the medLN, which occurs just prior to the emergence of Mtb-associated myeloid niches and when the bacterial burden in the LN is relatively low.

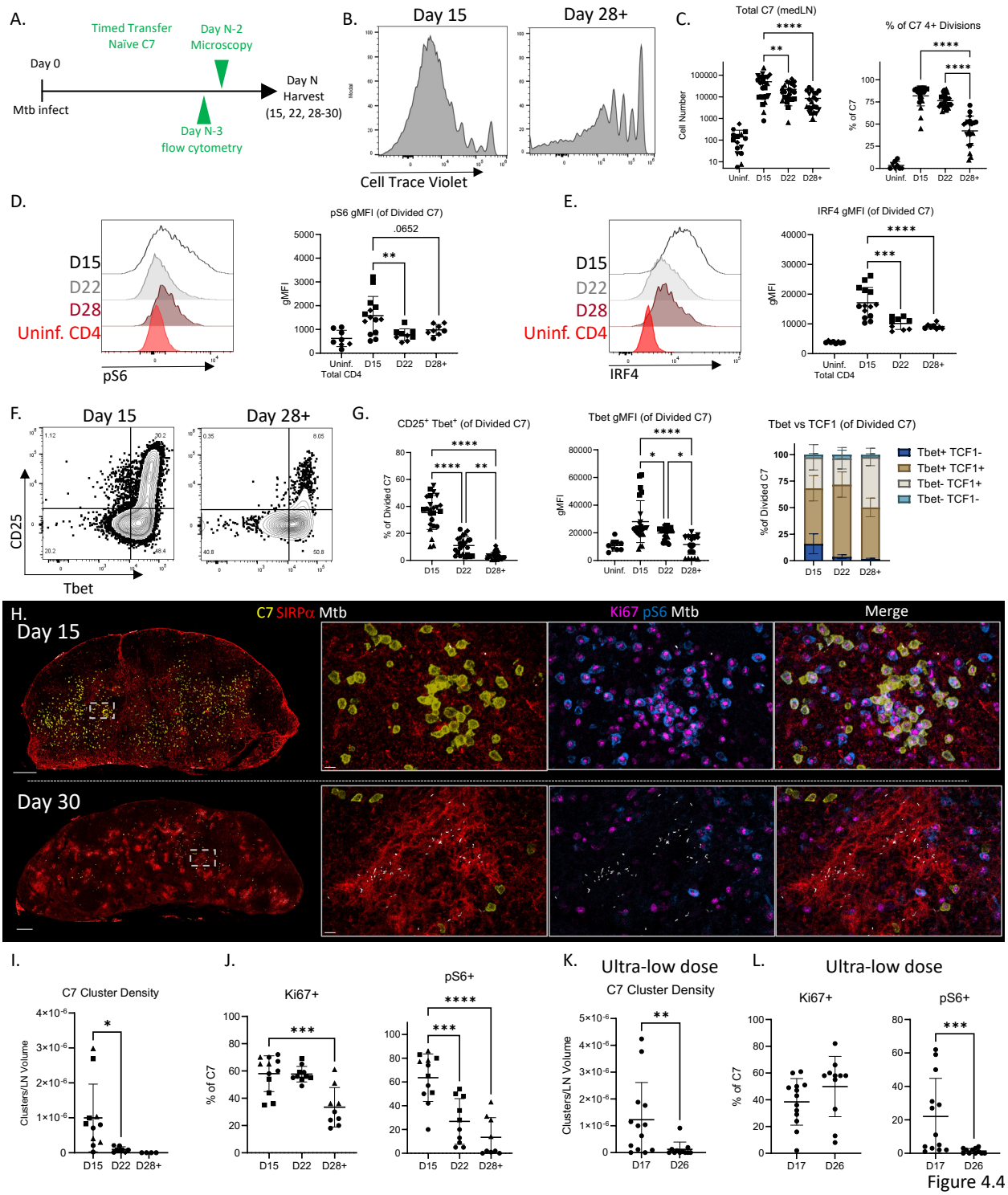
A.
Timed Transfer
Naïve C7
Day N-2
Microscopy
Day 0
Day N
Harvest
(15, 22, 28-30)
Mtb infect
Day N-3
flow cytometry
B.
Day 15
Day 28+
Cell Trace Violet
C.
Total C7 (medLN)
Cell Number
% of C7 4+ Divisions
% of C7
Uninf.
D15
D22
D28+
D.
D15
D22
D28
Uninf. CD4
pS6
pS6 gMFI (of Divided C7)
gMFI
Uninf.
Total CD4
E.
IRF4
IRF4 gMFI (of Divided C7)
F.
Day 15
Day 28+
CD25
Tbet
G.
CD25+ Tbet+ (of Divided C7)
% of Divided C7
Tbet gMFI (of Divided C7)
Tbet vs TCF1 (of Divided C7)
Tbet+ TCF1-
Tbet+ TCF1+
Tbet- TCF1+
Tbet- TCF1-
H.
Day 15
Day 30
C7 SIRPα Mtb
Ki67 pS6 Mtb
Merge
I.
C7 Cluster Density
Clusters/LN Volume
J.
Ki67+
pS6+
% of C7
K.
Ultra-low dose
C7 Cluster Density
D17
D26
L.
Ultra-low dose
Ki67+
pS6+

Figure 4.4

Figure 4.4: Mtb-specific T cell responses are diminished in the medLN as myeloid aggregates and Mtb burden increase

(A) Schematic for timed adoptive transfer experiments. (B-G) Flow cytometry analysis of C7 responses in medLNs at days 15-28+ (28-33) p.i. C7 cells (Live,$DUMP^{-}CD3^{+}CD4^{+}CD8^{-}$ $CD90.1/CD45.1^{+}$), were subgated for divided cells (1+ division) and examined for pS6 gMFI, IRF4 gMFI, $Tbet^{+}$ $CD25^{+}$, Tbet gMFI, as well as analyzed for ratios of Tbet vs TCF1 expressing cells. (H-L) Confocal microscopy of medLNs demonstrating C7 cell activation (Ki67, pS6) with respect to infected myeloid cells, with quantifications of C7 cluster density (I), and Ki67 and pS6 positivity (J). Related analyses for ULD infections (K-L). Scale bar: 200 µM (zoom-out); 10 µM (zoom-in). Data representative of 4-6 (B-C,F-G, N= 21-26 mice; D-E, N=8-14 mice), 3 (H-J, N=9-14 mice) or 1 (K-L, N=31 mice) independent experiments, identified by symbol shape. Statistical results for significance were measured by ordinary one-way ANOVA using multiple comparisons with Tukey's Correction.

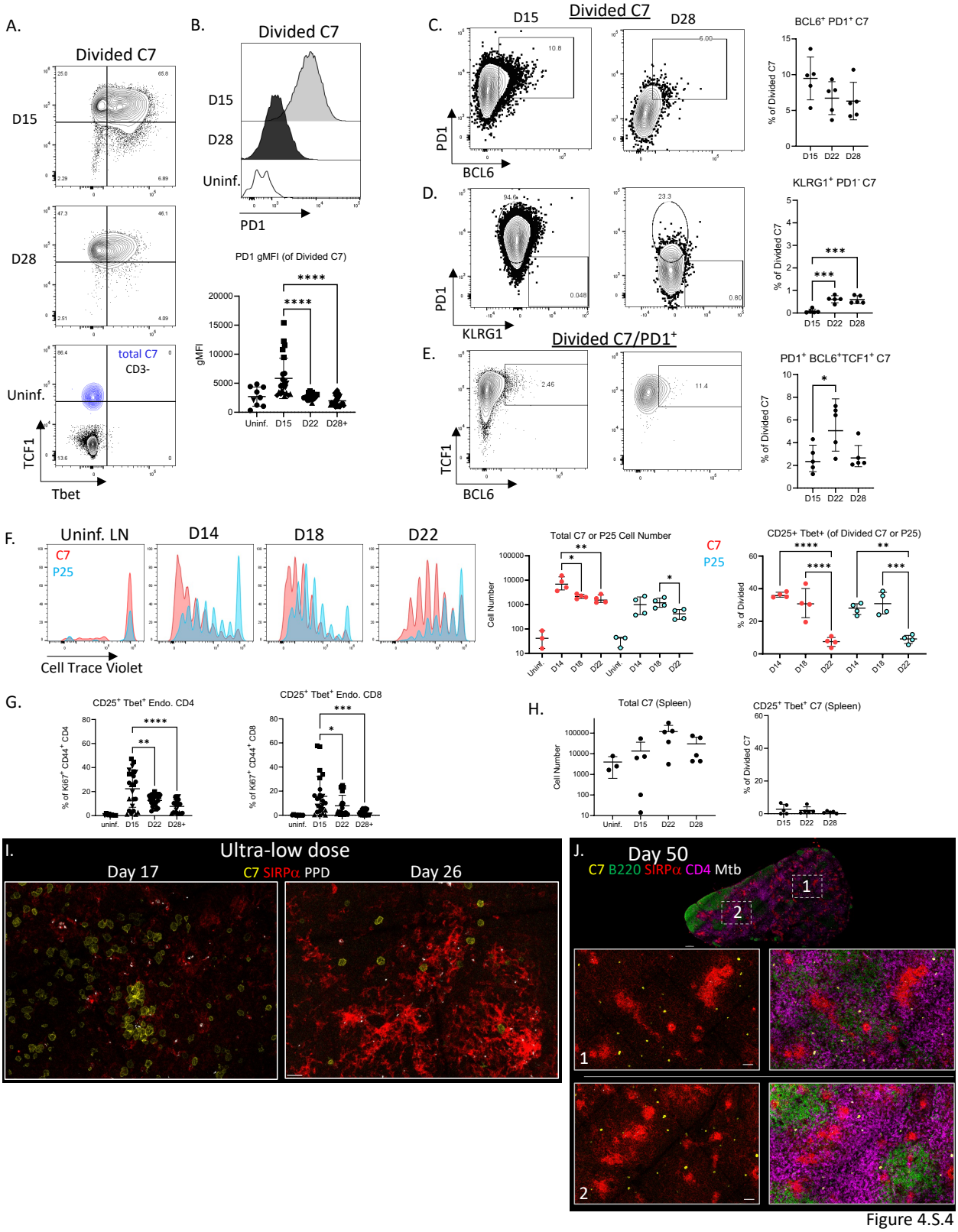
A.
Divided C7
D15
D28
Uninf.
total C7
CD3-
TCF1
Tbet
B.
Divided C7
D15
D28
Uninf.
PD1
PD1 gMFI (of Divided C7)
gMFI
Uninf. D15 D22 D28+
C.
D15
Divided C7
D28
PD1
BCL6
BCL6+ PD1+ C7
% of Divided C7
D15 D22 D28
D.
PD1
KLRG1
KLRG1+ PD1- C7
% of Divided C7
D15 D22 D28
E.
Divided C7/PD1+
TCF1
BCL6
PD1+ BCL6+TCF1+ C7
% of Divided C7
D15 D22 D28
F.
Uninf. LN
D14
D18
D22
C7
P25
Cell Trace Violet
Total C7 or P25 Cell Number
Cell Number
Uninf. D14 D18 D22
CD25+ Tbet+ (of Divided C7 or P25)
% of Divided
G.
CD25+ Tbet+ Endo. CD4
% of Ki67+ CD44+ CD4
uninf. D15 D22 D28+
CD25+ Tbet+ Endo. CD8
% of Ki67+ CD44+ CD8
H.
Total C7 (Spleen)
Cell Number
CD25+ Tbet+ C7 (Spleen)
% of Divided C7
I.
Ultra-low dose
Day 17
C7 SIRPα PPD
Day 26
J.
Day 50
C7 B220 SIRPα CD4 Mtb
1
2

Figure 4.S.4

Figure 4.S.4: T cells have reduced activation over time during Mtb infection

Data related to Fig. 4. C57Bl/6 mice were infected with Mtb H37Rv.mCherry at 50-100 CFU, received timed adoptive transfers of C7 cells (Fig. 4A, where applicable) and harvested at days 15 to 28+ (28-33) p.i. (A) Representative flow plots of total (uninfected) or divided (D15, D28) C7 cells in the medLN as compared to CD3- cells demonstrating differential expression of Tbet vs TCF1. (B) Representative histograms and analysis of PD1 gMFI for total (uninfected) or divided (D15, D28) C7 cells. (C) Flow cytometry analysis of BCL6 and PD1 expression among divided C7 cells. (D-E) Flow cytometry analysis of $KLRG1^+$ (D) or $PD1^+$ $BCL6^+$ $TCF1^+$ (E) phenotype T cells among divided C7 cells. (F) C57Bl/6 mice were transferred with 10^6 naïve $CD45.1^+$ Ag85B-specific P25 and 10^6 naïve $CD90.1^+$ C7 cells 3 days prior to harvest timepoints. Representative cell trace violet cell division plots and quantification of cell numbers and frequency of $Tbet^+$ $CD25^+$ cells are shown. (G) Flow cytometry analysis of endogenous CD4 and CD8 T cells (upstream gate: Live, $DUMP^-$, $CD3^+$, $CD4^+$ or $CD8^+$,$CD44^+$, $Ki67^+$). (H) Flow cytometry analysis of total number and percent $CD25^+$ $Tbet^+$ (of dividided) C7 cells in the spleen. (I-J) Confocal microscopy of ULD day 17 and 26 (I) or standard dose day 50 (J) p.i. medLN with timed adoptive transfers of naïve C7 cells. Scale bar: 200 µM (zoom-out); 20 µM (zoom-in). Data are representative of 2-6 experimental replicates (besides (I) 1 experiment, N=31 mice), indicated by symbol where applicable. Statistical results for significance were measured by ordinary one-way ANOVA using multiple comparisons with Tukey's Correction.

4.2.6 Mtb-Specific CD4⁺ T Cell Priming in the medLN is Driven by the Sequential Activity of cDC1s and Type I Interferon–Induced Inflammatory cDC2s

To identify myeloid cell types supporting C7 T cell responses, we distinguished cDCs from monocyte-derived populations using Zbtb46-GFP reporter mice. At both day 15 and 22 p.i., timepoints associated with T cell priming, most C7 cells were clustered around Mtb⁺Zbtb46-GFP⁺ cells (Fig. 5A-B, S.5A), suggesting that initial activation is driven by infected cDCs. Given the critical role of IL-12 in Th1 polarization[81,207,208], we also examined the distribution of IL-12p40, a key subunit of IL-12p70. This showed that activated C7 T cells frequently clustered around IL-12p40⁺ cells, nearly all of which were Zbtb46-GFP⁺ cDCs (Fig. 5A-B). By day 30, the extent of T cell clustering and presence of IL-12p40⁺ cDCs associated with the clusters had diminished (Fig. 4I, 5A-B), mirroring the loss of T-bet⁺ effector T cells and reduced proliferation seen by flow cytometry.

cDC1s have classically been characterized as potent IL-12 producers during inflammation, prompting us to examine their contribution to T cell priming. Using XCR1-Venus cDC1 reporter mice[148], we visualized cDC1 distribution relative to activated T cells in medLNs following infection. Consistent with our flow cytometry, migration tracing, and scRNA-seq findings, we observed individual cDC1s (Venus⁺) harboring single bacilli (Fig. 5C), supporting their role in direct bacterial transport from infected lungs (Fig. 3E). Many of these infected cDC1s expressed IL-12p40 and co-localized with clusters of activated C7 cells. However, we also noted multiple Venus⁻SIRPα⁺ cells expressing IL-12p40 in association with T cell clusters, suggesting that additional myeloid populations contribute to IL-12 production and T cell priming (Fig. 5C-D).

To directly assess the role of cDC1s in T cell priming, we next performed timed adoptive transfers of C7 cells into BATF3$^{-/-}$ mice[146], which lack normal cDC1 development (Fig. S.5B). Flow cytometry confirmed marked reductions in cDC1s in both lungs and medLNs, while bacterial burden remained equivalent to wild-type controls (Fig. S.5C-D). Analysis of T cell responses revealed that C7 proliferation and expansion were comparable in BATF3$^{-/-}$ and wild-type mice at both day 15 and 22 post-infection (Fig. S.5E-F). Antigen sensing (pS6 expression) and spatial clustering of T cells also appeared intact (Fig. 5E-F), indicating that cDC1s are not required for T cell activation. However, at day 15, the frequency of IL-12p40⁺ cells in proximity to T cell clusters

was reduced in Batf3$^{-/-}$ mice (Fig. 5G), corresponding with partially diminished Th1 effector differentiation marked by significantly lower frequencies of T-bet^{+} TCF1^{-} cells and a trending decrease in T-bet MFI (Fig. 5H-I)[209]. These impairments were not evident at day 22, suggesting a role for cDC1s in Th1 cell differentiation during early infection and compensatory mechanisms at later time points.

We observed strong induction of IFN pathways in medLN cDC2s at day 15 post-infection (Fig. 6A), suggesting conditions conducive to inf-cDC2 development[174-176,210,211]. Indeed, flow cytometric analysis of cDC2s (CD88^{-}CD26^{+}CD11c^{+}MHCII^{+}SIRPα^{+} XCR1^{-}) identified a distinct population co-expressing Ly6C and CD64, phenotypic characteristics of inf-cDC2s (Fig. S.1A), which peaked in abundance in the medLN by 22 days post-infection (Fig. S.6A). A significant proportion of Mtb-infected cDC2s (mCherry^{+}) exhibited this inflammatory phenotype (Fig. S.6B), indicating that Mtb infection promotes inf-cDC2 development. To test whether IFN-I signaling is required for inf-cDC2 generation and subsequent T cell priming, we infected wild-type or Ifnar1$^{-/-}$ mice and performed timed adoptive transfers of naïve C7 cells. In this model, IFN-I deficiency is restricted to host cells, while transferred T cells retain intact IFN-I signaling. In contrast to infected wild-type mice, Ifnar1$^{-/-}$ animals exhibited a marked reduction in total and Mtb-infected inf-cDC2 generation at both day 15 and 22 post-infection (Fig. 6B-D), despite having comparable lung bacterial burdens (Fig. S.6C), numbers of Mtb-infected cells in the medLN (Fig. S.6D), and formation of myeloid aggregates in the T cell zone (Fig. S.6E). A modest reduction in iMO cellularity was observed at day 22 (Fig. S.6F), suggesting a possible role for IFN-I in monocyte recruitment. Assessment of C7 responses revealed that T cell activation and Th1 differentiation were largely intact at day 15, consistent with an early role for cDC1 in T cell priming at this timepoint. However, by day 22, Ifnar1$^{-/-}$ mice exhibited a notable decline in T cell clustering around IL-12^{+} myeloid cells (Fig. 6E-F), and this was accompanied by impaired T cell expansion and reduced Th1 effector differentiation (Fig. 6G-H, S.6G).

Collectively, these findings support a temporal model, where a narrow window of effective Mtb-specific CD4^{+} T cell priming in the medLN is mediated by sequential waves of cDC activity (Fig. S6H). Early after infection, cDC1s are the dominant IL-12-producing subsets driving robust T cell effector differentiation. As infection progresses, IFN-I–driven inf-cDC2s sustain CD4 T cell

responses, contributing to limited effector activation that eventually dissipates. Both processes appear largely independent of expanding Mtb-infected monocytic aggregates which fail to elicit potent T cell responses.

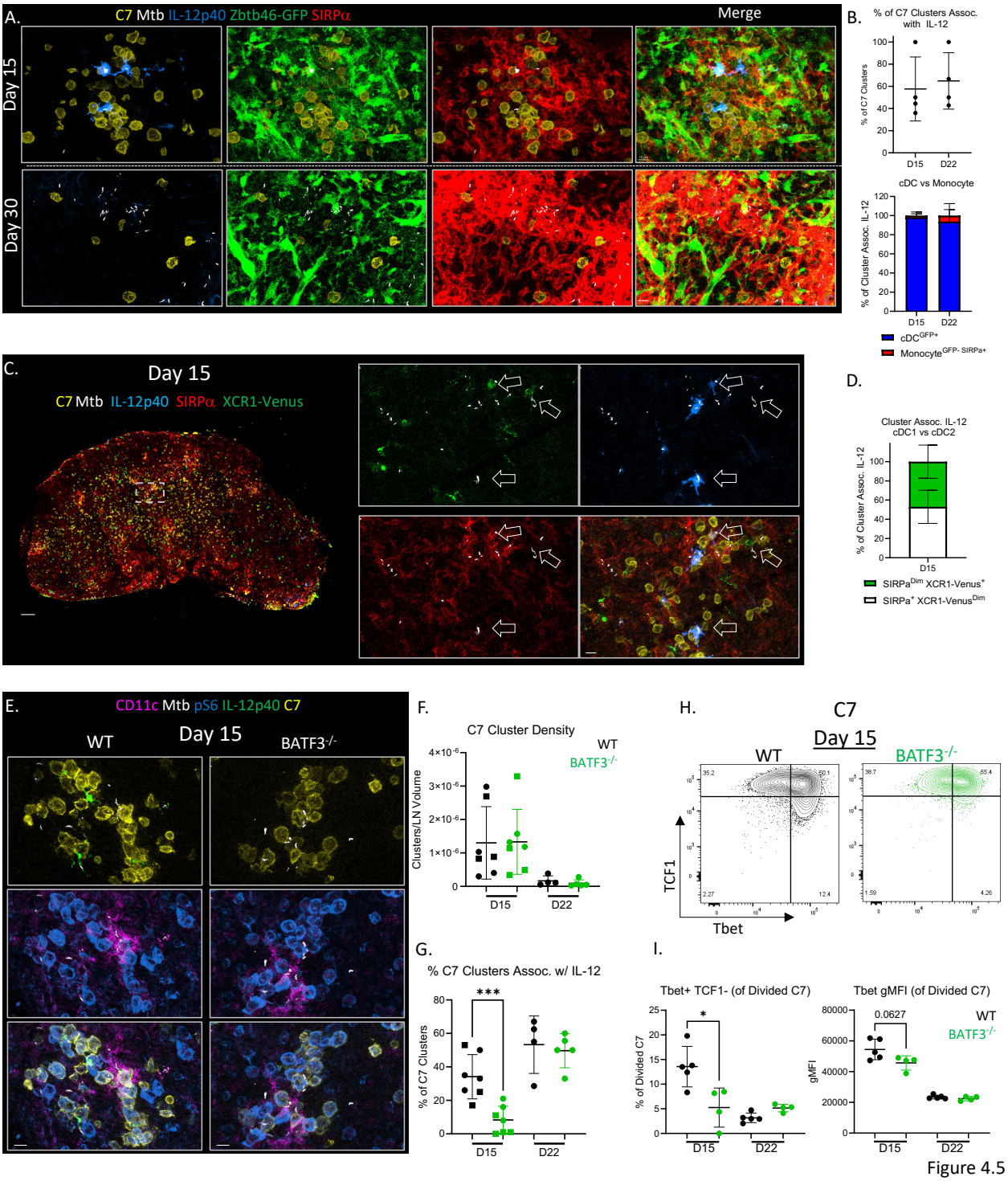
A.
C7 Mtb IL-12p40 Zbtb46-GFP SIRPα
Merge
Day 15
Day 30
B.
% of C7 Clusters Assoc. with IL-12
% of C7 Clusters
D15
D22
cDC vs Monocyte
% of Cluster Assoc. IL-12
cDC^GFP+
Monocyte^GFP- SIRPa+
C.
Day 15
C7 Mtb IL-12p40 SIRPα XCR1-Venus
D.
Cluster Assoc. IL-12 cDC1 vs cDC2
% of Cluster Assoc. IL-12
SIRPa^Dim XCR1-Venus^+
SIRPa^+ XCR1-Venus^Dim
E.
CD11c Mtb pS6 IL-12p40 C7
WT
Day 15
BATF3-/-
F.
C7 Cluster Density
WT
BATF3-/-
Clusters/LN Volume
D15
D22
G.
% C7 Clusters Assoc. w/ IL-12
***
% of C7 Clusters
H.
C7
Day 15
WT
BATF3-/-
TCF1
Tbet
I.
Tbet+ TCF1- (of Divided C7)
*
% of Divided C7
Tbet gMFI (of Divided C7)
0.0627
gMFI

Figure 4.5

Figure 4.5: cDC1 deficiency reduces T cell effector differentiation in the medLN

(A) Representative images of C7 cell clusters surrounding IL-12p40^{+} cells in infected Zbtb46-GFP mice. (B) C7 cluster associated IL-12p40 signal enumerated and phenotyped for cell type by Zbtb46-GFP or SIRPα expression. Scale bar: 10 µM. Data shown is representative of 3 independent experiments. (C) Representative images from XCR-Venus mice showing C7 cell clusters around XCR-Venus^{+} cDC1s (arrows). Scale bar: 100 µM (zoom-out), 10 µM (zoom-in). (D) Quantification of C7 cluster-associated IL-12+ cells, where surfaces were analyzed for XCR1-Venus and SIRPa expression. (E) Representative images of C7 cell clusters associated with IL-12^{+} cells in WT or BATF3$^{-/-}$ mice. Scale bar: 10 µM. (F) C7 cluster density quantification. (G) Fraction of C7 clusters associated with IL-12-positive cells. (H-I) Flow cytometry analysis of Tbet and TCF1 expression in C7 cells in the medLN. Data are representative of 3 independent experiments. Statistical results for significance were measured by student's unpaired T test.

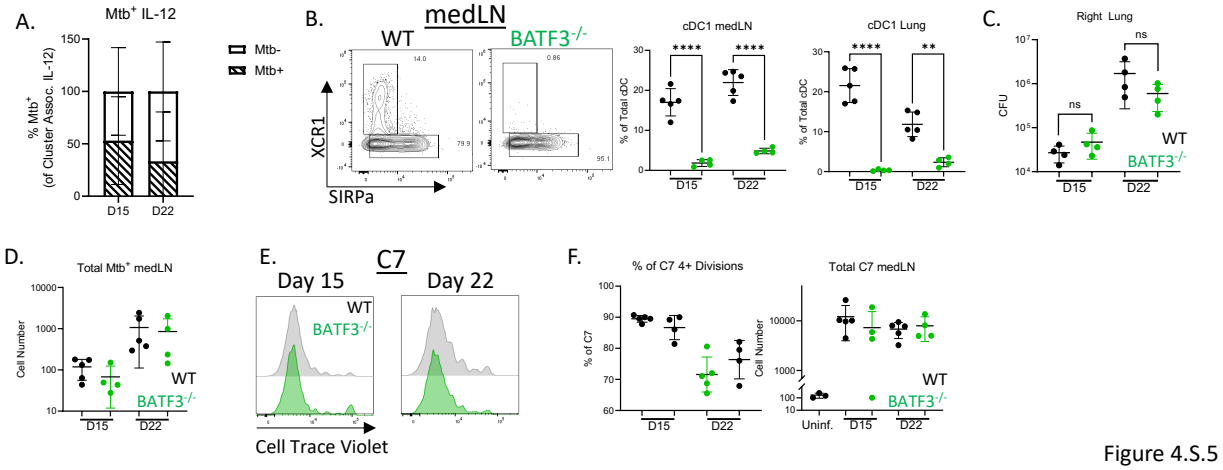

Figure 4.S.5

Figure 4.S.5: Role of cDC1 deficiency in Mtb infection

Data related to Fig. 5. (A) Data related to Fig. 5A-B. Quantification of percent cluster-associated IL-12 signal containing Mtb (mCherry^{+}). (B) Representative flow plots and quantification of cDC1 (CD88^{-}, CD26^{+}, CD11c^{+}, MHCII^{+}, XCR1^{+}) frequency in total cDCs (CD88^{-}, CD26^{+}, CD11c^{+}, MHCII^{+}) in medLNs and lungs of WT and BATF3$^{-/-}$ mice. (C) CFUs from right lungs of WT or BATF3$^{-/-}$ mice at indicated timepoints. (D) Flow cytometry analysis of total Mtb^{+} cell numbers in medLNs. (E-G) Representative flow plots and analysis of C7 cell responses (gating similar to Fig. 4B). (E-G) Total C7 cell numbers and proliferation. (G) Representative histograms of Tbet expression in C7 cells in WT and BATF3$^{-/-}$ mice. Data are representative of 3 independent experiments. Statistical results for significance were measured by student's unpaired T test.

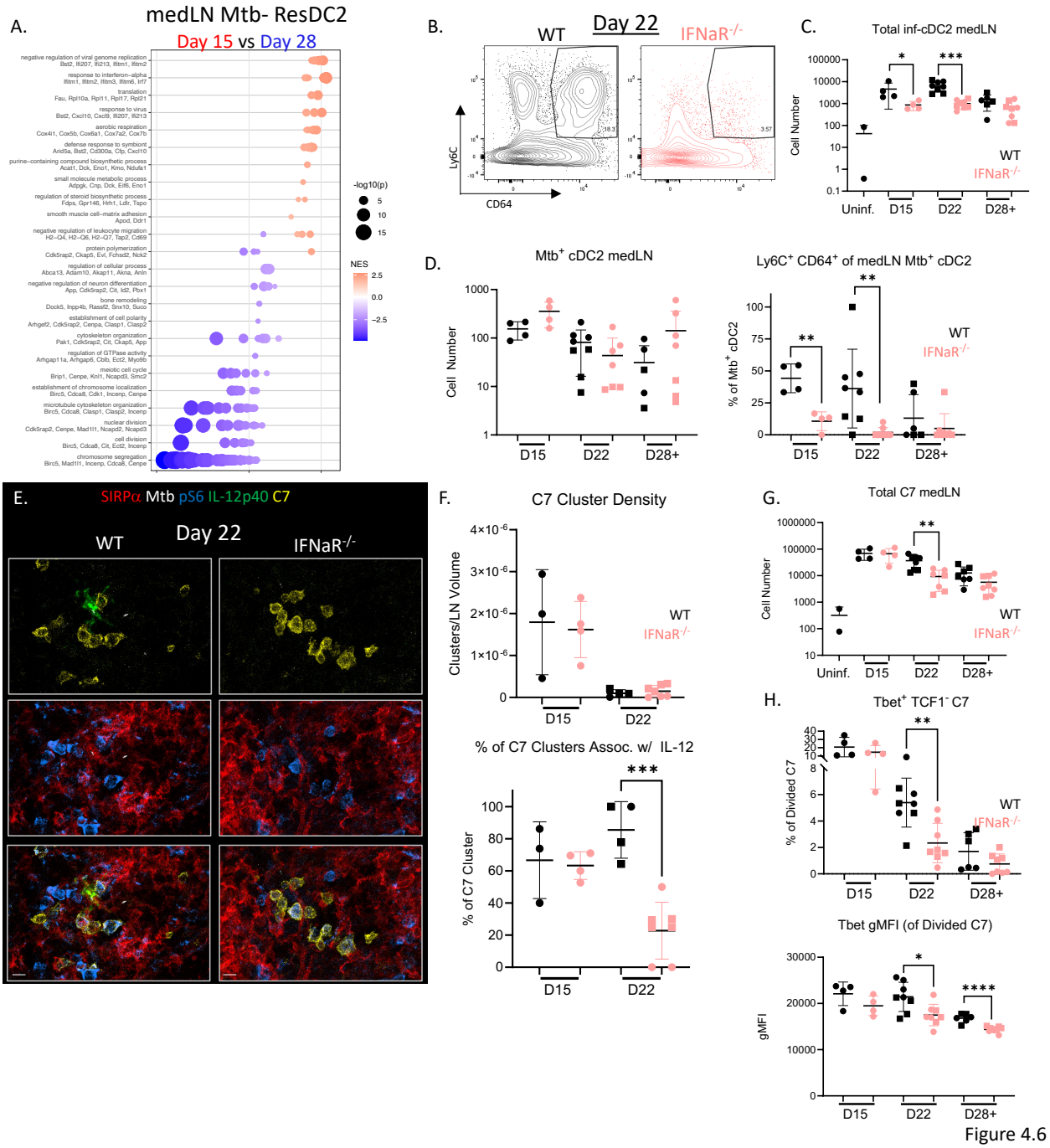
A.
medLN Mtb- ResDC2
Day 15 vs Day 28
-log10(p)
NES
B.
Day 22
WT
IFNaR-/-
Ly6C
CD64
C.
Total inf-cDC2 medLN
Cell Number
Uninf.
D15
D22
D28+
D.
Mtb+ cDC2 medLN
Ly6C+ CD64+ of medLN Mtb+ cDC2
% of Mtb+ cDC2
E.
SIRPα Mtb pS6 IL-12p40 C7
Day 22
F.
C7 Cluster Density
Clusters/LN Volume
% of C7 Clusters Assoc. w/ IL-12
% of C7 Cluster
G.
Total C7 medLN
H.
Tbet+ TCF1- C7
% of Divided C7
Tbet gMFI (of Divided C7)
gMFI

Figure 4.6

Figure 4.6: Inf-cDC2s contribute to T effector cell responses during Mtb infection

(A) Top GO:BP GSEA of D15 vs D28 for bystander (Mtb^-) medLN resDC2s. (B-H) WT or $IFNaR^{-/-}$ mice were infected with Mtb H37Rv.mCherry at 50-100 CFU and harvested at days 15 to 28+ (28-33) p.i. (B-D) Representative flow plots and quantification of total and Mtb^+ inf-cDC2s ($CD88^-CD26^+CD11c^+MHCII^+SIRPa^+CD64^+Ly6C^+$) for infected WT or $IFNaR^{-/-}$ mice. (E-H) Analysis of timed adoptively transferred (Fig. 4A) C7 responses. (E) Representative images of C7 clusters associated with $IL\text{-}12^+$ cells at D22. Scale bar: 10 µM. (F) Quantification of C7 cluster density (top) and percent C7 clusters associated with IL-12-expressing cells (bottom). (G-H) Flow cytometry analysis of C7 responses. Data are representative of 2 independent experiments, indicated by symbol. Statistical results for significance were measured by student's unpaired T test.

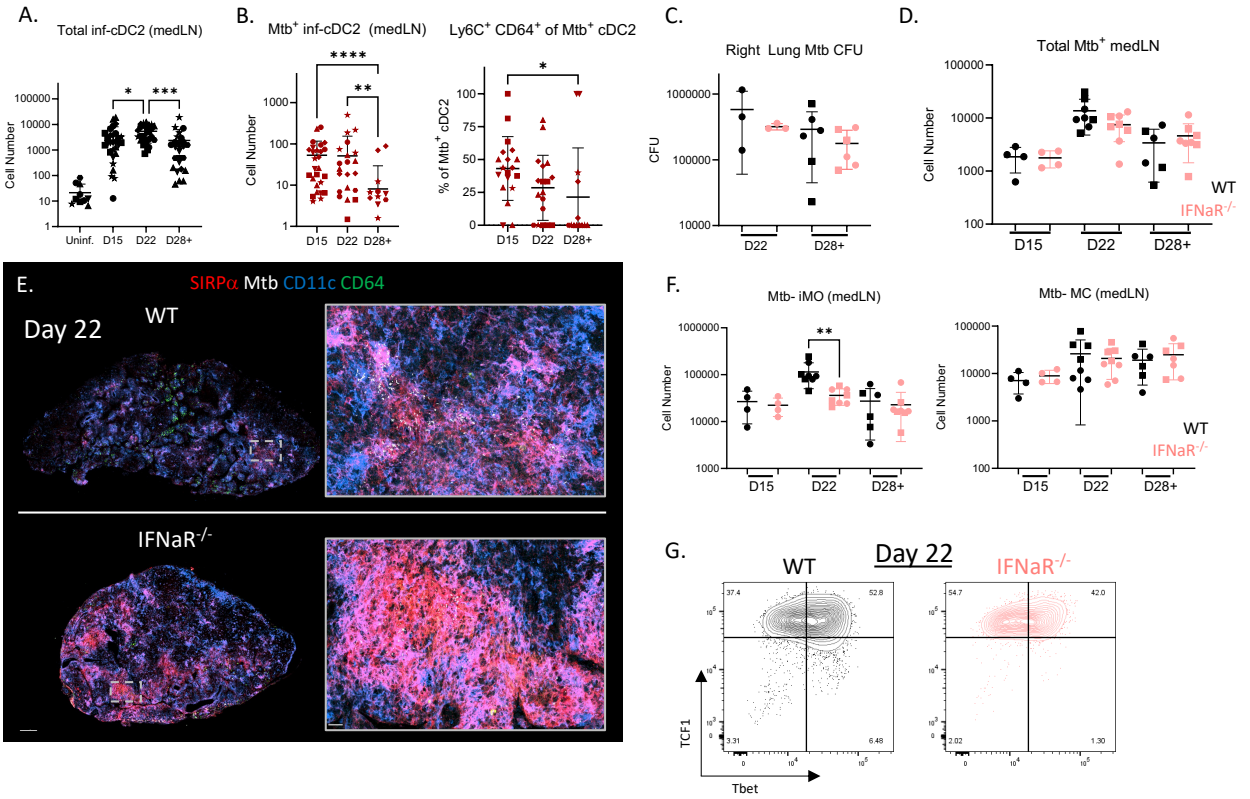
A.
Total inf-cDC2 (medLN)
Cell Number
Uninf.
D15
D22
D28+
B.
Mtb+ inf-cDC2 (medLN)
Ly6C+ CD64+ of Mtb+ cDC2
% of Mtb+ cDC2
C.
Right Lung Mtb CFU
CFU
D.
Total Mtb+ medLN
WT
IFNaR-/-
E.
SIRPα Mtb CD11c CD64
Day 22
WT
IFNaR-/-
F.
Mtb- iMO (medLN)
Mtb- MC (medLN)
G.
WT
Day 22
IFNaR-/-
TCF1
Tbet

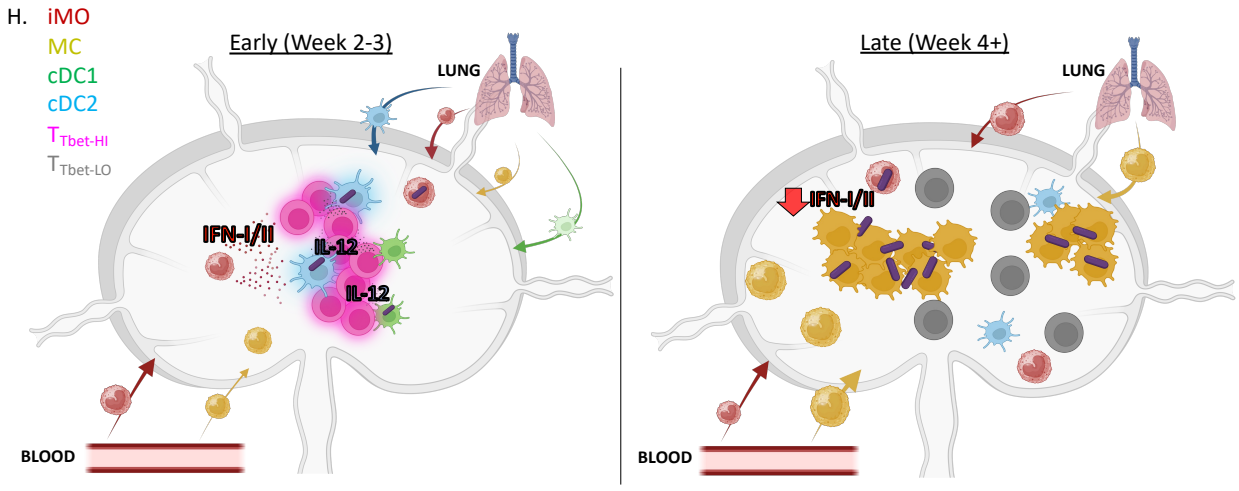
H.
iMO
MC
cDC1
cDC2
TTbet-HI
TTbet-LO
Early (Week 2-3)
LUNG
IFN-I/II
IL-12
IL-12
BLOOD
Late (Week 4+)
LUNG
IFN-I/II
BLOOD

Figure S.6

Figure 4.S.6: Myeloid and T cell phenotypes in IFNaR$^{-/-}$ during Mtb infection

Data related to Fig. 6. WT or IFNaR$^{-/-}$ mice were infected with Mtb H37Rv.mCherry at 50-100 CFU and harvested at days 15 to 28+ (28-33) p.i. (A) Quantification of total and (B) Mtb^{+} inf-cDC2s in WT mice. Data represent 7 experimental replicates, denoted by symbols (N=26-30 mice). (C) CFUs from right lungs of WT or IFNaR$^{-/-}$ mice. (D) Flow cytometry quantification of Mtb^{+} total cell numbers in medLNs. (E) Representative images of D22 medLN. Scale bar: 200 µM (zoom-out), 20 µM (zoom-in). (F) Flow cytometry quantification of total iMOs and MCs in medLNs. (G) Representative flow cytometry plots of Tbet and TCF1 expression by C7 cells at D22 p.i. Data are representative of 2 independent experiments, indicated by symbol where applicable. Statistical results for significance were performed by student's unpaired T test. (H) Graphical model of myeloid and T cell responses in the medLN during early and late Mtb infection.

4.2.7 BCG Immunization Limits Establishment of the Monocytic Niche but not T cell Priming in the medLN

BCG immunization reduces Mtb dissemination from the lung to distal sites[184,185], but whether it impacts initial lung-to-medLN transport or subsequent dissemination remains unclear. In addition, BCG modulates IFN-I/-II responses in myeloid cells[139,212], cytokines that are abundantly sensed in the medLN (Fig. 2, 6), yet its influence on myeloid cell dynamics and *de novo* T cell priming to Mtb-specific antigens in this site has not been defined. To address these questions, we subcutaneously immunized mice with BCG eight weeks prior to aerosol Mtb infection and assessed immune responses in the medLN at various post-infection timepoints.

We found that BCG immunization markedly reduced myeloid aggregate formation in the medLN at both early (day 18) and late (day 28) timepoints (Fig. 7A-B, panel I). This was accompanied by the detection of fewer bacilli per LN section (Fig. 7B, panel II). Notably, the bacillary load per infected myeloid aggregate was lower at day 18 but not day 28 (Fig. 7B, panel III), indicating that once infected, aggregates eventually accumulate similar burdens. We observed similar decreases in myeloid aggregate formation with BCG immunization in the ULD infection model (Fig. 7C-D). Further evaluation by flow cytometry confirmed an approximately 10-fold reduction in the number of Mtb^+ cells in the medLN in BCG immunized mice (Fig. 7E). These reductions were most notable for Mtb^+ iMOs and MCs at days 22 and 28 post-infection, but not at the early day 15 timepoint (Fig. 7F), suggesting intact initial seeding of the tissue but reduced later expansion of the monocytic niche and Mtb burden. Parallel reductions in Mtb^+ iMO and MC populations were also observed in the lung (Fig. S.7A). Phenotypic analysis further revealed that BCG immunization altered medLN iMO and MC maturation, marked by elevated MHC-II early and reduced CD11c at later timepoints (Fig. S.7B-C). In contrast to cells of monocyte origin, Mtb^+ cDCs were present in similar numbers in the medLN regardless of immunization status (Fig. 7F, S.7D), indicating that BCG did not impact cDC trafficking from the lung or their overall cellularity.

We next evaluated *de novo* Mtb-specific T cell priming in the medLN following adoptive transfer of naïve C7 cells (ESAT6 is expressed by Mtb but not BCG[213]). Across timepoints, T cell proliferation and expansion were comparable between non-immunized and BCG-immunized groups (Fig. S.7E), indicating that early cDC-mediated T cell priming was preserved despite

markedly different Mtb burdens. Of note, T cell activation declined by day 28 in both groups, consistent with reduced Mtb-infected cDC2 numbers at this timepoint (Fig. 7F). Interestingly, we observed reduced effector differentiation of C7 cells in BCG-immunized mice at day 22 post-infection (Fig. S.7F), suggesting a change in the quality rather than magnitude of antigen presentation. Consistent with this, total numbers of inf-cDC2s in medLNs were decreased following BCG immunization (Fig. 7G), implicating altered IFN signaling. To assess this, we isolated monocytes from the medLN, lung, and blood of BCG-immunized and control Mtb-infected mice at early (day 15) and later (day 25) timepoints and performed bulk RNA sequencing. Analysis of IFN-I and IFN-II–inducible gene signatures in the medLN[70] revealed that BCG immunization broadly suppressed both pathways at day 15 post infection, with further dampening seen by day 28 in both groups (Fig. 7H, S.7G). In contrast, lung and blood monocyte populations were enriched for IFN signature genes at day 15 with BCG immunization (Fig. S.7G), consistent with the findings that BCG accelerates immunity[140] and concomitant infection alters IFN responses in the lungs[214]. Together, these data align with prior reports that BCG modulates IFN-driven responses in myeloid cells[139,212], and extend them by demonstrating downstream consequences on innate cells and T cell priming within medLNs (Fig. 6).

Collectively, these findings suggested that BCG limits monocytic niche formation in the medLN while reducing Mtb burden. Using intratracheal and intravascular labeling techniques, we found that although BCG immunization increased the number of circulating monocytes in the blood (Fig. S.7H), it resulted in ~2-fold fewer blood-derived monocytes in medLN at 15 or 22+ days post-infection (Fig. S.7H), suggesting reduced recruitment to the tissue. To quantify these effects over time, we developed a mathematical model of monocyte trafficking fitted to these data (eqns. (6)-(8)). The model captured the increase in monocyte migration into the medLN in both groups (Fig. S.7H), also demonstrating a ~2–3-fold reduction in the per capita monocyte entry rate in BCG-immunized mice (Fig. S.7I and Table S.2). Notably, total numbers of blood-derived Mtb-infected cells in the medLN were unchanged (Fig. S.7J), indicating that alterations in circulatory monocytes with BCG do not markedly contribute to reduced bacterial burdens in medLNs. Additionally, the model estimated comparable migration rates of Mtb-infected innate cells from lung to medLN in unimmunized and BCG-immunized mice (with some variability in

unimmunized rates, Fig. S.7K), suggesting that BCG does not alter initial Mtb dissemination to the lymph node. Inferred rates of Mtb replication in the lung and medLN were also comparable between groups (Fig. S.7L and Table S.3). Instead, reduced numbers of Mtb-infected cells in BCG-immunized mice were best explained by earlier immune control of Mtb growth, reflected by a shorter time to half-maximal control (parameter T_E; Fig. S.7M), rather than by altered cell trafficking. This is consistent with earlier Mtb control previously observed in lungs of BCG-immunized mice[140].

Finally, to directly test how BCG impacts Mtb dissemination to the medLN and other organs, we employed the ULD model using aerosol exposure of mice to a pool of 50 barcoded strains of H37Rv with the goal of an effective dose of ~1 CFU/mouse[14,184]. This allowed tracking dissemination of individual bar-coded Mtb strains across tissues. As expected, BCG immunization significantly reduced Mtb burden in both lungs and medLNs at day 28 (Fig. 7I). As previously shown[184], BCG significantly restricted the dissemination of barcoded Mtb strains from the initially infected lung to the contralateral lung. In contrast, the barcodes found in the medLN largely matched those in the primary lung, regardless of immunization status (Fig. 7J, S.7N). These findings suggest that BCG-mediated immunity does not prevent initial Mtb access to the medLN, but instead curtails local replication and myeloid niche formation, while effectively limiting establishment of infection at distal sites.

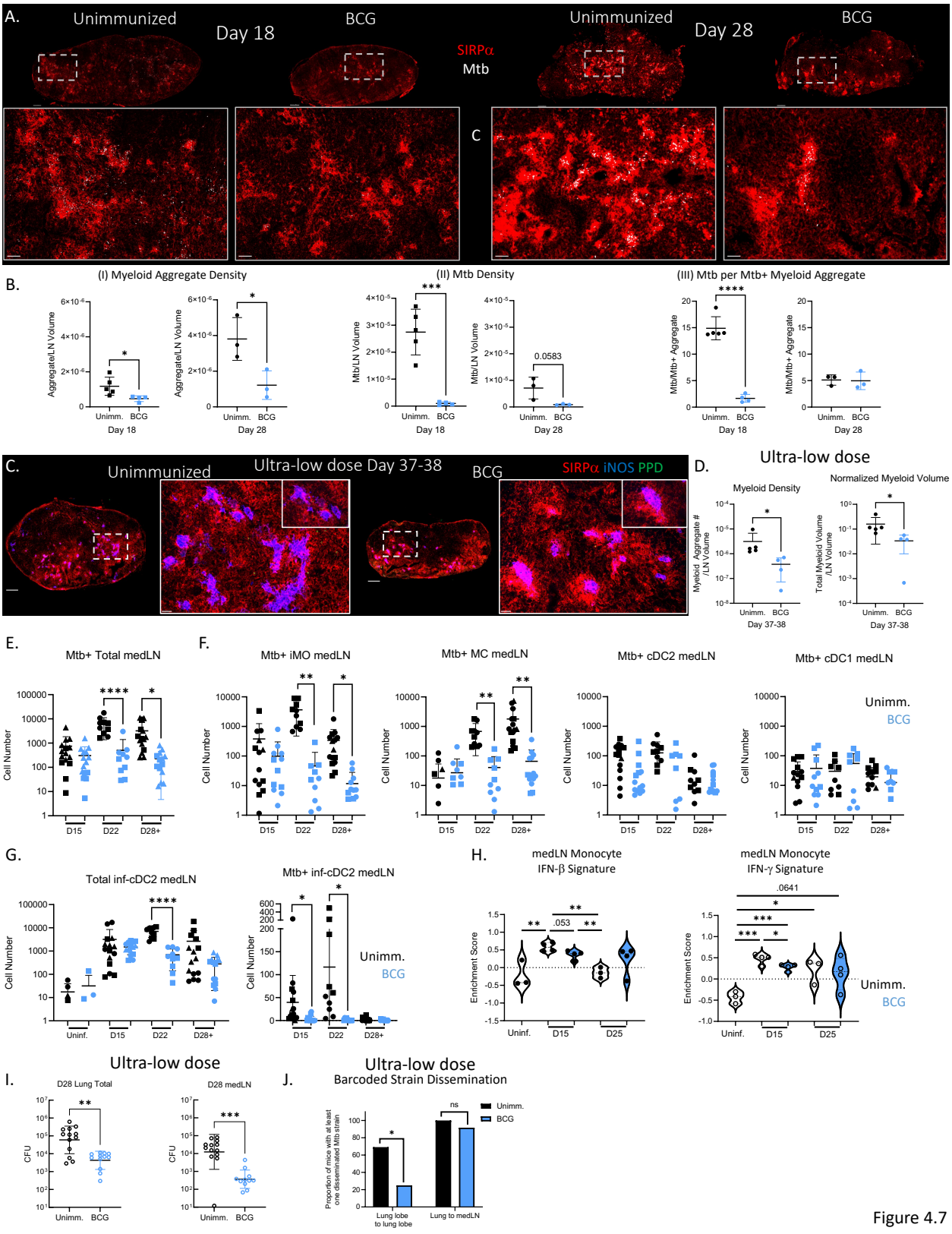
A.
Unimmunized
Day 18
BCG
Unimmunized
Day 28
BCG
SIRPα
Mtb
C
B.
(I) Myeloid Aggregate Density
(II) Mtb Density
(III) Mtb per Mtb+ Myeloid Aggregate
Aggregate/LN Volume
Mtb/LN Volume
Mtb/Mtb+ Aggregate
Unimm.
BCG
Day 18
Day 28
0.0583
C.
Unimmunized
Ultra-low dose Day 37-38
BCG
SIRPα iNOS PPD
D.
Ultra-low dose
Myeloid Density
Normalized Myeloid Volume
Myeloid Aggregate # /LN Volume
Total Myeloid Volume /LN Volume
Day 37-38
E.
Mtb+ Total medLN
F.
Mtb+ iMO medLN
Mtb+ MC medLN
Mtb+ cDC2 medLN
Mtb+ cDC1 medLN
Cell Number
D15
D22
D28+
Unimm.
BCG
G.
Total inf-cDC2 medLN
Mtb+ inf-cDC2 medLN
Uninf.
H.
medLN Monocyte IFN-β Signature
medLN Monocyte IFN-γ Signature
Enrichment Score
D25
I.
Ultra-low dose
D28 Lung Total
D28 medLN
CFU
J.
Ultra-low dose
Barcoded Strain Dissemination
Proportion of mice with at least one disseminated Mtb strain
Lung lobe to lung lobe
Lung to medLN
ns

Figure 4.7

Figure 4.7: BCG immunization improves Mtb control in the medLN

(A-B) Confocal microscopy of D18 and D28 medLNs from unimmunized or BCG immunized mice. (A) Representative images demonstrating myeloid aggregates and Mtb. N = 4-5/group. Scale bars: 200 uM (zoom-out), 10 uM (zoom-in). (B) Quantifications of myeloid aggregate density (I), total Mtb density per imaged LN section volume (II), and total number of Mtb bacilli per Mtb-infected myeloid aggregate (III). (C-D) Confocal microscopy of D37-38 ULD medLNs with myeloid aggregate quantifications, significance measured by Mann-Whitney Test. (E-F) Flow cytometry quantification of total number of Mtb^{+} innate cells in medLN (N=10-15 mice/group). Gating shown in Fig. S1A. (G) Flow cytometry quantification of total and Mtb-infected inf-cDC2s. (H) Bulk RNAseq IFN-b and IFN-g signature score analysis of bystander medLN MOs ($CD3^{-}B220^{-}Ly6G^{-}CD26^{-}CD88^{+}SIRP\alpha^{+}Mtb^{-}$). (I-J) ULD Mtb infection with BCG immunization (I) Quantification of D28 lung and medLN CFUs. (J) Mtb barcode sequencing results from lung and medLN. Statistical significance measured by Fischer's Exact Test. Data represent 2-3 independent experiments. Statistical results for significance were measured by student's unpaired T test, unless otherwise noted.

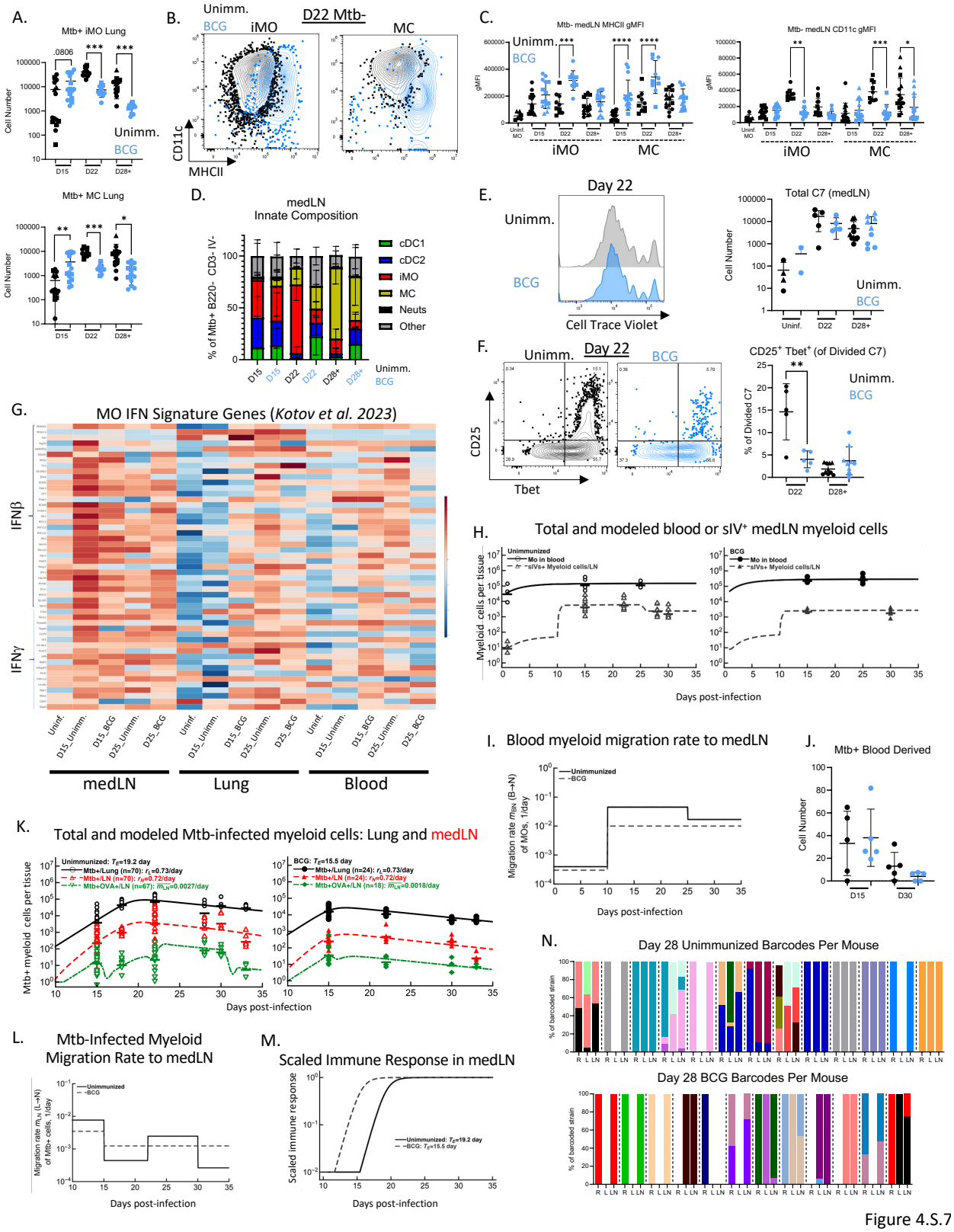
A.
Mtb+ iMO Lung
Mtb+ MC Lung
Cell Number
Unimm.
BCG
D15
D22
D28+
B.
Unimm.
BCG
iMO
MC
D22 Mtb-
CD11c
MHCII
C.
Mtb- medLN MHCII gMFI
Mtb- medLN CD11c gMFI
gMFI
D.
medLN
Innate Composition
% of Mtb+ B220- CD3- IV-
cDC1
cDC2
iMO
MC
Neuts
Other
E.
Day 22
Cell Trace Violet
Total C7 (medLN)
F.
CD25
Tbet
CD25+ Tbet+ (of Divided C7)
% of Divided C7
G.
MO IFN Signature Genes (Kotov et al. 2023)
IFNβ
IFNγ
medLN
Lung
Blood
H.
Total and modeled blood or siV+ medLN myeloid cells
Myeloid cells per tissue
Days post-infection
I.
Blood myeloid migration rate to medLN
Migration rate
J.
Mtb+ Blood Derived
K.
Total and modeled Mtb-infected myeloid cells: Lung and medLN
Mtb+ myeloid cells per tissue
L.
Mtb-Infected Myeloid
Migration Rate to medLN
M.
Scaled Immune Response in medLN
Scaled immune response
N.
Day 28 Unimmunized Barcodes Per Mouse
Day 28 BCG Barcodes Per Mouse
% of barcoded strain

Figure 4.S.7

Figure 4.S.7: Myeloid cell alterations and responses to BCG immunization

Data related to Fig.7. (A-D) Flow cytometry analysis of innate cells from medLN and lungs. Gating shown in Fig. S1A. (A) Quantification of Mtb^+ lung iMO and MCs by cell number. (B) Representative plots and (C) quantification of CD11c and MHCII expression in iMOs and MCs. (D) Quantification of Mtb-infected innate cells in medLNs as a proportion of Mtb^+ $B220^-$ $CD3^-$ IV^- cells. (E-F) Representative plots of C7 cell responses in D22 unimmunized or BCG immunized mice, with associated quantifications of total cell numbers and frequencies of divided C7 cells coexpressing Tbet and CD25 (F). (G) Gene expression heatmap for IFN-b and IFN-g signature genes identified in Kotov et. al., *Cell*, 2023. Gene expression normalized across all samples; n=3 or 4 biological replicates per condition. (H-I) Data on blood monocyte counts and blood-derived ($sIVs^+$) medLN myeloid cells were used to generate a best fit mathematical model (eqns. (1)–(2) and eqns. (3)–(4)) in unvaccinated (H-left) or BCG-vaccinated (H-right) mice (SSR = 5.78). Observed data denoted with symbols and lines show model predictions. In the model we let the rate of monocyte migration to change at day 10 and 25 post Mtb-infection (eqn. (8) and I) and the monocyte production rate p to depend on time since infection as $p = p_{min} + (p_{max} - p_{min})(1 - e^{-\alpha t})$ (see Table 3 for the parameter values). (J-L) Trafficking analysis of lung-derived and total Mtb-infected myeloid cells. Mathematical models (eqns. (11)– (12) and eqns. (13)–(14)) were fit to experimental data on the number of Mtb-infected myeloid cells in the lung, medLNs, and infected lung-to-medLN migrating cells ($Mtb^+OVA\text{-}488^+$) in unvaccinated (J-left) or BCG-vaccinated (J-right) mice (overall SSR = 64.54). Predictions of the (K) change in the rate of migration of Mtb+ cells from the lung to medLNs with time, and (L) scaled magnitude of the immune response which controls Mtb replication ($E_s(t) = (hE(t))^n/(1 + (hE(t))^n$) and with a detection limit of 0.01 for $E_s(t)$). The predicted time of immune response $T_E = -ln(h)/\rho$. (M) Related to Fig. 7G-H; Individual barcoded strains (denoted by color) shown per mouse for right lung (R), left lung (L), and medLN (LN), and quantified as a percentage of the total barcoded strains per tissue. Data by flow cytometry represent 2-3 independent experiments, indicated by symbol shape where applicable (N=10-15 mice/group). Statistical results for significance were measured by student's unpaired T test unless otherwise noted in legend.

4.3 Discussion

Lymph nodes are critical sites for the initiation of adaptive immune responses, yet paradoxically, Mtb and related mycobacteria effectively infect and persist within lymphatic tissues across multiple species[45,46]. In primary TB, which usually occurs in children, this can manifest as significant lymphadenopathy and pathology[215]. While earlier mouse studies have defined the onset of T cell responses in the medLN[30,118], it has remained unclear how the same organ can support both robust early T cell priming and long-term bacterial persistence. Here, we leveraged tools uniquely available in murine models to construct a spatiotemporal map of innate and adaptive responses to Mtb within the medLN. We show that infection in this organ proceeds through distinct stages. An initial phase is characterized by the induction of Mtb-specific $CD4^+$ T effector responses driven by sequential waves of cDC activity. However, this phase is brief and coincides with the emergence of a monocytic niche that appears functionally immuno-evasive and that supports local bacterial replication and persistence. Notably, this niche forms within the T cell zone of medLNs despite strong induction of inflammatory cytokine signaling and microbicidal pathways in the infected cells. Together, our findings indicate that Mtb is highly adapted for persistence within the LN microenvironment and underscore the limits of Th1-mediated immunity in achieving sterilizing protection.

Through blood and lung tracing experiments, paired with mathematical modeling of bacterial growth kinetics, we demonstrate that both cDCs and monocytes initially transport Mtb from the lung to the medLN, contrasting to a prior study which attributed Mtb transport exclusively to monocytes[24]. We believe this discrepancy reflects reliance on depletion of CCR2 expressing cells in the earlier study, as during inflammation[24] and as we now show during Mtb infection, CCR2 is expressed by multiple immune cell types, including cDCs. Over time, however, migration of Mtb-infected cDCs declines, whereas monocyte trafficking persists, mirroring shifts in innate cell composition in the lung. In addition to lung-to-medLN trafficking, we observe a burst of iMO entry from the blood, which likely represents the dominant source of cells driving the monocytic niche formation in the infected medLNs. Following this initial transport and the establishment of the monocytic niche, Mtb burden in the medLN appears to be driven largely by local bacterial replication rather than continued trafficking from the lung.

We further uncover a previously unappreciated division of labor among cDC subsets in CD4 T cell priming. cDC1s, canonically associated with IL-12 production and T cell differentiation[146,182], are indeed critical early mediators of Th1 responses. However, as infection progresses, elevated IFN-I signaling induces differentiation of inf-cDC2s, which become the dominant IL-12-producing population sustaining T cell responses, albeit less robustly than cDC1s. This observation reveals a nuanced role for IFN-I in Mtb infection biology across different organs. While IFN-I promotes pathogenic outcomes in lung[70,216-220], it appears partially beneficial in LNs by supporting continued effector T cell differentiation. Over time, however, we find a decline in the migration of Mtb-infected cDCs from lungs, accompanied by reduced bystander IFN-I sensing in the medLNs, which together likely contribute to the waning of T cell priming.

Although T cell activation in the medLN was markedly diminished at later timepoints, it was not completely abolished. CD4 T cells activated at later phases exhibited reduced effector function but retained elevated expression of the transcription factor TCF1. This phenotype is consistent with the generation of stem-like memory cells that sustain long-term immune surveillance and provide partial control over persistent infection[165,169,177,180,181,198,221]. These findings suggest that the heterogeneity of T cell responses in the lung during Mtb infection, including the balance of effector and memory populations, is in part temporally imprinted in the medLN, dictated by the specific myeloid subsets and inflammatory cues present at the time of priming. Of note, although the timed adoptive transfer approach employed here does not recapitulate the physiological kinetics of T cell priming, our observations do mirror endogenous polyclonal responses and are congruent with prior studies[30,31].

Our cross-organ single-cell RNA-sequencing atlas enabled us to assess tissue-specific myeloid cell alterations during early Mtb infection. In the medLN, infected cells shifted from early involvement of cDCs and iMOs to a predominance of MCs by day 28, whereas in the lung, infection transitioned from alveolar macrophages and neutrophils to iMO2-dominated populations with fewer MCs. Irrespective of these differences, infected cells in both tissues demonstrated induction of multiple inflammatory transcriptional programs, including TNF and IFN-I/-II signaling, indicating robust immune sensing. Despite this, Mtb continued to persist,

underscoring the pathogen's resilience and its ability to survive in the face of classical inflammatory and antimicrobial responses.

In addition to shared inflammatory programs, Mtb-infected cells in the lung vs. medLN exhibited complex and dynamic metabolic profiles. At day 15 post-infection, infected monocytic cells in the medLN were preferentially enriched for oxidative phosphorylation, whereas by day 28, glycolytic programs predominated in infected cells in both tissues. This transition from oxidative phosphorylation to glycolysis, termed the "Warburg" effect, enables rapid energy production and can support immune activation and inflammatory responses against pathogens[222]. Infected cells also upregulated hypoxia-associated pathways and acquired tissue-regenerative transcriptional features resembling non-canonical, pro-inflammatory wound-healing macrophages that promote cellular survival during bacterial infection[223]. Together, these features suggest that Mtb persistence in the medLN and lung reflects a combination of resilience to inflammatory and hypoxic stress, metabolic adaptation, and engagement of tissue-repair programs within infected myeloid cells.

A key factor likely contributing to Mtb persistence is the inability of Mtb-specific T cells to efficiently recognize infected monocyte-derived aggregates. Despite close physical proximity of transferred Mtb-specific and endogenous T cells to infected aggregates, we observed little evidence of T cell activation, as assessed by pS6 and IRF4 expression. Similar defects in T cell sensing of infected macrophages have been reported in liver and lung granulomas[204,224], suggesting that T cell inability to detect infected myeloid niches is a conserved feature across organs. Although Mtb can suppress antigen presentation through multiple mechanisms[225-229], this alone is unlikely to explain the near-complete lack of T cell activation as infected cells within aggregates expressed high levels of surface MHC-II. Furthermore, other infected cell types, such as Mtb-infected cDCs at earlier timepoints readily engaged with and activated CD4 T cells, indicating that infection does not universally abolish antigen presentation. Instead, infected aggregates may establish a locally immunosuppressive environment analogous to tumors[20,26,230]. Consistent with this, infected MCs in the medLN upregulated hypoxia-associated programs and inhibitory molecules such as PD-L1 and iNOS, whose expression has been shown to suppress TCR signaling[89-92,197].

A non-mutually exclusive explanation is that infected cDCs and MCs display different Mtb peptide antigens on their MHC molecules. Immunodominant T cell responses primed by cDCs are typically directed against secreted proteins and antigens expressed by actively replicating bacteria[231,232]. By contrast, induction of iNOS and hypoxia modules in infected MCs likely promotes bacterial stress-response related antigens via activation of the DosR regulon[93-96]. Supporting this idea, a lung monocyte-derived population sharing transcriptional features with medLN MCs was previously shown to harbor DosR-expressing Mtb[190]. Infected monocytic aggregates may therefore preferentially present distinct antigens that cannot be recognized by T cells primed by cDC-presented immunodominant antigens[233,234], resulting in ineffective immune surveillance. While recent studies have begun to define Mtb antigens presented by infected cells in vitro[235,236], further work is needed to determine which antigens are actively presented on MHC under stressed in vivo conditions, such as by the infected MCs.

Notably, we observed upregulation of both classical and non-classical MHC-I molecules on infected MCs, including H2-T23 (Qa-1), the murine homolog of HLA-E. Qa-1/HLA-E–restricted Mtb peptides are largely conserved across species, and loss of Qa-1 in mice increases susceptibility to Mtb infection[237-239]. Moreover, bispecific antibodies targeting Mtb–peptide HLA-E complexes can activate T cells and reduce bacterial burdens in Mtb-infected cells in vitro[240]. These findings suggest that vaccines targeting stress-induced and non-classical MHC-restricted Mtb epitopes may provide new strategies to overcome immunological blindness and enhance protective T cell responses against persistent Mtb reservoirs.

The only currently approved TB vaccination strategy, BCG, has limited efficacy against pulmonary disease but restricts Mtb disseminated disease in humans[185] and mice[184]. Our studies show that BCG immunization limits the establishment of the monocytic niche in the medLN and markedly reduces local Mtb burden without altered bacterial trafficking from the lung. Notably, these changes do not substantially affect *de novo* T cell priming, even in the setting of reduced bacterial load. These findings highlight the stark distinction between the mechanisms that initiate T cell responses (antigen-presentation by migratory cDCs was unchanged by BCG) and those that promote Mtb replication and persistence (infected monocytes that do not activate T cells). Consistent with prior work[184], we further demonstrate

that BCG immunization prevents the establishment of infection in the contralateral lung following ULD infection. Future studies are needed to determine whether this protection reflects reduced hematogenous dissemination or more rapid clearance of Mtb following seeding of distal tissue sites.

Limitations of the study

An important limitation of our study is that it was performed using a relatively restricted set of host and pathogen strains, which do not encompass the full spectrum of TB pathogenesis. In certain cases of human and NHP infection, lung-draining LNs can develop large necrotic granulomas that appear distinct from those in our studies. Future studies, including human post-mortem analyses and investigations of diverse animal models, will be needed to dissect the pathways that lead to these divergent outcomes and to more fully characterize the range of LN pathology in TB.

Altogether, however, our work reveals dynamic remodeling of medLNs during Mtb infection, which rapidly transitions from a site of potent adaptive immune induction to an immunologically inert reservoir of infection. By integrating a comprehensive myeloid single-cell atlas with spatial imaging and functional analyses of T cell priming, we provide a framework for dissecting host–pathogen interactions across tissues and time. These findings have direct implications for TB vaccine design, particularly strategies aimed at selectively targeting lymphoid tissues and monocytic niches that sustain bacterial persistence. Ultimately, our findings underscore that effective TB control strategies must account for the dynamic, tissue-specific nature of host-pathogen interactions rather than focusing exclusively on pulmonary infection or early stages associated with rapid bacterial replication.

Section 5. Shifting the host immune system: the protective capacity of cDCs and TH1 skewed Mtb-specific T cells in the medLN during Mtb infection

The work described in this section was used to improve our understanding of specific immune cell phenotypes to the major findings of our published manuscript but has not been peer reviewed and published. I would like to acknowledge Jessica Huang, Jiajie Le, and Molly Kanagy for their help and scientific support in generating the data shown in this section.

5.1 Revisiting the role of cDCs in the medLN during Mtb infection

5.1.1 Introduction

cDCs are central mediators of adaptive immune responses, responsible for antigen transport and presentation to T cells within draining lymphoid tissues. As discussed previously, TH1-skewed $CD4^+$ effector T cells are critical for protective immunity against Mtb. In Section 4, we identified cDC1 and inf-cDC2 subsets as potent producers of IL-12 and key drivers of TH1-skewed Mtb-specific $CD4^+$ T cell responses in the medLN during weeks 2–3 post-infection.

These findings build upon prior work establishing cDCs as essential for early Mtb-specific T cell priming in the medLN[24] and as capable of acquiring and presenting exogenous Mtb antigens. However, interpretation of cDC function in Mtb infection has been complicated by limitations of experimental models, including reliance on ex vivo culture systems[72], insufficient specificity of surface markers used to distinguish cDCs from monocyte-derived populations[71,72], and the use of transgenic depletion systems with unintended off-target effects, particularly depletion of monocytes in ostensibly cDC-specific models[1]. These limitations motivated the development of more refined in vivo approaches to isolate cDC contributions.

To address these concerns, we utilized the gating strategy described in Figure 4.S1A and generated Zbtb46-DTR bone marrow chimeras. In this system, host mice were sublethally irradiated and reconstituted with Zbtb46-DTR bone marrow, enabling selective depletion of Zbtb46-expressing cDCs from the hematopoietic compartment following diphtheria toxin (DT) administration. This approach allows for more specific interrogation of cDC function with minimal disruption to monocyte populations. In parallel, we employed a cDC2 depletion model ($CD11c^{cre}$ $IRF4^{fl/fl}$) to assess the contribution of matured migratory cDC2s during Mtb infection.

5.1.2 Results: cDCs are critical for T cell responses in the medLN during Mtb infection

To validate and extend prior findings by Samstein et al.[24], who used whole-body Zbtb46-DTR depletion, we employed Zbtb46-DTR bone marrow chimeras to interrogate cDC function during Mtb infection in a more controlled system. Mice were infected with 50–100 CFU of Mtb H37Rv.mCherry and received timed adoptive transfers of 10^6 naïve C7 cells three days prior to harvest for flow cytometric analysis.

Analysis at day 18 post-infection revealed partial, but not complete, depletion of cDCs following DT administration (20 ng/kg body weight) at days 15 and 17 (Fig. 5.1A). In addition to significant reductions in cDCs (Fig. 5.1A), we observed a significant reduction in C7 T cell numbers within the medLN (Fig. 5.1B), consistent with previous reports[24]. Notably, this effect was restricted to response magnitude, as effector phenotypes defined by T-bet, CD25, and TCF1 expression were preserved (Fig. 5.1B). Similar trends were observed among endogenous $CD4^+$ and $CD8^+$ T cells, where antigen-experienced ($pS6^+$ $IRF4^+$) populations were reduced in number without alterations in effector differentiation (Fig. 5.1C–D). These data indicate that cDCs are required for optimal T cell expansion and activation in the medLN but not for TH1 effector polarization, suggesting compensatory cytokine and costimulatory signals from other myeloid populations.

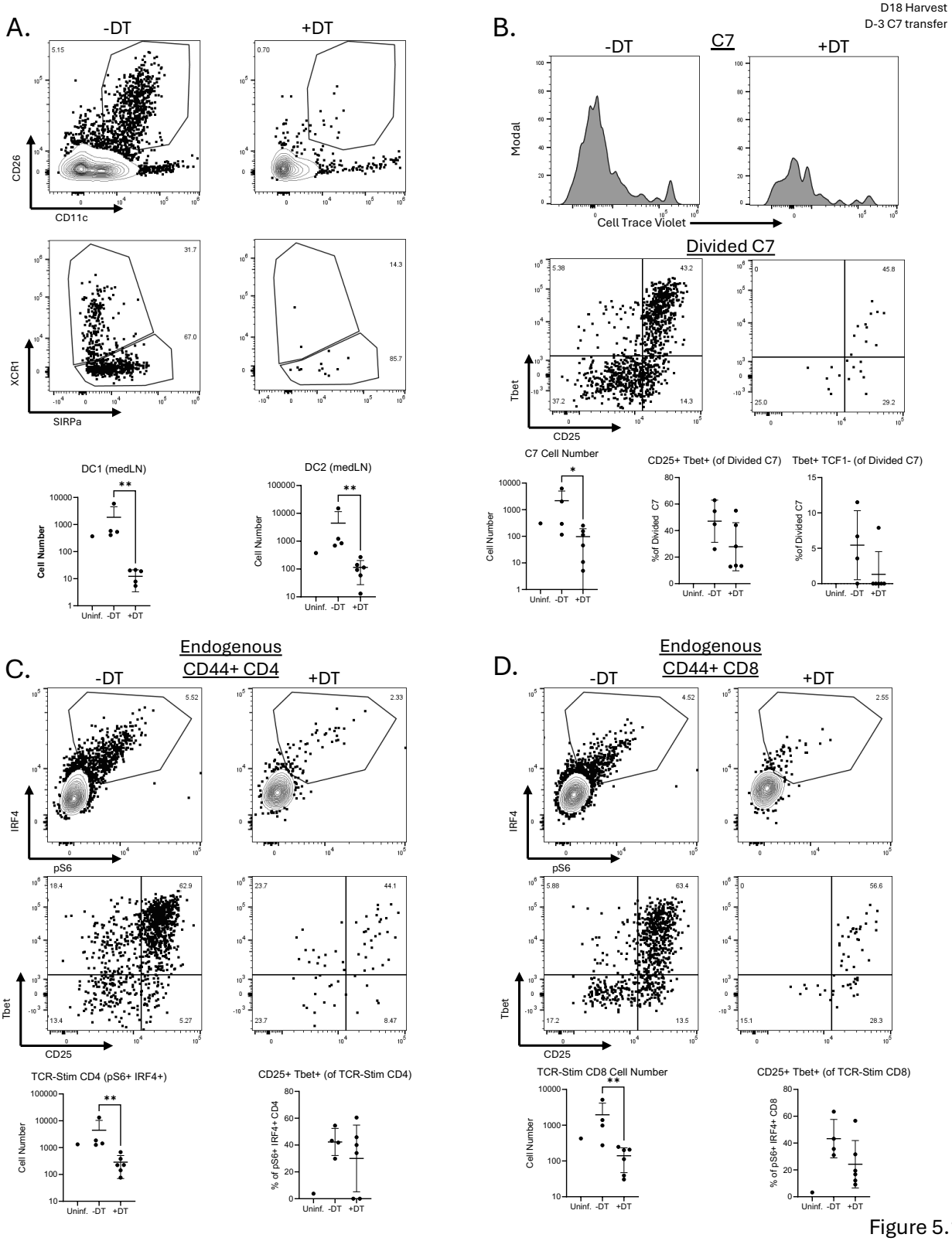
A.
-DT
+DT
CD26
CD11c
XCR1
SIRPa
DC1 (medLN)
DC2 (medLN)
Cell Number
Uninf. -DT +DT
B.
D18 Harvest
D-3 C7 transfer
C7
-DT
+DT
Modal
Cell Trace Violet
Divided C7
Tbet
CD25
C7 Cell Number
CD25+ Tbet+ (of Divided C7)
Tbet+ TCF1- (of Divided C7)
%of Divided C7
C.
Endogenous
CD44+ CD4
IRF4
pS6
TCR-Stim CD4 (pS6+ IRF4+)
CD25+ Tbet+ (of TCR-Stim CD4)
% of pS6+ IRF4+ CD4
D.
Endogenous
CD44+ CD8
TCR-Stim CD8 Cell Number
CD25+ Tbet+ (of TCR-Stim CD8)
% of pS6+ IRF4+ CD8

Figure 5.1

Figure 5.1: Zbtb46-DTR chimeras have reduced T cell response magnitude. Zbtb46-DTR chimeras were generated and DT was administered at 20 ng/kg body weight at days 15 and 17 post-Mtb infection (H37Rv.mCherry 50-100 CFU). Mice were harvested for flow cytometry analysis at day 18 post-infection. (A) Flow cytometry analysis of cDCs (as gated in Fig. 4.S.1A), identifying cDC1 and cDC2s in medLNs of DT treated and untreated chimeras. (B) timed adoptive transfer C7 responses (similar to Fig. 4.4A) by cell number, and effector (Tbet+ CD25+ or TCF1-) phenotypes. (C-D) endogenous CD4 and CD8 T cell responses, gating on TCR-stimulated (IRF4+ pS6+) and further on T effector phenotypes (Tbet+ CD25+). Data shown is representative of 2 independent experiments.

5.1.3 Results: Migratory cDC2s are not required for C7 responses in the medLN

In Section 4, we identified cDCs as underappreciated carriers of Mtb from the lung to the medLN during early infection and demonstrated key roles for cDC1 and inf-cDC2 subsets in antigen presentation and IL-12 production. Transcriptomic analyses further suggested migratory phenotypes among Mtb-infected cDCs at day 15. To directly assess the contribution of migratory cDC2s, we utilized $CD11c^{cre}$ $IRF4^{fl/fl}$ mice, in which DC2 maturation and LN migration are impaired [241,242]. Consistent with prior studies[242], these mice exhibited a selective reduction in the migratory cDC2s compartment (by percent of total migratory cDCs) within medLNs at days 15 and 21 post-infection (Fig. 5.2A), without affecting Mtb burdens in the lung or medLN (Fig. 5.2B–C) by total Mtb^+ cell numbers.

Looking at Mtb-specific T cell activation in the medLN by flow cytometry, we saw equal cellularity, terminal divisions by cell trace violet dilution, and effector response generation at both day 15 and day 21 (Fig. 5.2D-F). We also looked at these phenotypes spatially at day 15, where we saw equal C7 density (Fig. 5.2H-I), as well as antigen sensing and proliferation by pS6 (Fig. 5.2J) and Ki67 (Fig. 5.2K), respectively. These findings suggest that migratory cDC2s are not requisite for effective Mtb-specific $CD4^+$ T cell priming in the medLN and support the existence of compensatory antigen-presenting populations within this tissue.

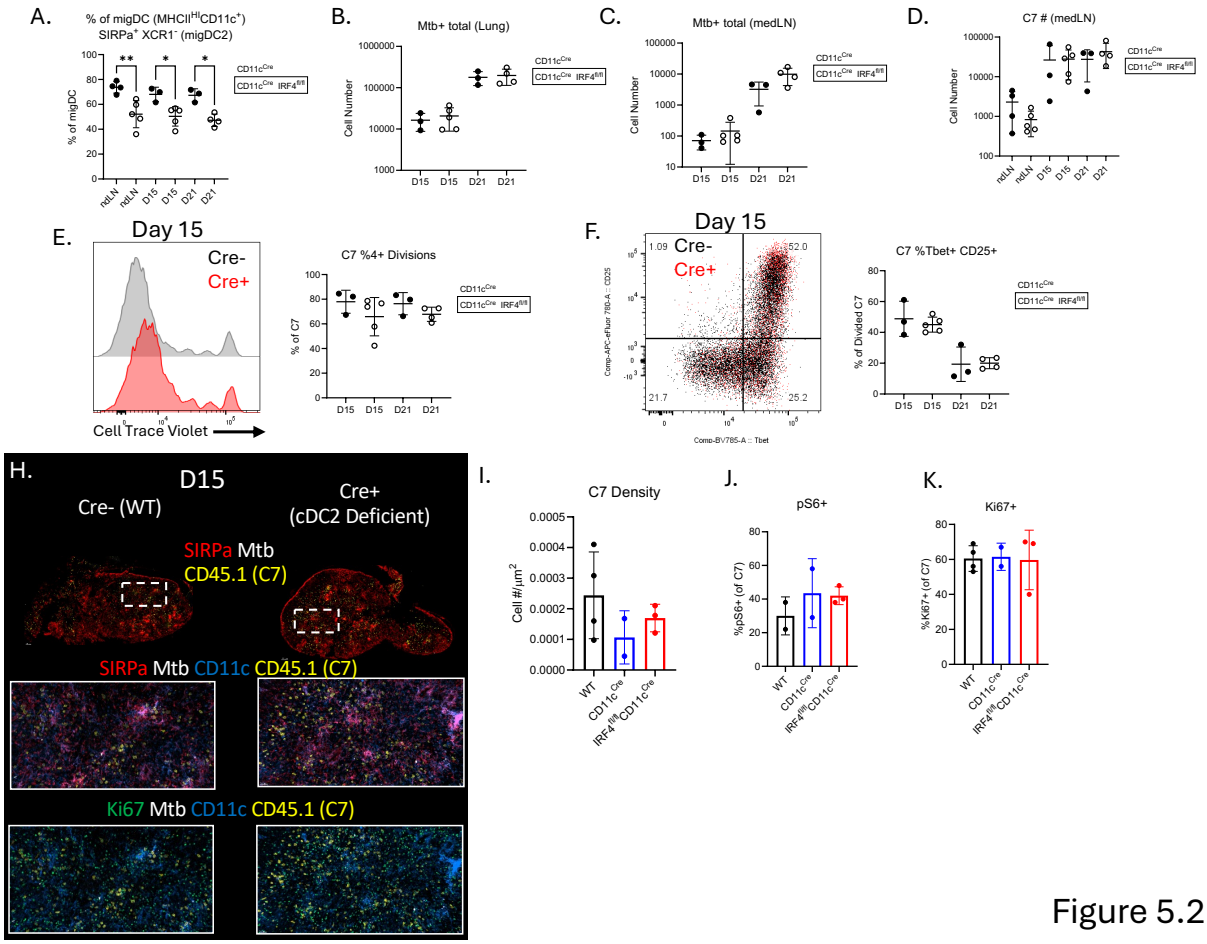

Figure 5.2

Figure 5.2: CD11c^{cre} IRF4$^{fl/fl}$ mice do not have altered Mtb trafficking or T cell responses. CD11c^{cre} IRF4$^{fl/fl}$ mice were infected with Mtb (H37Rv.mCherry 50-100 CFU). (A-F) Mice were harvested for flow cytometry analysis at days 15 or 21 post-infection. (A) Flow cytometry analysis of cDCs (as gated in Fig. 4.S.1A), with further gating on migratory (MHCIIHI CD11c+) identifying mig-cDC2s in medLNs. (B-C) Mtb cell numbers in the lung and medLN by flow cytometry. (D-F) C7 responses by cell number, and effector (Tbet+ CD25+) phenotypes. Day 15 examples shown. (H-K) Confocal microscopy analysis of day 15 medLNs, with identification of myeloid (SIRPa, CD11c) cells, Mtb, and C7 T cells (CD45.1, Ki67), and associated quantifications (I-K). Data shown is representative of 2 independent experiments.

5.2 Immunological blindness during Mtb infection

5.2.1 Introduction

A key finding emerging from our work in Section 4 is the failure of Mtb-specific $CD4^+$ T cells to effectively recognize and engage Mtb-infected myeloid cells within the medLN. The immune-evasive strategies employed by Mtb are well documented and include intracellular suppression of antigen presentation pathways, expression of immunodominant decoy antigens, and metabolic reprogramming toward dormancy. Consistent with these mechanisms, many contemporary vaccine strategies generate robust TH1 responses against immunodominant antigens such as Ag85 and ESAT-6 yet fail to confer sterilizing protection[79], suggesting that immune activation alone is insufficient for bacterial clearance.

Given the persistence of Mtb within monocytic niches, we hypothesized that overwhelming TH1-skewed antigen-specific T cell responses might attenuate these niches. To test this, we generated ex vivo TH1-polarized Mtb-specific (C7) $CD4^+$ T cells and adoptively transferred 10^7 cells five days prior to tissue harvest, assessing immune responses in the medLN and lung at early (day 18) and late (day 30) time points. Antigen-irrelevant, similarly polarized OT-II $CD4^+$ T cells served as controls to account for bystander effects.

5.2.2 Results: TH1 skewed effector T cells are unable to attenuate Mtb burden in the medLN

To determine whether enhancing adaptive immunity could overcome medLN bacterial persistence, we adoptively transferred large numbers (10^7) of ex vivo TH1-polarized C7 or antigen-irrelevant OTII $CD4^+$ T cells into infected hosts 5 days prior to harvest timepoints as previously described[204] (Fig. 5.3A). While these cells trafficked efficiently to the medLN and expressed high levels of T-bet, they failed to significantly reduce Mtb burden within the medLN at either day 18 or day 30 post-infection (Fig. 5.3B-C).

Confocal microscopy revealed that C7 transfer reduced expansion of monocytic aggregates over time compared to OT-II controls (Fig. 5.3D–E), yet normalized Mtb density within the medLN remained unchanged (Fig. 5.3D–E). In contrast, lung CFU measurements demonstrated significant bacterial reduction following C7 transfer, consistent with prior studies[4] (Fig. 5.3F).

These results highlight a striking tissue-specific divergence in immune efficacy, identifying the medLN as uniquely resistant to otherwise protective TH1-mediated immunity.

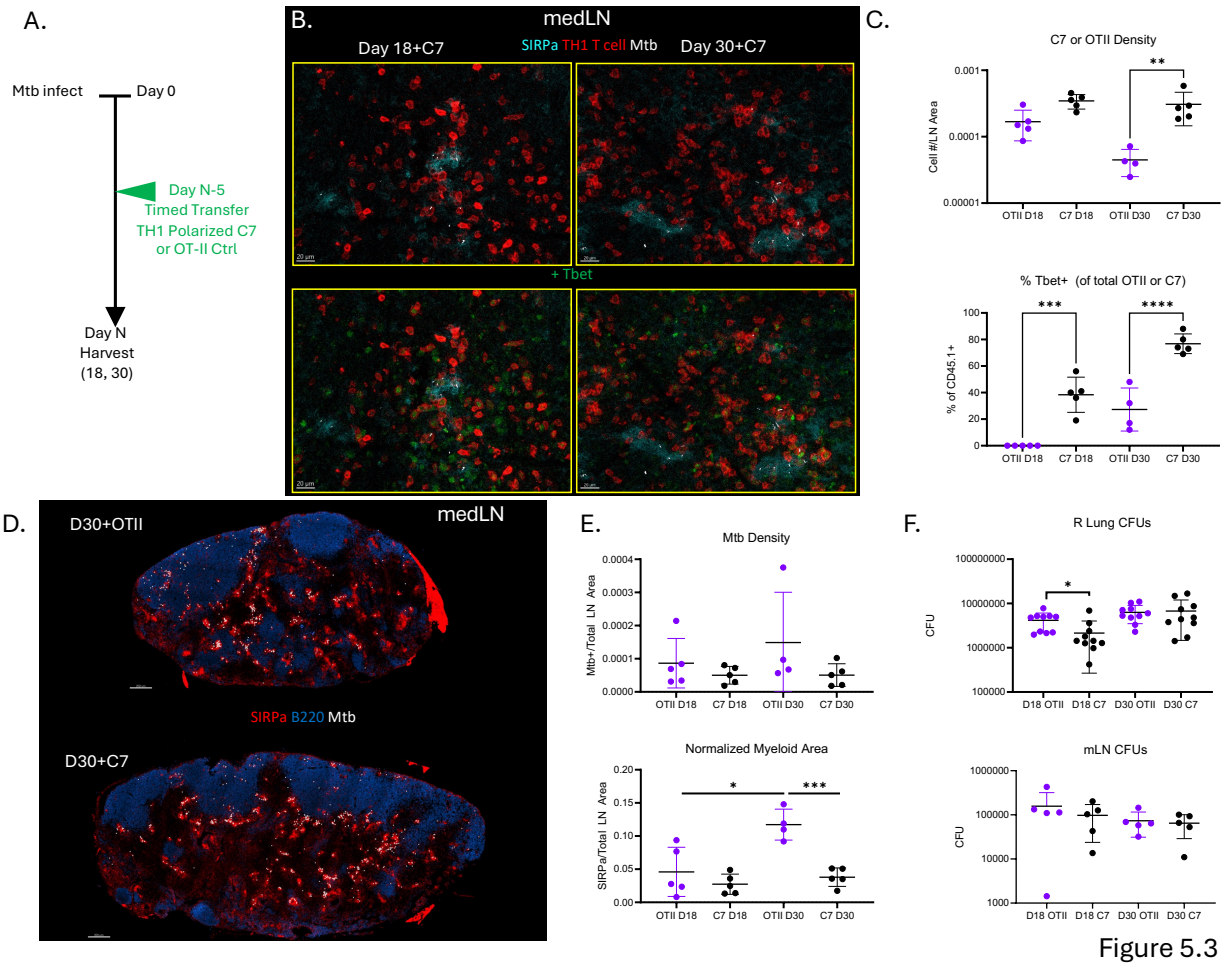

Figure 5.3

Figure 5.3: TH1 skewed effector T cells do not substantially attenuate Mtb burden in the medLN. Mtb-infected mice were adoptively transferred with 10 million C7 or OTII transgenic CD4 T cells that were TH1 polarized *ex vivo* at days 18 or 30. (A) Experimental scheme. (B-E) Confocal microscopy analysis of transferred T cell responses (B-C) and myeloid aggregates (D-E). (F) CFU analysis of right lungs or medLNs of mice.

5.3 Discussion

The overarching goal of this work is to resolve a central paradox of Mtb infection: the medLN functions as the primary site of adaptive immune priming while simultaneously serving as a reservoir for persistent bacteria. In this section, we examined how two critical components of protective immunity- cDCs and TH1-skewed effector CD4 T cells- shape immune responses within the medLN during Mtb infection. Collectively, these studies reveal intrinsic limitations of adaptive immunity that permit bacterial persistence despite robust immune activation.

Our findings demonstrate that cDCs are essential for determining the magnitude, but not the quality, of T cell responses in the medLN. Using a Zbtb46-DTR bone marrow chimera system, cDC depletion resulted in a marked reduction in both adoptively transferred and endogenous antigen-experienced T cells, while canonical TH1 effector phenotypes were preserved. These results are consistent with prior work identifying cDCs as key amplifiers of Mtb-specific T cell responses[24], while extending these conclusions using a more specific and experimentally robust depletion strategy.

The preservation of TH1 effector differentiation in the absence of cDCs suggests the presence of compensatory antigen-presenting pathways within the medLN. Monocytes, inflammatory cDC2-like populations, or LN-resident myeloid cells may provide sufficient cytokine and costimulatory signals to sustain effector differentiation once antigen is encountered[154,243]. This redundancy indicates that the medLN is not intrinsically deficient in its capacity to generate TH1-skewed immunity. Rather, limitations in immune efficacy likely arise downstream of T cell activation, at the level of antigen accessibility, spatial organization, or engagement with infected myeloid niches.

Consistent with this interpretation, depletion of migratory cDC2s in $CD11c^{cre}$ $IRF4^{fl/fl}$ mice did not impair Mtb-specific CD4 T cell activation, proliferation, or effector differentiation in the medLN, nor did it alter Mtb-infected cell numbers in the medLN or lung. Despite transcriptional evidence of migratory phenotypes among infected cDCs (Fig. 4.2A-B), these findings indicate that migratory cDC2s are not the only population that can transport Mtb or prime T cells in the

medLN. Together, these results argue that other myeloid cells can compensate for some antigen-presentation and T cell activation roles of cDCs in the medLN.

A central conceptual advance of this section is the demonstration of functional immunological blindness within the medLN. Despite the presence of activated, antigen-specific TH1 CD4 T cells, these responses fail to meaningfully engage Mtb-infected myeloid cells or reduce bacterial burden. This conclusion is supported by adoptive transfer experiments in which overwhelming numbers of *ex vivo*-polarized, Mtb-specific TH1 CD4 T cells trafficked efficiently to the medLN and reduced myeloid aggregate formation, yet failed to decrease medLN CFUs. In contrast, the same intervention significantly reduced Mtb loads in the lung at day 18, highlighting a striking tissue-specific divergence in immune efficacy.

Together, these findings support a model in which the medLN functions as a privileged niche for Mtb persistence. Unlike the lung, where granulomatous inflammation and neutrophilia can constrain bacterial growth, the medLN permits immune activation without immune efficacy. Our findings in Section 4 further contextualize this model: Mtb residing within monocytic niches appear to upregulate DosR-associated stress response pathways, consistent with adaptation to a persistent intracellular state. The greater burden of infection within monocytic compartments in the medLN, relative to the lung, likely facilitates this persistence. Although TH1 cell responses can partially restrict this niche, the accumulation of myeloid aggregates appears to create a permissive environment in which Mtb can continue to survive, as reflected by the bacterial burdens described in Section 5.2. This distinction is consistent with historical pathology and modern imaging studies demonstrating metabolically active lymph nodes in the absence of overt pulmonary disease[45]. Thus, the medLN represents not merely a site of delayed clearance, but a specialized anatomical and immunological environment that supports long-term bacterial survival.

These insights carry important implications for vaccine and immunotherapeutic design. Strategies that focus solely on enhancing TH1 responses or IFNγ production may fail to overcome the fundamental barriers imposed by LN-resident myeloid niches. Effective interventions may instead require approaches that restore antigen presentation, disrupt

permissive myeloid states, or alter spatial and metabolic constraints within lymphoid tissues. Notably, recent work identifying protective roles for non-classical and rare antigenic T cell responses[106,235,237,244-246], suggests alternative avenues for targeting immunologically silent niches not recognized by immunodominant antigen–specific T cells.

In conclusion, while cDCs initiate and amplify adaptive immune responses in the medLN, neither robust antigen presentation nor overwhelming TH1 immunity is sufficient to clear Mtb from this tissue. Instead, the medLN emerges as a distinct immunological niche characterized by immune activation uncoupled from immune efficacy, redefining how lymphoid tissues contribute to TB pathogenesis and highlighting the medLN as a critical target for future therapeutic and vaccine strategies.

6. Future Directions

6.1 Introduction

The studies presented in this dissertation establish that Mtb exploits a monocytic niche within the mediastinal lymph node to persist during early infection, while simultaneously constraining the window of effective adaptive immune priming. These findings raise several interconnected questions that motivate the future directions outlined in this chapter. First, what monocyte-intrinsic pathways sustain this permissive niche, and can they be targeted to disrupt bacterial persistence in lymphoid tissues without the delays inherent to live attenuated vaccination? Second, given that the medLN's capacity to support effector T cell differentiation is temporally limited, can alternative tissue sites (including the lung and spleen) be leveraged to extend or redirect protective adaptive responses? Third, does monocytic niche formation represent a conserved feature of mycobacterial immunity more broadly, or a vulnerability specific to Mtb? Finally, do the transcriptional programs that define these monocyte-derived cells converge with immunoregulatory myeloid states observed in other chronic inflammatory diseases, including cancer? Addressing these questions will require integrating the single-cell innate immune atlas generated here with targeted genetic, pharmacologic, and comparative infection models, and may ultimately reveal shared principles of myeloid dysfunction that extend well beyond tuberculosis.

6.2 Identifying monocyte-intrinsic mechanisms to intervene against Mtb persistence

In Section 4, we identified an Mtb-permissive monocytic niche that enables bacterial persistence within the medLN. Although this phenotype could be attenuated by BCG vaccination, BCG is a live attenuated vaccine that establish protective immunity over the course of 6 to 8 weeks. This delay highlights the need to identify monocyte-intrinsic pathways that could be targeted more directly to disrupt Mtb persistence within lymphoid tissues.

We performed a series of pilot experiments targeting cellular origins, signaling pathways, receptors, and molecules that were transcriptionally upregulated in Mtb-infected or bystander monocytes in the medLN (Fig. 4.S2G, Fig. 6.1A–C). In addition to genes highlighted in Fig. 4.S2G that were upregulated at days 15 and 28 relative to naïve day 0 iMO2s and MCs, we observed transcriptional similarities between day 22 medLN monocytes and uninfected circulating blood

monocytes, including increased expression of *Ceacam1*, *Sell*, and *Csf1r*. These observations informed the design of multiple pilot intervention studies (Fig. 6.1A–C).

The pathways and cell populations targeted included patrolling monocytes (via Nr4a1_SE2$^{-/-}$ bone-marrow chimeras), cDCs (via BATF3$^{-/-}$ mice, Zbtb46-DTR chimeras, and CD11c^{cre} IRF4$^{fl/fl}$ mice), metabolic pathways (via IRG1$^{-/-}$ bone-marrow chimeras, LysM ^{cre} Alox5f $^{fl/fl}$mice, or pharmacologic inhibition of PPARγ using GW9662), chemokine receptors (via L-selectin–blocking antibodies), IFN-I signaling (using Ifnar1$^{-/-}$ mice), immune checkpoint pathways (via PD-L1–blocking antibodies), and adhesion molecules (via CEACAM1$^{-/-}$ bone marrow chimeras). Across these models, we assessed medLN myeloid aggregate formation at timepoints corresponding to niche establishment (day 18 and later). Apart from Batf3$^{-/-}$ mice, none of these perturbations resulted in significant alterations to aggregate formation. Batf3$^{-/-}$ mice exhibited modest changes in aggregate structure (Fig. 6.1D–E); however, these effects are difficult to interpret given the broader consequences of global Batf3 deficiency, including potential effects on monocytic populations.

Importantly, many candidate pathways implicated in monocyte recruitment, differentiation, and tissue retention remain untested in the context of Mtb infection. Promising targets emerging from our transcriptional analyses include the CCR5/CCL5 axis, which has been implicated in monocyte recruitment during inflammation[247], and P-selectin (*Selplg*), which promotes monocyte migration to lymph nodes [248]. These migratory signaling axes could be interrogated using genetic models, inducible systems, or bone marrow chimera approaches to enable spatial or temporal control of target ablation.

While these examples are not exhaustive, the datasets generated in this dissertation (particularly the large-scale single-cell innate atlas of murine Mtb infection) provide a foundational resource to inform future studies aimed at identifying and disrupting Mtb-permissive monocytic niches.

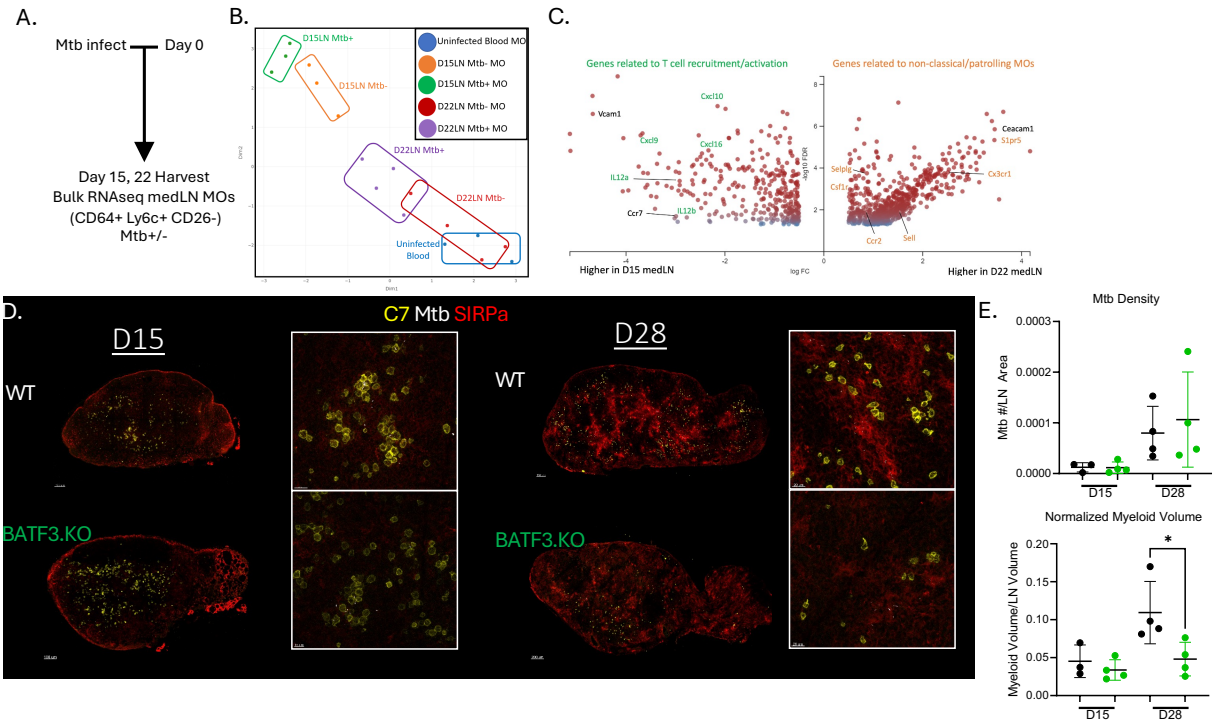

Figure 6.1

Figure 6.1: Monocytes in the medLN have differential expression of markers that can be ablated in mouse models during Mtb infection. (A-C) Mice infected with Mtb (H37Rv.mCherry 50-100 CFU) had Mtb+/- monocytes sorted for bulk RNAseq from medLNs at day 15 and 22, and blood at day 0. (A) experimental scheme. (B) PCA analysis of independent samples. (C) Differential analysis via volcano plot of total day 15 vs day 22 monocytes identifying genes of interest related to T cell recruitment/activation (green), or genes related to monocyte phenotypes (orange). (D-E) BATF3$^{-/-}$ were infected (similar to Figure 4.5 and 4.S.5) and harvested at days 15 and 28 for confocal microscopy analysis. Myeloid aggregates (SIRPa), C7 T cells, and Mtb are shown. Myeloid and Mtb density are quantified (E).

6.3 Inducing Mtb-specific adaptive responses in other tissue sites

I would like to acknowledge Cody Jenkins for his work in generating the data referred to in Fig. 6.2 during his rotation project.

In Section 4, we demonstrate that the medLN provides the most robust window for effector CD4 T cell priming during Mtb infection (Fig. 4.4). In contrast, other secondary lymphoid organs, such as the spleen, are comparatively ineffective at generating strong effector T cell responses during the same critical window between days 15 and 28 post-infection (Fig. 4.S4H, Fig. 6.2A–C). While this may initially appear to reflect a limitation of the adaptive immune system, it also suggests that other priming sites could be therapeutically leveraged to bypass the constraints imposed by the medLN during later stages of infection.

Indeed, sites of Mtb dissemination such as the spleen may represent underexplored targets for vaccination or immune modulation. Recent work has identified restriction of Mtb infection in both the lung and spleen mediated by marginal zone B cells with memory-like and activated phenotypes, which contribute to the production of TNF, IL-2, and GM-CSF[249]. These findings raise the possibility that non-T cell–centric mechanisms operating in other SLOs could complement or enhance conventional T cell–based immunity.

As the primary site of infection, the lung also serves as a site of adaptive immune activation. Persistent lung T cell responses have been observed during late Mtb infection in bisulfan-treated mice, indicating that de novo T cell responses can be sustained independently of thymic output[31]. In addition, recent studies have identified granuloma-associated lymphoid structures within the lung that function as local priming niches during Mtb infection[29].

Consistent with these findings, we observed that Mtb-specific C7 T cell priming within the lung changes dynamically over the first four weeks of infection in our timed adoptive transfer model (Fig. 6.2D-G). During the first three weeks, lung-localized C7 cells predominantly exhibited effector phenotypes and were either terminally divided or remained undivided (Fig. 6.2D). Although the total number of recovered C7 cells was comparable across timepoints, patterns of cell trace dilution and effector differentiation diverged at days 22 and 28 (Fig. 6.2D–G). These

results suggest that similar to the medLN, the lung undergoes temporal remodeling in its capacity to support T cell priming.

While these observations require further validation, particularly through experiments with longer adoptive transfer windows allowing for Mtb-specific T cell homing to the lung after priming or by S1P blockade via FTY720, they raise the possibility that the lung may become a more permissive site for adaptive priming at later stages of infection, when the medLN no longer supports robust effector differentiation. This concept aligns with emerging vaccine strategies aimed at targeting the lung directly to induce mucosal immunity and durable protection against Mtb[250,251].

Together, these findings suggest that effective TB immunotherapies may require spatial re-engineering of adaptive immune responses, either by extending the window of medLN priming or by redirecting priming to alternative tissue sites such as the lung or spleen.

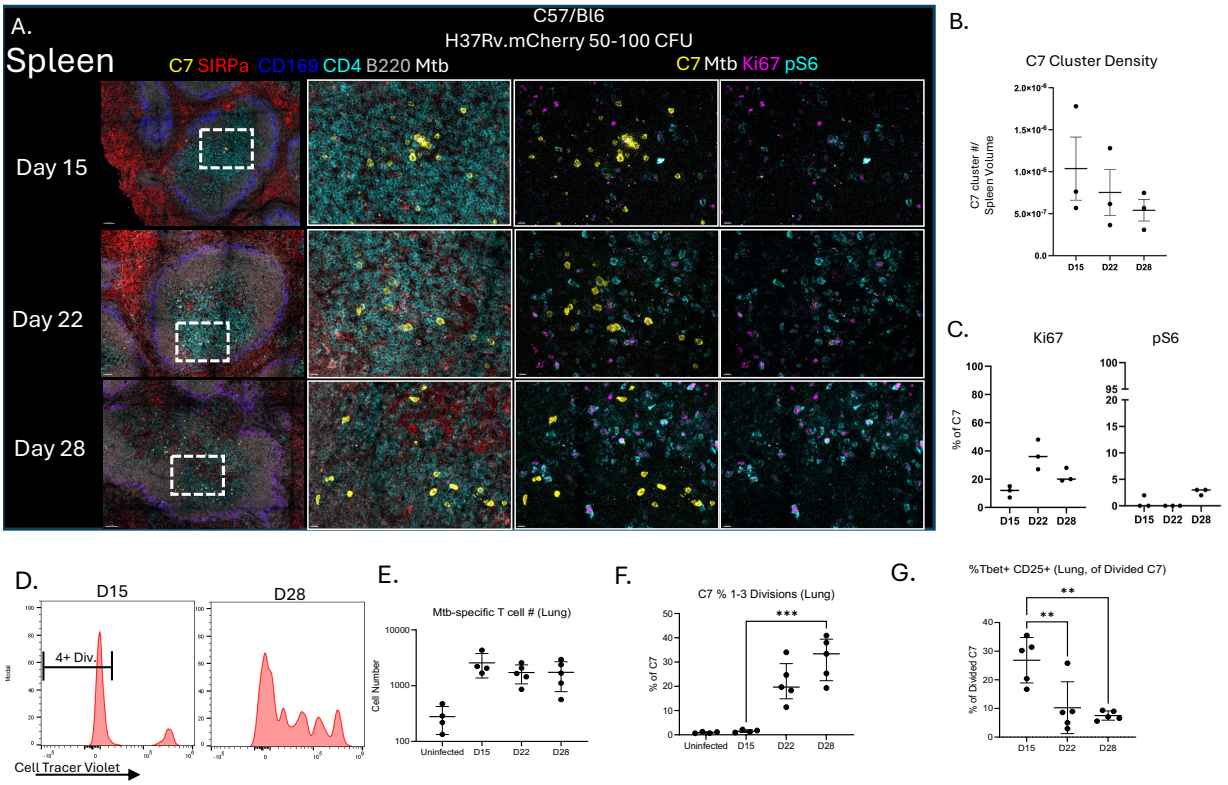

Figure 6.2

Figure 6.2: Mtb-specific T cell priming in the spleen and lung during Mtb infection. (A-G) confocal microscopy of spleens (A-C) or flow cytometry analysis of lungs (D-G) from Mtb-infected (H37Rv.mCherry 50-100 CFU) mice. (A-C) C7 T cells and structural markers shown at timepoints indicated, with quantifications for C7 cells shown (B-C). (D-G) Flow cytometry analysis of timed (D-3) adoptively transferred C7 from lungs, identifying cell numbers (E), division phenotypes (F) and T effector (Tbet+ CD25+) phenotypes (G).

6.4 The role of monocytic niches in other mycobacterial infections

As discussed in Section 1, mycobacterial infections beyond Mtb frequently involve lymphatic tissues and can persist within lymph nodes. Because the only licensed TB vaccine, BCG, is itself a live attenuated mycobacterium, we leveraged this model to explore whether monocytic niche formation represents a conserved feature of mycobacterial immunity.

To address this, we examined the spatial innate immune landscape of BCG-draining inguinal lymph nodes following subcutaneous BCG immunization administered eight weeks prior to aerosol Mtb infection. Mice were harvested at day 14 post-Mtb infection (Fig. 6.3). At this timepoint, BCG-draining lymph nodes exhibited pronounced enlargement and increased cellularity, indicative of sustained immune activation (Fig. 6.3). Strikingly, we observed substantial SIRPα$^+$ myeloid aggregates within these lymph nodes, accompanied by robust iNOS expression, resembling the monocytic aggregates described in the medLN during Mtb infection. In addition, focal Ag85B staining was detected within these structures (Fig. 6.3 zoom in), consistent with the presence of mycobacterial antigens shared between BCG and Mtb. The co-localization of iNOS within SIRPα$^+$ aggregates suggests active IFN- or TLR-mediated sensing within these innate cells, potentially reflecting persistent or slowly cleared BCG. These observations raise the possibility that formation of monocytic aggregates represents a conserved response to lymph node-localized mycobacterial infection rather than a phenomenon unique to Mtb. Future studies could directly compare the kinetics, transcriptional programs, and immune visibility of monocytic niches induced by distinct mycobacterial species, including *M. bovis*, *M. avium*, and *M. abscessus*, using parallel infection models.

Such comparative approaches may provide broader insight into immune strategies employed by mycobacteria across hosts and disease contexts, including infections that have had devastating impacts on wildlife, livestock, and avian populations[252,253]. Importantly, identifying immune mechanisms that successfully limit persistence in non-tuberculous mycobacterial infections could reveal protective pathways that are absent, suppressed, or subverted during Mtb infection, informing the development of novel host-directed or vaccine-based interventions.

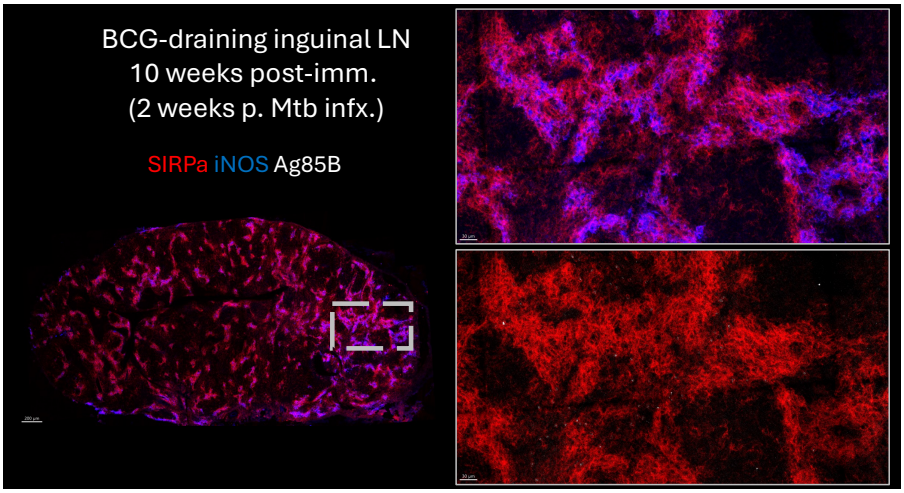

Figure 6.3

Figure 6.3: The BCG-draining LN during Mtb infection. Confocal microscopy of a BCG draining inguinal lymph node at 14 days post- Mtb infection (H37Rv.mCherry 50-100 CFU), identifying mycobacteria (Ag85B), myeloid cells (SIRPa), and iNOS.

6.5 Exploring overlapping monocytic phenotypes in other chronic disease states

Mtb infection induces a chronic inflammatory disease characterized by granuloma formation at the primary site of infection, which can limit bacterial dissemination but also disrupt normal lung architecture and function. This pathological state shares striking similarities with solid tumors, which likewise consist of dysregulated immune, stromal, and epithelial compartments, arise in mucosal tissues such as the lung, and require sustained T cell-mediated immune control. In both settings, myeloid cell recruitment is extensive and persistent, and monocytes exhibit pronounced plasticity in response to local inflammatory and metabolic cues.

Consistent with these parallels, our single-cell RNA-sequencing atlas of innate immune cells during Mtb infection identified a population of monocyte-derived cells (MCs) that comprise the myeloid aggregates in the medLN. From this dataset, we derived an MC gene signature representing the top 50 genes enriched in this population relative to other innate cell types **(Table 3.2)**. To assess whether analogous cell states exist in human disease, we converted this signature to human orthologs and interrogated its expression in patient-derived transcriptional datasets.

To this end, we leveraged the Mo-Mac-VERSE dataset, which integrates approximately 179,000 monocytes and macrophages across 13 tissues and 41 datasets spanning healthy, infectious, and malignant disease states[254]. Within this resource, we observed enrichment of the MC signature in macrophage populations annotated as $C1Q^+$, $HES1^+$, $IL4L1^+$, and $TREM2^+$ (Fig. 6.4A–B). Notably, several of these phenotypes have independently been implicated in Mtb infection and disease progression. C1Q expression has been reported as a biomarker of active TB in patient cohorts[191], while $TREM2^+$ macrophages have been associated with foamy macrophage states and spatially localized pathology in human pulmonary TB[255]. Beyond infectious disease, IL4L1-expressing macrophages are characterized in cancer, where they contribute to regulatory T cell recruitment, suppression of effector T cell function, and broader tumor microenvironment dysfunction[254]. The convergence of these transcriptional programs suggests that the monocytic niches identified in the medLN during Mtb infection may share conserved differentiation pathways and immunoregulatory functions with tumor-associated macrophages.

While these analyses remain correlative, they raise the intriguing possibility that immune-evasive monocytic niches represent a shared feature of chronic inflammatory diseases. Future studies integrating cross-disease comparative analyses among large-scale transcriptional and spatial datasets could clarify whether therapeutic strategies developed to target suppressive myeloid populations in cancer might also be repurposed to disrupt Mtb-permissive niches. Such approaches may offer novel avenues for host-directed therapies that complement conventional antimicrobial strategies and improve immune-mediated clearance of persistent Mtb infection.

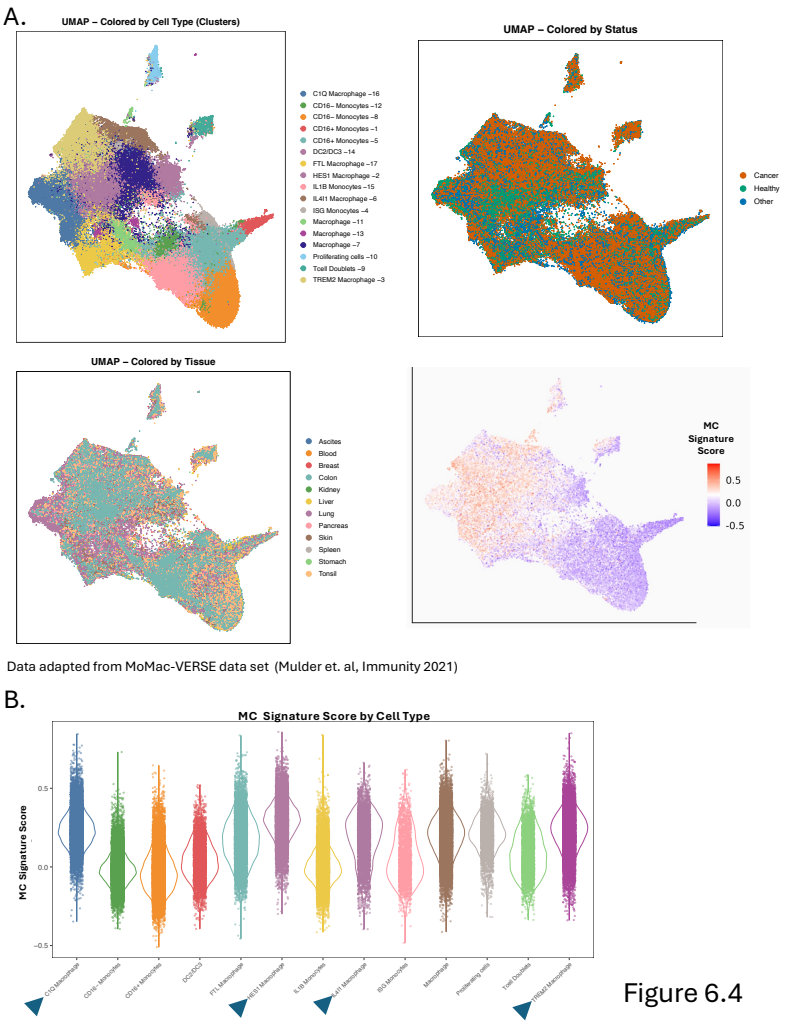

Figure 6.4

Figure 6.4: MC signatures in patient-derived monocytes and macrophages. (A) UMAP analysis of Mulder et. al 2021 dataset, indicating cell types, status, tissue, and MC-signature (Table 6.4.1) enrichment. (B) MC signature enrichment among annotated cell types from Mulder et. al 2021 dataset.

7. Conclusion

7.1 Summary

Tuberculosis remains a leading cause of infectious mortality worldwide, in part due to the extraordinary capacity of Mtb to persist within host tissues despite robust immune activation. While pulmonary infection has historically dominated models of TB pathogenesis, the work presented in this dissertation identifies the lung-draining mediastinal lymph node (medLN) as a central and underappreciated site of Mtb persistence. Through integrated spatial, transcriptional, functional, and quantitative approaches, these studies resolve a long-standing paradox: how the same lymphoid organ can initiate protective adaptive immunity while simultaneously supporting long-term bacterial survival.

In Section 4, we demonstrate that Mtb persistence in the medLN is enabled by the formation of specialized monocyte-derived cellular niches that arise following an early, transient phase of immune activation. Initial dissemination of Mtb to the medLN occurs around days 8–15 post-infection via both inflammatory monocytes and conventional dendritic cells (cDCs)[30,32,72,118], coinciding with robust induction of inflammatory cytokine signaling and efficient priming of Mtb-specific CD4 T cell responses. During this early window, individual bacilli are dispersed within myeloid cells localized to the T cell zone, and antigen presentation by cDCs supports effective TH1 differentiation.

This productive phase is short-lived. By weeks 3–4 post-infection, the medLN undergoes dramatic structural remodeling marked by the emergence of large aggregates of monocyte-derived cells harboring multiple bacilli. These aggregates persist into late infection, occupy substantial portions of the medLN parenchyma and are conserved across mouse strains, Mtb genotypes, and infectious doses. Despite strong induction of classical antimicrobial and inflammatory programs, including IFN-I, IFN-II, TNF signaling, and high iNOS expression[80,82,84,89,197,198], these monocytic niches fail to clear Mtb, establishing a stable, pathogen-permissive reservoir.

Single-cell transcriptomic analyses revealed that infected monocyte-derived cells in the medLN undergo temporal reprogramming from early inflammatory states to later programs enriched

for hypoxia, lipid metabolism, tissue repair, and cellular survival [190,193,194]. These features closely resemble previously described interstitial macrophage populations in the lung that harbor stress-adapted, DosR-expressing Mtb[95,96,190], suggesting a conserved strategy of persistence across tissues. Mathematical modeling and organ-tracing experiments further demonstrate that rising medLN bacterial burdens cannot be explained by continued trafficking from the lung alone, but instead require substantial local bacterial replication within the medLN itself, at rates comparable to those in the lung.

Section 4 further establishes that effective Mtb-specific CD4 T cell priming in the medLN is temporally restricted and supported by sequential waves of cDC subset activity. Early after infection, cDC1s serve as dominant IL-12–producing antigen-presenting cells driving robust TH1 differentiation[81,177,207,208]. As infection progresses, elevated type I interferon signaling induces the emergence of inflammatory cDC2s (inf-cDC2s), which acquire monocyte-like features while retaining IL-12 production capacity[174,243]. These inf-cDC2s transiently sustain CD4 T cell responses as cDC1 activity wanes. Over time, however, migration of Mtb-infected cDCs from the lung declines, IFN-I sensing within the medLN diminishes, and both cDC1- and inf-cDC2-mediated priming collapses, coincident with establishment of the monocytic niche.

A central conceptual advance of this work is the identification of functional immunological blindness within the medLN. Although Mtb-specific CD4 T cells are generated and persist within the tissue, they fail to efficiently recognize or respond to infected monocyte-derived aggregates at later stages of infection. This defect persists despite direct physical proximity between T cells and infected cells and is marked by diminished pS6 and IRF4 signaling, indicating impaired antigen recognition. While Mtb is known to suppress antigen presentation through multiple mechanisms[225-229], the persistence of high MHC-II expression on infected cells suggests additional barriers to immune engagement. These likely include local immunosuppression mediated by PD-L1 and nitric oxide[89-92,197], as well as altered antigen repertoires associated with bacterial dormancy[93-96,233,234]. The enrichment of non-classical MHC-I molecules such as Qa-1 (H2-T23) on infected cells further suggests that dominant CD4 T cell responses may be mismatched to the antigens presented within persistent niches[237-240].

BCG immunization provides important insight into how this niche can be perturbed. As shown in Section 4, BCG markedly reduces Mtb burden and limits formation of monocytic aggregates in the medLN[184,185] without preventing initial dissemination from the lung or altering early cDC-mediated T cell priming. Instead, BCG reduces recruitment of blood-derived monocytes to the medLN, dampens IFN-I/II signaling within medLN myeloid cells, and accelerates immune control of bacterial growth, thereby constraining expansion of the monocytic niche. Barcode-based dissemination studies further demonstrate that while BCG restricts spread to distal organs such as the contralateral lung[184], it does not alter which Mtb clones access the medLN, reinforcing the conclusion that BCG acts locally to limit replication and niche establishment rather than blocking dissemination.

Building on these findings, Section 5 demonstrates that even overwhelming the immune system with large numbers of ex vivo–polarized, TH1-skewed, Mtb-specific CD4 T cells is insufficient to clear Mtb from the medLN, despite effectively reducing bacterial burden in the lung. Depletion of cDCs reduced the magnitude of T cell responses but preserved effector differentiation, while migratory cDC2 depletion did not alter T cell responses, revealing compensatory antigen-presention within the medLN. Together, these data show that the medLN is not intrinsically incapable of sustaining TH1 immunity. Rather, immune efficacy becomes uncoupled from immune activation once Mtb establishes residence within monocyte-derived niches.

Motivated by the prior sections, future directions explored in section 6 aimed at translating these mechanistic insights into actionable interventions. The identification of a transcriptionally dynamic, Mtb permissive monocytic niche raises the immediate question of which monocyte intrinsic pathways sustain it and whether they can be targeted more rapidly than BCG mediated protection allows. Pilot studies interrogating monocyte recruitment, metabolic reprogramming, checkpoint signaling, and adhesion molecules have begun to narrow this space, with emerging candidates including the CCR5/CCL5 and P selectin axes. The temporal collapse of medLN priming capacity further raises the possibility that alternative lymphoid and mucosal sites, including the spleen and lung, could be therapeutically engaged to extend or redirect protective adaptive responses. Whether monocytic niche formation is unique to Mtb or represents a conserved mycobacterial immune evasion strategy is examined through BCG draining lymph

node models, which reveal strikingly similar aggregate structures. Finally, cross disease transcriptional analyses suggest that the monocyte derived cells comprising these niches share differentiation programs with immunoregulatory macrophage states in human cancer, raising the possibility that shared therapeutic vulnerabilities exist across disease contexts.

Altogether, this dissertation redefines the medLN as a dynamic immunological site that rapidly transitions from a hub of adaptive immune induction to a privileged reservoir of persistent infection. Early after infection, coordinated cDC subset activity enables effective TH1 priming. However, this window closes as Mtb establishes metabolically adapted, immunologically evasive monocytic niches that resist T cell–mediated clearance despite robust inflammatory signaling. These findings help explain longstanding observations of lymph node involvement in subclinical TB[45,46] and provide a mechanistic framework for understanding why vaccines and immunotherapies that robustly induce TH1 responses often fail to achieve sterilizing immunity. Effective TB control strategies will likely require interventions that specifically target lymphoid tissue niches, alter monocyte recruitment or differentiation, restore antigen visibility, or expand immune recognition beyond immunodominant epitopes. By highlighting the tissue-specific and temporally dynamic nature of host–pathogen interactions, this work underscores the necessity of moving beyond lung-centric models of TB pathogenesis and positions the medLN as a critical target for next-generation therapeutic and vaccine strategies.

7.2 Concluding Remarks

Tuberculosis persists as a global health threat not only because Mtb escapes immune recognition, but because it is able to endure within host microenvironments that are immunologically active yet functionally ineffective. The work presented in this dissertation reframes the lung-draining mediastinal lymph node as a central site where this paradox is most clearly revealed. Rather than serving exclusively as a conduit for protective immunity, the medLN is shown to undergo a rapid transformation that permits bacterial persistence alongside ongoing immune activation.

Across experimental systems, these studies demonstrate that effective adaptive immune responses can be generated without achieving bacterial clearance. Early during infection, the

medLN supports inflammatory responses, robust antigen presentation, and T cell priming; however, this capacity is temporally limited and ultimately gives way to monocyte-dominated niches that enable Mtb persistence and are poorly engaged by antigen-specific T cells. These findings highlight that immune failure in tuberculosis does not arise from an absence of immunity, but from a fundamental disconnect between immune responses and the dominant cellular reservoirs of infection. By identifying monocyte-derived niches within lymphoid tissue as stable sites of persistence, this work challenges prevailing assumptions that enhancing canonical TH1 responses alone is sufficient for protection. Instead, it emphasizes that tissue context, cellular differentiation state, and spatial organization critically shape immune efficacy. In this light, lymph nodes emerge not only as sites of immune initiation, but also as environments that can be actively co-opted to sustain chronic infection.

Together, the findings presented here underscore the need to broaden how protective immunity against tuberculosis is defined and evaluated. Durable control will likely require strategies that target the cellular and anatomical contexts that support persistence, rather than focusing solely on amplifying immune activation. By redefining the role of the medLN in tuberculosis pathogenesis, this dissertation provides a framework for understanding how immune responses can be both potent and insufficient, thus offering insight into how this balance might ultimately be shifted toward sterilizing protection.

References

1. (WHO), W.H.O. (2024). Global Tuberculosis Report 2024.
2. Bottai, D., Stinear, T.P., Supply, P., and Brosch, R. (2014). Mycobacterial Pathogenomics and Evolution. Microbiol Spectr *2*, MGM2-0025-2013. 10.1128/microbiolspec.MGM2-0025-2013.
3. Malhotra, A.M., Arias, M., Backx, M., Gadsby, J., Goodman, A., Gourlay, Y., Milburn, H., Moncayo-Nieto, O.L., Shimmin, D., Dedicoat, M., and Kunst, H. (2024). Extrapulmonary nontuberculous mycobacterial infections: a guide for the general physician. Clin Med (Lond) *24*, 100016. 10.1016/j.clinme.2024.100016.
4. Adams, L.B. (2021). Susceptibility and resistance in leprosy: Studies in the mouse model. Immunol Rev *301*, 157-174. 10.1111/imr.12960.
5. Martiniano, S.L., Nick, J.A., and Daley, C.L. (2016). Nontuberculous Mycobacterial Infections in Cystic Fibrosis. Clin Chest Med *37*, 83-96. 10.1016/j.ccm.2015.11.001.
6. Naranjo, V., Gortazar, C., Vicente, J., and de la Fuente, J. (2008). Evidence of the role of European wild boar as a reservoir of Mycobacterium tuberculosis complex. Vet Microbiol *127*, 1-9. 10.1016/j.vetmic.2007.10.002.
7. Fitzgerald, S.D., and Kaneene, J.B. (2013). Wildlife reservoirs of bovine tuberculosis worldwide: hosts, pathology, surveillance, and control. Vet Pathol *50*, 488-499. 10.1177/0300985812467472.
8. Zimpel, C.K., Patané, J.S.L., Guedes, A.C.P., de Souza, R.F., Silva-Pereira, T.T., Camargo, N.C.S., de Souza Filho, A.F., Ikuta, C.Y., Neto, J.S.F., Setubal, J.C., et al. (2020). Global Distribution and Evolution of. Front Microbiol *11*, 843. 10.3389/fmicb.2020.00843.
9. Olea-Popelka, F., Muwonge, A., Perera, A., Dean, A.S., Mumford, E., Erlacher-Vindel, E., Forcella, S., Silk, B.J., Ditiu, L., El Idrissi, A., et al. (2017). Zoonotic tuberculosis in human beings caused by Mycobacterium bovis-a call for action. Lancet Infect Dis *17*, e21-e25. 10.1016/S1473-3099(16)30139-6.
10. Gröschel, M.I., Sayes, F., Simeone, R., Majlessi, L., and Brosch, R. (2016). ESX secretion systems: mycobacterial evolution to counter host immunity. Nat Rev Microbiol *14*, 677-691. 10.1038/nrmicro.2016.131.
11. Shah, S., Bohsali, A., Ahlbrand, S.E., Srinivasan, L., Rathinam, V.A., Vogel, S.N., Fitzgerald, K.A., Sutterwala, F.S., and Briken, V. (2013). Cutting edge: Mycobacterium tuberculosis but not nonvirulent mycobacteria inhibits IFN-β and AIM2 inflammasome-dependent IL-1β production via its ESX-1 secretion system. J Immunol *191*, 3514-3518. 10.4049/jimmunol.1301331.
12. Riley, R.L., Mills, C.C., Nyka, W., Weinstock, N., Storey, P.B., Sultan, L.U., Riley, M.C., and Wells, W.F. (1995). Aerial dissemination of pulmonary tuberculosis. A two-year study of contagion in a tuberculosis ward. 1959. Am J Epidemiol *142*, 3-14. 10.1093/oxfordjournals.aje.a117542.
13. Saini, D., Hopkins, G.W., Seay, S.A., Chen, C.J., Perley, C.C., Click, E.M., and Frothingham, R. (2012). Ultra-low dose of Mycobacterium tuberculosis aerosol creates partial infection in mice. Tuberculosis (Edinb) *92*, 160-165. 10.1016/j.tube.2011.11.007.

14. Plumlee, C.R., Duffy, F.J., Gern, B.H., Delahaye, J.L., Cohen, S.B., Stoltzfus, C.R., Rustad, T.R., Hansen, S.G., Axthelm, M.K., Picker, L.J., et al. (2021). Ultra-low Dose Aerosol Infection of Mice with Mycobacterium tuberculosis More Closely Models Human Tuberculosis. Cell Host Microbe *29*, 68-82.e65. 10.1016/j.chom.2020.10.003.
15. Coussens, A.K., Zaidi, S.M.A., Allwood, B.W., Dewan, P.K., Gray, G., Kohli, M., Kredo, T., Marais, B.J., Marks, G.B., Martinez, L., et al. (2024). Classification of early tuberculosis states to guide research for improved care and prevention: an international Delphi consensus exercise. Lancet Respir Med *12*, 484-498. 10.1016/S2213-2600(24)00028-6.
16. Alonzi, T., Petruccioli, E., Aiello, A., Repele, F., and Goletti, D. (2025). Diagnostic tests for tuberculosis infection and predictive indicators of disease progression: Utilizing host and pathogen biomarkers to enhance the tuberculosis elimination strategies. Int J Infect Dis *155*, 107880. 10.1016/j.ijid.2025.107880.
17. Luetkemeyer, A.F., Firnhaber, C., Kendall, M.A., Wu, X., Mazurek, G.H., Benator, D.A., Arduino, R., Fernandez, M., Guy, E., Johnson, P., et al. (2016). Evaluation of Xpert MTB/RIF Versus AFB Smear and Culture to Identify Pulmonary Tuberculosis in Patients With Suspected Tuberculosis From Low and Higher Prevalence Settings. Clin Infect Dis *62*, 1081-1088. 10.1093/cid/ciw035.
18. Liu, J.J., Feng, Y.P., Liu, Z.D., and Guo, J. (2024). Impact of delayed diagnosis and treatment on tuberculosis infection within families: A case report. Medicine (Baltimore) *103*, e37406. 10.1097/MD.0000000000037406.
19. Bello, S., Afolabi, R.F., Ajayi, D.T., Sharma, T., Owoeye, D.O., Oduyoye, O., and Jasanya, J. (2019). Empirical evidence of delays in diagnosis and treatment of pulmonary tuberculosis: systematic review and meta-regression analysis. BMC Public Health *19*, 820. 10.1186/s12889-019-7026-4.
20. Cohen, S.B., Gern, B.H., Delahaye, J.L., Adams, K.N., Plumlee, C.R., Winkler, J.K., Sherman, D.R., Gerner, M.Y., and Urdahl, K.B. (2018). Alveolar Macrophages Provide an Early Mycobacterium tuberculosis Niche and Initiate Dissemination. Cell Host Microbe *24*, 439-446.e434. 10.1016/j.chom.2018.08.001.
21. Rothchild, A.C., Olson, G.S., Nemeth, J., Amon, L.M., Mai, D., Gold, E.S., Diercks, A.H., and Aderem, A. (2019). Alveolar macrophages generate a noncanonical NRF2-driven transcriptional response. Sci Immunol *4*. 10.1126/sciimmunol.aaw6693.
22. Norris, B.A., and Ernst, J.D. (2018). Mononuclear cell dynamics in M. tuberculosis infection provide opportunities for therapeutic intervention. PLoS Pathog *14*, e1007154. 10.1371/journal.ppat.1007154.
23. Huang, L., Nazarova, E.V., Tan, S., Liu, Y., and Russell, D.G. (2018). Growth of M*ycobacterium tuberculosis* in vivo segregates with host macrophage metabolism and ontogeny. J Exp Med *215*, 1135-1152. 10.1084/jem.20172020.
24. Samstein, M., Schreiber, H.A., Leiner, I.M., Susac, B., Glickman, M.S., and Pamer, E.G. (2013). Essential yet limited role for $CCR2^{+}$ inflammatory monocytes during Mycobacterium tuberculosis-specific T cell priming. Elife *2*, e01086. 10.7554/eLife.01086.

25. Cooper, A.M., Roberts, A.D., Rhoades, E.R., Callahan, J.E., Getzy, D.M., and Orme, I.M. (1995). The role of interleukin-12 in acquired immunity to Mycobacterium tuberculosis infection. Immunology *84*, 423-432.
26. Cohen, S.B., Gern, B.H., and Urdahl, K.B. (2022). The Tuberculous Granuloma and Preexisting Immunity. Annu Rev Immunol *40*, 589-614. 10.1146/annurev-immunol-093019-125148.
27. Tsai, M.C., Chakravarty, S., Zhu, G., Xu, J., Tanaka, K., Koch, C., Tufariello, J., Flynn, J., and Chan, J. (2006). Characterization of the tuberculous granuloma in murine and human lungs: cellular composition and relative tissue oxygen tension. Cell Microbiol *8*, 218-232. 10.1111/j.1462-5822.2005.00612.x.
28. Ulrichs, T., Kosmiadi, G.A., Trusov, V., Jörg, S., Pradl, L., Titukhina, M., Mishenko, V., Gushina, N., and Kaufmann, S.H. (2004). Human tuberculous granulomas induce peripheral lymphoid follicle-like structures to orchestrate local host defence in the lung. J Pathol *204*, 217-228. 10.1002/path.1628.
29. Swanson, R.V., Gupta, A., Foreman, T.W., Lu, L., Choreno-Parra, J.A., Mbandi, S.K., Rosa, B.A., Akter, S., Das, S., Ahmed, M., et al. (2023). Antigen-specific B cells direct T follicular-like helper cells into lymphoid follicles to mediate Mycobacterium tuberculosis control. Nat Immunol *24*, 855-868. 10.1038/s41590-023-01476-3.
30. Reiley, W.W., Calayag, M.D., Wittmer, S.T., Huntington, J.L., Pearl, J.E., Fountain, J.J., Martino, C.A., Roberts, A.D., Cooper, A.M., Winslow, G.M., and Woodland, D.L. (2008). ESAT-6-specific CD4 T cell responses to aerosol Mycobacterium tuberculosis infection are initiated in the mediastinal lymph nodes. Proc Natl Acad Sci U S A *105*, 10961-10966. 10.1073/pnas.0801496105.
31. Reiley, W.W., Wittmer, S.T., Ryan, L.M., Eaton, S.M., Haynes, L., Winslow, G.M., and Woodland, D.L. (2012). Maintenance of peripheral T cell responses during Mycobacterium tuberculosis infection. J Immunol *189*, 4451-4458. 10.4049/jimmunol.1201153.
32. Chackerian, A.A., Alt, J.M., Perera, T.V., Dascher, C.C., and Behar, S.M. (2002). Dissemination of Mycobacterium tuberculosis is influenced by host factors and precedes the initiation of T-cell immunity. Infect Immun *70*, 4501-4509. 10.1128/IAI.70.8.4501-4509.2002.
33. Sharma, S.K., and Mohan, A. (2004). Extrapulmonary tuberculosis. Indian J Med Res *120*, 316-353.
34. Fanning, A. (1999). Tuberculosis: 6. Extrapulmonary disease. CMAJ *160*, 1597-1603.
35. El Sahly, H.M., Teeter, L.D., Pan, X., Musser, J.M., and Graviss, E.A. (2007). Mortality associated with central nervous system tuberculosis. J Infect *55*, 502-509. 10.1016/j.jinf.2007.08.008.
36. Lapinel, N.C., Jolley, S.E., Ali, J., and Welsh, D.A. (2019). Prevalence of non-tuberculous mycobacteria in HIV-infected patients admitted to hospital with pneumonia. Int J Tuberc Lung Dis *23*, 491-497. 10.5588/ijtld.18.0336.
37. Wu, U.I., and Holland, S.M. (2015). Host susceptibility to non-tuberculous mycobacterial infections. Lancet Infect Dis *15*, 968-980. 10.1016/S1473-3099(15)00089-4.

38. Luca, S., and Mihaescu, T. (2013). History of BCG Vaccine. Maedica (Bucur) *8*, 53-58.
39. Schembri Higgans, J., Pace, K., Sciberras, J., and Scicluna, W. (2021). Systemic BCGosis following intra-renal instillation of BCG: a case report. J Surg Case Rep *2021*, rjab544. 10.1093/jscr/rjab544.
40. Oladiran, O., Nwosu, I., Oladunjoye, A., and Oladunjoye, O. (2020). Disseminated BCG sepsis following intravesical therapy for Bladder Carcinoma: A case report and review of literature. J Community Hosp Intern Med Perspect *10*, 168-170. 10.1080/20009666.2020.1742475.
41. Lukacs, S., Tschobotko, B., Szabo, N.A., and Symes, A. (2013). Systemic BCG-Osis as a Rare Side Effect of Intravesical BCG Treatment for Superficial Bladder Cancer. Case Rep Urol *2013*, 821526. 10.1155/2013/821526.
42. Miller, F.W. (2023). The increasing prevalence of autoimmunity and autoimmune diseases: an urgent call to action for improved understanding, diagnosis, treatment, and prevention. Curr Opin Immunol *80*, 102266. 10.1016/j.coi.2022.102266.
43. Hunter, R.L. (2018). The Pathogenesis of Tuberculosis: The Early Infiltrate of Post-primary (Adult Pulmonary) Tuberculosis: A Distinct Disease Entity. Front Immunol *9*, 2108. 10.3389/fimmu.2018.02108.
44. Donald, P.R., Diacon, A.H., and Thee, S. (2021). Anton Ghon and His Colleagues and Their Studies of the Primary Focus and Complex of Tuberculosis Infection and Their Relevance for the Twenty-First Century. Respiration *100*, 557-567. 10.1159/000509522.
45. Behr, M.A., and Waters, W.R. (2014). Is tuberculosis a lymphatic disease with a pulmonary portal? Lancet Infect Dis *14*, 250-255. 10.1016/S1473-3099(13)70253-6.
46. Opie, E.L., and Aronson, J.D. (1927). Tubercle bacilli in latent tuberculosis lesions and in lung tissue without tuberculosis lesions.
47. Robertson, H.E. (1933). The Persistence of Tuberculous Infections. Am J Pathol *9*, 711-718.711.
48. HC, S. (1933). Studies on the pathogenesis of primary tuberculosis infections. 1. The regressive lesions. .
49. CANETTI, G. (1950). Exogenous reinfection and pulmonary tuberculosis a study of the pathology. Tubercle *31*, 224-233. 10.1016/s0041-3879(50)80092-2.
50. Ghesani, N., Patrawalla, A., Lardizabal, A., Salgame, P., and Fennelly, K.P. (2014). Increased cellular activity in thoracic lymph nodes in early human latent tuberculosis infection. Am J Respir Crit Care Med *189*, 748-750. 10.1164/rccm.201311-1976LE.
51. Huang, J.Y., Lyons-Cohen, M.R., and Gerner, M.Y. (2022). Information flow in the spatiotemporal organization of immune responses. Immunol Rev *306*, 93-107. 10.1111/imr.13046.
52. Lian, J., and Luster, A.D. (2015). Chemokine-guided cell positioning in the lymph node orchestrates the generation of adaptive immune responses. Curr Opin Cell Biol *36*, 1-6. 10.1016/j.ceb.2015.05.003.
53. Wendland, M., Willenzon, S., Kocks, J., Davalos-Misslitz, A.C., Hammerschmidt, S.I., Schumann, K., Kremmer, E., Sixt, M., Hoffmeyer, A., Pabst, O., and Förster, R.

(2011). Lymph node T cell homeostasis relies on steady state homing of dendritic cells. Immunity *35*, 945-957. 10.1016/j.immuni.2011.10.017.

54. Potter, E.L., Gideon, H.P., Tkachev, V., Fabozzi, G., Chassiakos, A., Petrovas, C., Darrah, P.A., Lin, P.L., Foulds, K.E., Kean, L.S., et al. (2021). Measurement of leukocyte trafficking kinetics in macaques by serial intravascular staining. Sci Transl Med *13*. 10.1126/scitranslmed.abb4582.
55. Alberts-Grill, N., Denning, T.L., Rezvan, A., and Jo, H. (2013). The role of the vascular dendritic cell network in atherosclerosis. Am J Physiol Cell Physiol *305*, C1-21. 10.1152/ajpcell.00017.2013.
56. Gerner, M.Y., Kastenmuller, W., Ifrim, I., Kabat, J., and Germain, R.N. (2012). Histo-cytometry: a method for highly multiplex quantitative tissue imaging analysis applied to dendritic cell subset microanatomy in lymph nodes. Immunity *37*, 364-376. 10.1016/j.immuni.2012.07.011.
57. Junt, T., Moseman, E.A., Iannacone, M., Massberg, S., Lang, P.A., Boes, M., Fink, K., Henrickson, S.E., Shayakhmetov, D.M., Di Paolo, N.C., et al. (2007). Subcapsular sinus macrophages in lymph nodes clear lymph-borne viruses and present them to antiviral B cells. Nature *450*, 110-114. 10.1038/nature06287.
58. Bogoslowski, A., and Kubes, P. (2018). Lymph Nodes: The Unrecognized Barrier against Pathogens. ACS Infect Dis *4*, 1158-1161. 10.1021/acsinfecdis.8b00111.
59. Gasteiger, G., Ataide, M., and Kastenmüller, W. (2016). Lymph node - an organ for T-cell activation and pathogen defense. Immunol Rev *271*, 200-220. 10.1111/imr.12399.
60. Huang, J.Y., and Gerner, M.Y. (2026). Dendritic cells regulate the innate-adaptive balance in lymph nodes for optimal host defense. Cell *189*, 548-568.e519. 10.1016/j.cell.2025.11.027.
61. Ganchua, S.K.C., White, A.G., Klein, E.C., and Flynn, J.L. (2020). Lymph nodes-The neglected battlefield in tuberculosis. PLoS Pathog *16*, e1008632. 10.1371/journal.ppat.1008632.
62. Liu, C.H., Liu, H., and Ge, B. (2017). Innate immunity in tuberculosis: host defense vs pathogen evasion. Cell Mol Immunol *14*, 963-975. 10.1038/cmi.2017.88.
63. Kleinnijenhuis, J., Oosting, M., Joosten, L.A., Netea, M.G., and Van Crevel, R. (2011). Innate immune recognition of Mycobacterium tuberculosis. Clin Dev Immunol *2011*, 405310. 10.1155/2011/405310.
64. Palucci, I., Camassa, S., Cascioferro, A., Sali, M., Anoosheh, S., Zumbo, A., Minerva, M., Iantomasi, R., De Maio, F., Di Sante, G., et al. (2016). PE_PGRS33 Contributes to Mycobacterium tuberculosis Entry in Macrophages through Interaction with TLR2. PLoS One *11*, e0150800. 10.1371/journal.pone.0150800.
65. Guo, Q., Bi, J., Li, M., Ge, W., Xu, Y., Fan, W., Wang, H., and Zhang, X. (2019). ESX Secretion-Associated Protein C From. Front Cell Infect Microbiol *9*, 158. 10.3389/fcimb.2019.00158.
66. Faridgohar, M., and Nikoueinejad, H. (2017). New findings of Toll-like receptors involved in Mycobacterium tuberculosis infection. Pathog Glob Health *111*, 256-264. 10.1080/20477724.2017.1351080.

67. Guirado, E., Schlesinger, L.S., and Kaplan, G. (2013). Macrophages in tuberculosis: friend or foe. Semin Immunopathol *35*, 563-583. 10.1007/s00281-013-0388-2.
68. Basu, S., and Fenton, M.J. (2004). Toll-like receptors: function and roles in lung disease. Am J Physiol Lung Cell Mol Physiol *286*, L887-892. 10.1152/ajplung.00323.2003.
69. Gern, B.H., Klas, J.M., Foster, K.A., Kanagy, M.E., Cohen, S.B., Plumlee, C.R., Duffy, F.J., Neal, M.L., Halima, M., Gustin, A.T., et al. (2025). Early and opposing neutrophil and CD4 T cell responses shape pulmonary tuberculosis pathology. J Exp Med *222*. 10.1084/jem.20250161.
70. Kotov, D.I., Lee, O.V., Fattinger, S.A., Langner, C.A., Guillen, J.V., Peters, J.M., Moon, A., Burd, E.M., Witt, K.C., Stetson, D.B., et al. (2023). Early cellular mechanisms of type I interferon-driven susceptibility to tuberculosis. Cell *186*, 5536-5553.e5522. 10.1016/j.cell.2023.11.002.
71. Srivastava, S., Grace, P.S., and Ernst, J.D. (2016). Antigen Export Reduces Antigen Presentation and Limits T Cell Control of M. tuberculosis. Cell Host Microbe *19*, 44-54. 10.1016/j.chom.2015.12.003.
72. Srivastava, S., and Ernst, J.D. (2014). Cell-to-cell transfer of M. tuberculosis antigens optimizes CD4 T cell priming. Cell Host Microbe *15*, 741-752. 10.1016/j.chom.2014.05.007.
73. Lu, Y.J., Barreira-Silva, P., Boyce, S., Powers, J., Cavallo, K., and Behar, S.M. (2021). CD4 T cell help prevents CD8 T cell exhaustion and promotes control of Mycobacterium tuberculosis infection. Cell Rep *36*, 109696. 10.1016/j.celrep.2021.109696.
74. Winchell, C.G., Nyquist, S.K., Chao, M.C., Maiello, P., Myers, A.J., Hopkins, F., Chase, M., Gideon, H.P., Patel, K.V., Bromley, J.D., et al. (2023). CD8+ lymphocytes are critical for early control of tuberculosis in macaques. J Exp Med *220*. 10.1084/jem.20230707.
75. Simonson, A.W., Zeppa, J.J., Bucsan, A.N., Chao, M.C., Pokkali, S., Hopkins, F., Chase, M.R., Vickers, A.J., Sutton, M.S., Winchell, C.G., et al. (2025). Intravenous BCG-mediated protection against tuberculosis requires CD4+ T cells and CD8α+ lymphocytes. J Exp Med *222*. 10.1084/jem.20241571.
76. Jones, B.E., Young, S.M., Antoniskis, D., Davidson, P.T., Kramer, F., and Barnes, P.F. (1993). Relationship of the manifestations of tuberculosis to CD4 cell counts in patients with human immunodeficiency virus infection. Am Rev Respir Dis *148*, 1292-1297. 10.1164/ajrccm/148.5.1292.
77. Mogues, T., Goodrich, M.E., Ryan, L., LaCourse, R., and North, R.J. (2001). The relative importance of T cell subsets in immunity and immunopathology of airborne Mycobacterium tuberculosis infection in mice. J Exp Med *193*, 271-280. 10.1084/jem.193.3.271.
78. Srivastava, S., and Ernst, J.D. (2013). Cutting edge: Direct recognition of infected cells by CD4 T cells is required for control of intracellular Mycobacterium tuberculosis in vivo. J Immunol *191*, 1016-1020. 10.4049/jimmunol.1301236.
79. Mortensen, R., Arlehamn, C.S.L., Coler, R.N., Gerner, M.Y., Goletti, D., Lewinsohn, D.A., Modlin, R.L., Musvosvi, M., Rengarajan, J., Urdahl, K.B., et al. (2026). T cell-

macrophage interactions in tuberculosis: What we've got here is failure to communicate. J Intern Med *299*, 44-65. 10.1111/joim.70028.

80. Mishra, B.B., Rathinam, V.A., Martens, G.W., Martinot, A.J., Kornfeld, H., Fitzgerald, K.A., and Sassetti, C.M. (2013). Nitric oxide controls the immunopathology of tuberculosis by inhibiting NLRP3 inflammasome-dependent processing of IL-1β. Nat Immunol *14*, 52-60. 10.1038/ni.2474.
81. Magram, J., Connaughton, S.E., Warrier, R.R., Carvajal, D.M., Wu, C.Y., Ferrante, J., Stewart, C., Sarmiento, U., Faherty, D.A., and Gately, M.K. (1996). IL-12-deficient mice are defective in IFN gamma production and type 1 cytokine responses. Immunity *4*, 471-481. 10.1016/s1074-7613(00)80413-6.
82. Flynn, J.L., Chan, J., Triebold, K.J., Dalton, D.K., Stewart, T.A., and Bloom, B.R. (1993). An essential role for interferon gamma in resistance to Mycobacterium tuberculosis infection. J Exp Med *178*, 2249-2254. 10.1084/jem.178.6.2249.
83. Browne, S.K., Burbelo, P.D., Chetchotisakd, P., Suputtamongkol, Y., Kiertiburanakul, S., Shaw, P.A., Kirk, J.L., Jutivorakool, K., Zaman, R., Ding, L., et al. (2012). Adult-onset immunodeficiency in Thailand and Taiwan. N Engl J Med *367*, 725-734. 10.1056/NEJMoa1111160.
84. Maciag, K., Plumlee, C.R., Cohen, S.B., Gern, B.H., and Urdahl, K.B. (2024). Reappraising the Role of T Cell-Derived IFN-γ in Restriction of Mycobacterium tuberculosis in the Murine Lung. J Immunol *213*, 339-346. 10.4049/jimmunol.2400145.
85. MacMicking, J.D., North, R.J., LaCourse, R., Mudgett, J.S., Shah, S.K., and Nathan, C.F. (1997). Identification of nitric oxide synthase as a protective locus against tuberculosis. Proc Natl Acad Sci U S A *94*, 5243-5248. 10.1073/pnas.94.10.5243.
86. Chan, J., Tanaka, K., Carroll, D., Flynn, J., and Bloom, B.R. (1995). Effects of nitric oxide synthase inhibitors on murine infection with Mycobacterium tuberculosis. Infect Immun *63*, 736-740. 10.1128/iai.63.2.736-740.1995.
87. Chan, J., Xing, Y., Magliozzo, R.S., and Bloom, B.R. (1992). Killing of virulent Mycobacterium tuberculosis by reactive nitrogen intermediates produced by activated murine macrophages. J Exp Med *175*, 1111-1122. 10.1084/jem.175.4.1111.
88. Jianjun Yang, Zhang, R., Lu, G., Shen, Y., Peng, L., Zhu, C., Cui, M., Wang, W., Arnaboldi, P., Tang, M., et al. (2013). T cell–derived inducible nitric oxide synthase switches off Th17 cell differentiation. J Exp Med *210*, 1447-1462. 10.1084/jem.20122494.
89. Braverman, J., and Stanley, S.A. (2017). Nitric Oxide Modulates Macrophage Responses to. J Immunol *199*, 1805-1816. 10.4049/jimmunol.1700515.
90. Giordano, D., Li, C., Suthar, M.S., Draves, K.E., Ma, D.Y., Gale, M., and Clark, E.A. (2011). Nitric oxide controls an inflammatory-like Ly6C(hi)PDCA1+ DC subset that regulates Th1 immune responses. J Leukoc Biol *89*, 443-455. 10.1189/jlb.0610329.
91. Lukacs-Kornek, V., Malhotra, D., Fletcher, A.L., Acton, S.E., Elpek, K.G., Tayalia, P., Collier, A.R., and Turley, S.J. (2011). Regulated release of nitric oxide by nonhematopoietic stroma controls expansion of the activated T cell pool in lymph nodes. Nat Immunol *12*, 1096-1104. 10.1038/ni.2112.

92. Mazzoni, A., Bronte, V., Visintin, A., Spitzer, J.H., Apolloni, E., Serafini, P., Zanovello, P., and Segal, D.M. (2002). Myeloid suppressor lines inhibit T cell responses by an NO-dependent mechanism. J Immunol *168*, 689-695. 10.4049/jimmunol.168.2.689.
93. Peddireddy, V., Doddam, S.N., and Ahmed, N. (2017). Mycobacterial Dormancy Systems and Host Responses in Tuberculosis. Front Immunol *8*, 84. 10.3389/fimmu.2017.00084.
94. Leistikow, R.L., Morton, R.A., Bartek, I.L., Frimpong, I., Wagner, K., and Voskuil, M.I. (2010). The Mycobacterium tuberculosis DosR regulon assists in metabolic homeostasis and enables rapid recovery from nonrespiring dormancy. J Bacteriol *192*, 1662-1670. 10.1128/JB.00926-09.
95. Park, H.D., Guinn, K.M., Harrell, M.I., Liao, R., Voskuil, M.I., Tompa, M., Schoolnik, G.K., and Sherman, D.R. (2003). Rv3133c/dosR is a transcription factor that mediates the hypoxic response of Mycobacterium tuberculosis. Mol Microbiol *48*, 833-843. 10.1046/j.1365-2958.2003.03474.x.
96. Voskuil, M.I., Schnappinger, D., Visconti, K.C., Harrell, M.I., Dolganov, G.M., Sherman, D.R., and Schoolnik, G.K. (2003). Inhibition of respiration by nitric oxide induces a Mycobacterium tuberculosis dormancy program. J Exp Med *198*, 705-713. 10.1084/jem.20030205.
97. Allie, N., Grivennikov, S.I., Keeton, R., Hsu, N.J., Bourigault, M.L., Court, N., Fremond, C., Yeremeev, V., Shebzukhov, Y., Ryffel, B., et al. (2013). Prominent role for T cell-derived tumour necrosis factor for sustained control of Mycobacterium tuberculosis infection. Sci Rep *3*, 1809. 10.1038/srep01809.
98. Lindenstrøm, T., Knudsen, N.P., Agger, E.M., and Andersen, P. (2013). Control of chronic mycobacterium tuberculosis infection by CD4 KLRG1- IL-2-secreting central memory cells. J Immunol *190*, 6311-6319. 10.4049/jimmunol.1300248.
99. Rothchild, A.C., Stowell, B., Goyal, G., Nunes-Alves, C., Yang, Q., Papavinasasundaram, K., Sassetti, C.M., Dranoff, G., Chen, X., Lee, J., and Behar, S.M. (2017). Role of Granulocyte-Macrophage Colony-Stimulating Factor Production by T Cells during. mBio *8*. 10.1128/mBio.01514-17.
100. Rothchild, A.C., Jayaraman, P., Nunes-Alves, C., and Behar, S.M. (2014). iNKT cell production of GM-CSF controls Mycobacterium tuberculosis. PLoS Pathog *10*, e1003805. 10.1371/journal.ppat.1003805.
101. Sia, J.K., Bizzell, E., Madan-Lala, R., and Rengarajan, J. (2017). Engaging the CD40-CD40L pathway augments T-helper cell responses and improves control of Mycobacterium tuberculosis infection. PLoS Pathog *13*, e1006530. 10.1371/journal.ppat.1006530.
102. Khader, S.A., Bell, G.K., Pearl, J.E., Fountain, J.J., Rangel-Moreno, J., Cilley, G.E., Shen, F., Eaton, S.M., Gaffen, S.L., Swain, S.L., et al. (2007). IL-23 and IL-17 in the establishment of protective pulmonary CD4+ T cell responses after vaccination and during Mycobacterium tuberculosis challenge. Nat Immunol *8*, 369-377. 10.1038/ni1449.
103. Bunjun, R., Omondi, F.M.A., Makatsa, M.S., Keeton, R., Wendoh, J.M., Müller, T.L., Prentice, C.S.L., Wilkinson, R.J., Riou, C., and Burgers, W.A. (2021). Th22 Cells Are a

Major Contributor to the Mycobacterial CD4. J Immunol *207*, 1239-1249. 10.4049/jimmunol.1900984.

104. Shafiani, S., Dinh, C., Ertelt, J.M., Moguche, A.O., Siddiqui, I., Smigiel, K.S., Sharma, P., Campbell, D.J., Way, S.S., and Urdahl, K.B. (2013). Pathogen-specific Treg cells expand early during mycobacterium tuberculosis infection but are later eliminated in response to Interleukin-12. Immunity *38*, 1261-1270. 10.1016/j.immuni.2013.06.003.
105. Amezcua Vesely, M.C., Pallis, P., Bielecki, P., Low, J.S., Zhao, J., Harman, C.C.D., Kroehling, L., Jackson, R., Bailis, W., Licona-Limón, P., et al. (2019). Effector T. Cell *178*, 1176-1188.e1115. 10.1016/j.cell.2019.07.032.
106. Ogongo, P., Tran, A., Marzan, F., Gingrich, D., Krone, M., Aweeka, F., Lindestam Arlehamn, C.S., Martin, J.N., Deeks, S.G., Hunt, P.W., and Ernst, J.D. (2024). High-parameter phenotypic characterization reveals a subset of human Th17 cells that preferentially produce IL-17 against. Front Immunol *15*, 1378040. 10.3389/fimmu.2024.1378040.
107. Okamoto Yoshida, Y., Umemura, M., Yahagi, A., O'Brien, R.L., Ikuta, K., Kishihara, K., Hara, H., Nakae, S., Iwakura, Y., and Matsuzaki, G. (2010). Essential role of IL-17A in the formation of a mycobacterial infection-induced granuloma in the lung. J Immunol *184*, 4414-4422. 10.4049/jimmunol.0903332.
108. Jong, R.M., Van Dis, E., Berry, S.B., Nguyenla, X., Baltodano, A., Pastenkos, G., Xu, C., Fox, D., Yosef, N., McWhirter, S.M., and Stanley, S.A. (2022). Mucosal Vaccination with Cyclic Dinucleotide Adjuvants Induces Effective T Cell Homing and IL-17-Dependent Protection against. J Immunol *208*, 407-419. 10.4049/jimmunol.2100029.
109. Knudsen, N.P., Olsen, A., Buonsanti, C., Follmann, F., Zhang, Y., Coler, R.N., Fox, C.B., Meinke, A., D'Oro, U., Casini, D., et al. (2016). Different human vaccine adjuvants promote distinct antigen-independent immunological signatures tailored to different pathogens. Sci Rep *6*, 19570. 10.1038/srep19570.
110. Weaver, C.T., Elson, C.O., Fouser, L.A., and Kolls, J.K. (2013). The Th17 pathway and inflammatory diseases of the intestines, lungs, and skin. Annu Rev Pathol *8*, 477-512. 10.1146/annurev-pathol-011110-130318.
111. Kozakiewicz, L., Chen, Y., Xu, J., Wang, Y., Dunussi-Joannopoulos, K., Ou, Q., Flynn, J.L., Porcelli, S.A., Jacobs, W.R., and Chan, J. (2013). B cells regulate neutrophilia during Mycobacterium tuberculosis infection and BCG vaccination by modulating the interleukin-17 response. PLoS Pathog *9*, e1003472. 10.1371/journal.ppat.1003472.
112. Makatsa, M.S., Omondi, F.M.A., Bunjun, R., Wilkinson, R.J., Riou, C., and Burgers, W.A. (2022). Characterization of. J Immunol *209*, 446-455. 10.4049/jimmunol.2200140.
113. Matthews, K., Wilkinson, K.A., Kalsdorf, B., Roberts, T., Diacon, A., Walzl, G., Wolske, J., Ntsekhe, M., Syed, F., Russell, J., et al. (2011). Predominance of interleukin-22 over interleukin-17 at the site of disease in human tuberculosis. Tuberculosis (Edinb) *91*, 587-593. 10.1016/j.tube.2011.06.009.

114. Dhiman, R., Venkatasubramanian, S., Paidipally, P., Barnes, P.F., Tvinnereim, A., and Vankayalapati, R. (2014). Interleukin 22 inhibits intracellular growth of Mycobacterium tuberculosis by enhancing calgranulin A expression. J Infect Dis *209*, 578-587. 10.1093/infdis/jit495.
115. Treerat, P., Prince, O., Cruz-Lagunas, A., Muñoz-Torrico, M., Salazar-Lezama, M.A., Selman, M., Fallert-Junecko, B., Reinhardt, T.A., Alcorn, J.F., Kaushal, D., et al. (2017). Novel role for IL-22 in protection during chronic Mycobacterium tuberculosis HN878 infection. Mucosal Immunol *10*, 1069-1081. 10.1038/mi.2017.15.
116. Guyot-Revol, V., Innes, J.A., Hackforth, S., Hinks, T., and Lalvani, A. (2006). Regulatory T cells are expanded in blood and disease sites in patients with tuberculosis. Am J Respir Crit Care Med *173*, 803-810. 10.1164/rccm.200508-1294OC.
117. Gallegos, A.M., Pamer, E.G., and Glickman, M.S. (2008). Delayed protection by ESAT-6-specific effector CD4+ T cells after airborne M. tuberculosis infection. J Exp Med *205*, 2359-2368. 10.1084/jem.20080353.
118. Wolf, A.J., Desvignes, L., Linas, B., Banaiee, N., Tamura, T., Takatsu, K., and Ernst, J.D. (2008). Initiation of the adaptive immune response to Mycobacterium tuberculosis depends on antigen production in the local lymph node, not the lungs. J Exp Med *205*, 105-115. 10.1084/jem.20071367.
119. Flory, C.M., Hubbard, R.D., and Collins, F.M. (1992). Effects of in vivo T lymphocyte subset depletion on mycobacterial infections in mice. J Leukoc Biol *51*, 225-229. 10.1002/jlb.51.3.225.
120. Lin, P.L., and Flynn, J.L. (2015). CD8 T cells and Mycobacterium tuberculosis infection. Semin Immunopathol *37*, 239-249. 10.1007/s00281-015-0490-8.
121. Stenger, S., Hanson, D.A., Teitelbaum, R., Dewan, P., Niazi, K.R., Froelich, C.J., Ganz, T., Thoma-Uszynski, S., Melián, A., Bogdan, C., et al. (1998). An antimicrobial activity of cytolytic T cells mediated by granulysin. Science *282*, 121-125. 10.1126/science.282.5386.121.
122. Woodworth, J.S., Wu, Y., and Behar, S.M. (2008). Mycobacterium tuberculosis-specific CD8+ T cells require perforin to kill target cells and provide protection in vivo. J Immunol *181*, 8595-8603. 10.4049/jimmunol.181.12.8595.
123. Chandra, S., and Kronenberg, M. (2015). Activation and Function of iNKT and MAIT Cells. Adv Immunol *127*, 145-201. 10.1016/bs.ai.2015.03.003.
124. Ruibal, P., Voogd, L., Joosten, S.A., and Ottenhoff, T.H.M. (2021). The role of donor-unrestricted T-cells, innate lymphoid cells, and NK cells in anti-mycobacterial immunity. Immunol Rev *301*, 30-47. 10.1111/imr.12948.
125. Gold, M.C., Cerri, S., Smyk-Pearson, S., Cansler, M.E., Vogt, T.M., Delepine, J., Winata, E., Swarbrick, G.M., Chua, W.J., Yu, Y.Y., et al. (2010). Human mucosal associated invariant T cells detect bacterially infected cells. PLoS Biol *8*, e1000407. 10.1371/journal.pbio.1000407.
126. Vorkas, C.K., Wipperman, M.F., Li, K., Bean, J., Bhattarai, S.K., Adamow, M., Wong, P., Aubé, J., Juste, M.A.J., Bucci, V., et al. (2018). Mucosal-associated invariant and γδ T cell subsets respond to initial Mycobacterium tuberculosis infection. JCI Insight *3*. 10.1172/jci.insight.121899.

127. Sakai, S., Kauffman, K.D., Oh, S., Nelson, C.E., Barry, C.E., and Barber, D.L. (2021). MAIT cell-directed therapy of Mycobacterium tuberculosis infection. Mucosal Immunol *14*, 199-208. 10.1038/s41385-020-0332-4.
128. Dubois Cauwelaert, N., Baldwin, S.L., Orr, M.T., Desbien, A.L., Gage, E., Hofmeyer, K.A., and Coler, R.N. (2016). Antigen presentation by B cells guides programing of memory CD4. Eur J Immunol *46*, 2719-2729. 10.1002/eji.201646399.
129. Linge, I., Dyatlov, A., Kondratieva, E., Avdienko, V., Apt, A., and Kondratieva, T. (2017). B-lymphocytes forming follicle-like structures in the lung tissue of tuberculosis-infected mice: Dynamics, phenotypes and functional activity. Tuberculosis (Edinb) *102*, 16-23. 10.1016/j.tube.2016.11.005.
130. Armstrong, J.A., and Hart, P.D. (1975). Phagosome-lysosome interactions in cultured macrophages infected with virulent tubercle bacilli. Reversal of the usual nonfusion pattern and observations on bacterial survival. J Exp Med *142*, 1-16. 10.1084/jem.142.1.1.
131. Abebe, F., and Bjune, G. (2009). The protective role of antibody responses during Mycobacterium tuberculosis infection. Clin Exp Immunol *157*, 235-243. 10.1111/j.1365-2249.2009.03967.x.
132. Rijnink, W.F., Ottenhoff, T.H.M., and Joosten, S.A. (2021). B-Cells and Antibodies as Contributors to Effector Immune Responses in Tuberculosis. Front Immunol *12*, 640168. 10.3389/fimmu.2021.640168.
133. Grace, P.S., Peters, J.M., Sixsmith, J., Lu, R., Irvine, E.B., Luedeman, C., Fenderson, B.A., Vickers, A., Slein, M.D., McKitrick, T., et al. (2025). Antibody-Fab and -Fc features promote Mycobacterium tuberculosis restriction. Immunity *58*, 1586-1597.e1585. 10.1016/j.immuni.2025.05.004.
134. Johnson, C.M., Cooper, A.M., Frank, A.A., Bonorino, C.B., Wysoki, L.J., and Orme, I.M. (1997). Mycobacterium tuberculosis aerogenic rechallenge infections in B cell-deficient mice. Tuber Lung Dis *78*, 257-261. 10.1016/s0962-8479(97)90006-x.
135. Torrado, E., Fountain, J.J., Robinson, R.T., Martino, C.A., Pearl, J.E., Rangel-Moreno, J., Tighe, M., Dunn, R., and Cooper, A.M. (2013). Differential and site specific impact of B cells in the protective immune response to Mycobacterium tuberculosis in the mouse. PLoS One *8*, e61681. 10.1371/journal.pone.0061681.
136. Phuah, J., Wong, E.A., Gideon, H.P., Maiello, P., Coleman, M.T., Hendricks, M.R., Ruden, R., Cirrincione, L.R., Chan, J., Lin, P.L., and Flynn, J.L. (2016). Effects of B Cell Depletion on Early Mycobacterium tuberculosis Infection in Cynomolgus Macaques. Infect Immun *84*, 1301-1311. 10.1128/IAI.00083-16.
137. Liao, T.L., Lin, C.H., Chen, Y.M., Chang, C.L., Chen, H.H., and Chen, D.Y. (2016). Different Risk of Tuberculosis and Efficacy of Isoniazid Prophylaxis in Rheumatoid Arthritis Patients with Biologic Therapy: A Nationwide Retrospective Cohort Study in Taiwan. PLoS One *11*, e0153217. 10.1371/journal.pone.0153217.
138. Schmidt, A.C., Fairlie, L., Hellström, E., Luabeya Kany Kany, A., Middelkoop, K., Naidoo, K., Nair, G., Gela, A., Nemes, E., Scriba, T.J., et al. (2025). BCG Revaccination for the Prevention of. N Engl J Med *392*, 1789-1800. 10.1056/NEJMoa2412381.

139. Kaufmann, E., Sanz, J., Dunn, J.L., Khan, N., Mendonça, L.E., Pacis, A., Tzelepis, F., Pernet, E., Dumaine, A., Grenier, J.C., et al. (2018). BCG Educates Hematopoietic Stem Cells to Generate Protective Innate Immunity against Tuberculosis. Cell *172*, 176-190.e119. 10.1016/j.cell.2017.12.031.
140. Delahaye, J.L., Gern, B.H., Cohen, S.B., Plumlee, C.R., Shafiani, S., Gerner, M.Y., and Urdahl, K.B. (2019). Cutting Edge: Bacillus Calmette-Guérin-Induced T Cells Shape. J Immunol *203*, 807-812. 10.4049/jimmunol.1900108.
141. Derrick, S.C., Yabe, I.M., Yang, A., and Morris, S.L. (2011). Vaccine-induced anti-tuberculosis protective immunity in mice correlates with the magnitude and quality of multifunctional CD4 T cells. Vaccine *29*, 2902-2909. 10.1016/j.vaccine.2011.02.010.
142. Kar, U.K., and Joosten, L.A.B. (2020). Training the trainable cells of the immune system and beyond. Nat Immunol *21*, 115-119. 10.1038/s41590-019-0583-y.
143. Luabeya, A.K.K., Rozot, V., Imbratta, C., Ratangee, F., Shenje, J., Tameris, M., Mendelsohn, S.C., Geldenhuys, H., Fisher, M., Musvosvi, M., et al. (2025). Live-attenuated Mycobacterium tuberculosis vaccine, MTBVAC, in adults with or without M tuberculosis sensitisation: a single-centre, phase 1b-2a, double-blind, dose-escalation, randomised controlled trial. Lancet Glob Health *13*, e1030-e1042. 10.1016/S2214-109X(25)00046-4.
144. Tameris, M., Mearns, H., Penn-Nicholson, A., Gregg, Y., Bilek, N., Mabwe, S., Geldenhuys, H., Shenje, J., Luabeya, A.K.K., Murillo, I., et al. (2019). Live-attenuated Mycobacterium tuberculosis vaccine MTBVAC versus BCG in adults and neonates: a randomised controlled, double-blind dose-escalation trial. Lancet Respir Med *7*, 757-770. 10.1016/S2213-2600(19)30251-6.
145. Gong, W., and Du, J. (2024). Optimising the vaccine strategy of BCG, ChAdOx1 85A, and MVA85A for tuberculosis control. Lancet Infect Dis *24*, 224-226. 10.1016/S1473-3099(23)00514-5.
146. Hildner, K., Edelson, B.T., Purtha, W.E., Diamond, M., Matsushita, H., Kohyama, M., Calderon, B., Schraml, B.U., Unanue, E.R., Diamond, M.S., et al. (2008). Batf3 deficiency reveals a critical role for CD8alpha+ dendritic cells in cytotoxic T cell immunity. Science *322*, 1097-1100. 10.1126/science.1164206.
147. Nagai, T., Ibata, K., Park, E.S., Kubota, M., Mikoshiba, K., and Miyawaki, A. (2002). A variant of yellow fluorescent protein with fast and efficient maturation for cell-biological applications. Nat Biotechnol *20*, 87-90. 10.1038/nbt0102-87.
148. Yamazaki, C., Sugiyama, M., Ohta, T., Hemmi, H., Hamada, E., Sasaki, I., Fukuda, Y., Yano, T., Nobuoka, M., Hirashima, T., et al. (2013). Critical roles of a dendritic cell subset expressing a chemokine receptor, XCR1. J Immunol *190*, 6071-6082. 10.4049/jimmunol.1202798.
149. Satpathy, A.T., KC, W., Albring, J.C., Edelson, B.T., Kretzer, N.M., Bhattacharya, D., Murphy, T.L., and Murphy, K.M. (2012). Zbtb46 expression distinguishes classical dendritic cells and their committed progenitors from other immune lineages. J Exp Med *209*, 1135-1152. 10.1084/jem.20120030.
150. Tamura, T., Ariga, H., Kinashi, T., Uehara, S., Kikuchi, T., Nakada, M., Tokunaga, T., Xu, W., Kariyone, A., Saito, T., et al. (2004). The role of antigenic peptide in CD4+ T

helper phenotype development in a T cell receptor transgenic model. Int Immunol *16*, 1691-1699. 10.1093/intimm/dxh170.

151. Cosma, C.L., Humbert, O., and Ramakrishnan, L. (2004). Superinfecting mycobacteria home to established tuberculous granulomas. Nat Immunol *5*, 828-835. 10.1038/ni1091.
152. Palanisamy, G.S., DuTeau, N., Eisenach, K.D., Cave, D.M., Theus, S.A., Kreiswirth, B.N., Basaraba, R.J., and Orme, I.M. (2009). Clinical strains of Mycobacterium tuberculosis display a wide range of virulence in guinea pigs. Tuberculosis (Edinb) *89*, 203-209. 10.1016/j.tube.2009.01.005.
153. Urdahl, K.B., Liggitt, D., and Bevan, M.J. (2003). CD8+ T cells accumulate in the lungs of Mycobacterium tuberculosis-infected Kb-/-Db-/- mice, but provide minimal protection. J Immunol *170*, 1987-1994. 10.4049/jimmunol.170.4.1987.
154. Leal, J.M., Huang, J.Y., Kohli, K., Stoltzfus, C., Lyons-Cohen, M.R., Olin, B.E., Gale, M., and Gerner, M.Y. (2021). Innate cell microenvironments in lymph nodes shape the generation of T cell responses during type I inflammation. Sci Immunol *6*. 10.1126/sciimmunol.abb9435.
155. Butler, A., Hoffman, P., Smibert, P., Papalexi, E., and Satija, R. (2018). Integrating single-cell transcriptomic data across different conditions, technologies, and species. Nat Biotechnol *36*, 411-420. 10.1038/nbt.4096.
156. Hafemeister, C., and Satija, R. (2019). Normalization and variance stabilization of single-cell RNA-seq data using regularized negative binomial regression. Genome Biol *20*, 296. 10.1186/s13059-019-1874-1.
157. Aran, D., Looney, A.P., Liu, L., Wu, E., Fong, V., Hsu, A., Chak, S., Naikawadi, R.P., Wolters, P.J., Abate, A.R., et al. (2019). Reference-based analysis of lung single-cell sequencing reveals a transitional profibrotic macrophage. Nat Immunol *20*, 163-172. 10.1038/s41590-018-0276-y.
158. Miller, J.C., Brown, B.D., Shay, T., Gautier, E.L., Jojic, V., Cohain, A., Pandey, G., Leboeuf, M., Elpek, K.G., Helft, J., et al. (2012). Deciphering the transcriptional network of the dendritic cell lineage. Nat Immunol *13*, 888-899. 10.1038/ni.2370.
159. Fu, R., Gillen, A.E., Sheridan, R.M., Tian, C., Daya, M., Hao, Y., Hesselberth, J.R., and Riemondy, K.A. (2020). clustifyr: an R package for automated single-cell RNA sequencing cluster classification. F1000Res *9*, 223. 10.12688/f1000research.22969.2.
160. Sayols, S. (2023). rrvgo: a Bioconductor package for interpreting lists of Gene Ontology terms. MicroPubl Biol *2023*. 10.17912/micropub.biology.000811.
161. Street, K., Risso, D., Fletcher, R.B., Das, D., Ngai, J., Yosef, N., Purdom, E., and Dudoit, S. (2018). Slingshot: cell lineage and pseudotime inference for single-cell transcriptomics. BMC Genomics *19*, 477. 10.1186/s12864-018-4772-0.
162. Lyons-Cohen, M.R., Shamskhou, E.A., and Gerner, M.Y. (2024). Site-specific regulation of Th2 differentiation within lymph node microenvironments. J Exp Med *221*. 10.1084/jem.20231282.
163. Taverna, F., Goveia, J., Karakach, T.K., Khan, S., Rohlenova, K., Treps, L., Subramanian, A., Schoonjans, L., Dewerchin, M., Eelen, G., and Carmeliet, P.

(2020). BIOMEX: an interactive workflow for (single cell) omics data interpretation and visualization. Nucleic Acids Res *48*, W385-W394. 10.1093/nar/gkaa332.

164. O'Connell, K.E., Mikkola, A.M., Stepanek, A.M., Vernet, A., Hall, C.D., Sun, C.C., Yildirim, E., Staropoli, J.F., Lee, J.T., and Brown, D.E. (2015). Practical murine hematopathology: a comparative review and implications for research. Comp Med *65*, 96-113.
165. Sakai, S., Mayer-Barber, K.D., and Barber, D.L. (2014). Defining features of protective CD4 T cell responses to Mycobacterium tuberculosis. Curr Opin Immunol *29*, 137-142. 10.1016/j.coi.2014.06.003.
166. Le, D., Miller, J.D., and Ganusov, V.V. (2014). Mathematical modeling provides kinetic details of the human immune response to vaccination. Front Cell Infect Microbiol *4*, 177. 10.3389/fcimb.2014.00177.
167. (!!! INVALID CITATION !!!).
168. McDaniel, M.M., Krishna, N., Handagama, W.G., Eda, S., and Ganusov, V.V. (2016). Quantifying Limits on Replication, Death, and Quiescence of Mycobacterium tuberculosis in Mice. Front Microbiol *7*, 862. 10.3389/fmicb.2016.00862.
169. Urdahl, K.B., Shafiani, S., and Ernst, J.D. (2011). Initiation and regulation of T-cell responses in tuberculosis. Mucosal Immunol *4*, 288-293. 10.1038/mi.2011.10.
170. Balasubramanian, V., Wiegeshaus, E.H., Taylor, B.T., and Smith, D.W. (1994). Pathogenesis of tuberculosis: pathway to apical localization. Tuber Lung Dis *75*, 168-178. 10.1016/0962-8479(94)90002-7.
171. Ganchua, S.K.C., Cadena, A.M., Maiello, P., Gideon, H.P., Myers, A.J., Junecko, B.F., Klein, E.C., Lin, P.L., Mattila, J.T., and Flynn, J.L. (2018). Lymph nodes are sites of prolonged bacterial persistence during Mycobacterium tuberculosis infection in macaques. PLoS Pathog *14*, e1007337. 10.1371/journal.ppat.1007337.
172. Becker, S.H., Ronayne, C.E., Bold, T.D., and Jenkins, M.K. (2025). Antigen-specific CD4+ T cells promote monocyte recruitment and differentiation into glycolytic lung macrophages to control Mycobacterium tuberculosis. PLoS Pathog *21*, e1013208. 10.1371/journal.ppat.1013208.
173. Nakano, H., Lyons-Cohen, M.R., Whitehead, G.S., Nakano, K., and Cook, D.N. (2017). Distinct functions of CXCR4, CCR2, and CX3CR1 direct dendritic cell precursors from the bone marrow to the lung. J Leukoc Biol *101*, 1143-1153. 10.1189/jlb.1A0616-285R.
174. Cabeza-Cabrerizo, M., Minutti, C.M., da Costa, M.P., Cardoso, A., Jenkins, R.P., Kulikauskaite, J., Buck, M.D., Piot, C., Rogers, N., Crotta, S., et al. (2021). Recruitment of dendritic cell progenitors to foci of influenza A virus infection sustains immunity. Sci Immunol *6*, eabi9331. 10.1126/sciimmunol.abi9331.
175. Bosteels, C., Neyt, K., Vanheerswynghels, M., van Helden, M.J., Sichien, D., Debeuf, N., De Prijck, S., Bosteels, V., Vandamme, N., Martens, L., et al. (2020). Inflammatory Type 2 cDCs Acquire Features of cDC1s and Macrophages to Orchestrate Immunity to Respiratory Virus Infection. Immunity *52*, 1039-1056.e1039. 10.1016/j.immuni.2020.04.005.

176. Sun, X., Chao, J.L., Gerner, M., and Elkon, K.B. (2025). Induction of Type I Interferon-Dependent Activation and Migration of Inflammatory Dendritic Cells to Local Lymph Nodes by UV Light Exposure. Arthritis Rheumatol *77*, 867-875. 10.1002/art.43108.
177. Moguche, A.O., Shafiani, S., Clemons, C., Larson, R.P., Dinh, C., Higdon, L.E., Cambier, C.J., Sissons, J.R., Gallegos, A.M., Fink, P.J., and Urdahl, K.B. (2015). ICOS and Bcl6-dependent pathways maintain a CD4 T cell population with memory-like properties during tuberculosis. J Exp Med *212*, 715-728. 10.1084/jem.20141518.
178. Sakai, S., Kauffman, K.D., Schenkel, J.M., McBerry, C.C., Mayer-Barber, K.D., Masopust, D., and Barber, D.L. (2014). Cutting edge: control of Mycobacterium tuberculosis infection by a subset of lung parenchyma-homing CD4 T cells. J Immunol *192*, 2965-2969. 10.4049/jimmunol.1400019.
179. Sallin, M.A., Sakai, S., Kauffman, K.D., Young, H.A., Zhu, J., and Barber, D.L. (2017). Th1 Differentiation Drives the Accumulation of Intravascular, Non-protective CD4 T Cells during Tuberculosis. Cell Rep *18*, 3091-3104. 10.1016/j.celrep.2017.03.007.
180. Moguche, A.O., Musvosvi, M., Penn-Nicholson, A., Plumlee, C.R., Mearns, H., Geldenhuys, H., Smit, E., Abrahams, D., Rozot, V., Dintwe, O., et al. (2017). Antigen Availability Shapes T Cell Differentiation and Function during Tuberculosis. Cell Host Microbe *21*, 695-706.e695. 10.1016/j.chom.2017.05.012.
181. Torrado, E., Fountain, J.J., Liao, M., Tighe, M., Reiley, W.W., Lai, R.P., Meintjes, G., Pearl, J.E., Chen, X., Zak, D.E., et al. (2015). Interleukin 27R regulates CD4+ T cell phenotype and impacts protective immunity during Mycobacterium tuberculosis infection. J Exp Med *212*, 1449-1463. 10.1084/jem.20141520.
182. Cabeza-Cabrerizo, M., Cardoso, A., Minutti, C.M., Pereira da Costa, M., and Reis e Sousa, C. (2021). Dendritic Cells Revisited. Annu Rev Immunol *39*, 131-166. 10.1146/annurev-immunol-061020-053707.
183. Catron, D.M., Itano, A.A., Pape, K.A., Mueller, D.L., and Jenkins, M.K. (2004). Visualizing the first 50 hr of the primary immune response to a soluble antigen. Immunity *21*, 341-347. 10.1016/j.immuni.2004.08.007.
184. Plumlee, C.R., Barrett, H.W., Shao, D.E., Lien, K.A., Cross, L.M., Cohen, S.B., Edlefsen, P.T., and Urdahl, K.B. (2023). Assessing vaccine-mediated protection in an ultra-low dose Mycobacterium tuberculosis murine model. PLoS Pathog *19*, e1011825. 10.1371/journal.ppat.1011825.
185. Mangtani, P., Abubakar, I., Ariti, C., Beynon, R., Pimpin, L., Fine, P.E., Rodrigues, L.C., Smith, P.G., Lipman, M., Whiting, P.F., and Sterne, J.A. (2014). Protection by BCG vaccine against tuberculosis: a systematic review of randomized controlled trials. Clin Infect Dis *58*, 470-480. 10.1093/cid/cit790.
186. Guilliams, M., Dutertre, C.A., Scott, C.L., McGovern, N., Sichien, D., Chakarov, S., Van Gassen, S., Chen, J., Poidinger, M., De Prijck, S., et al. (2016). Unsupervised High-Dimensional Analysis Aligns Dendritic Cells across Tissues and Species. Immunity *45*, 669-684. 10.1016/j.immuni.2016.08.015.
187. Driver, E.R., Ryan, G.J., Hoff, D.R., Irwin, S.M., Basaraba, R.J., Kramnik, I., and Lenaerts, A.J. (2012). Evaluation of a mouse model of necrotic granuloma formation using C3HeB/FeJ mice for testing of drugs against Mycobacterium tuberculosis. Antimicrob Agents Chemother *56*, 3181-3195. 10.1128/AAC.00217-12.

188. Bohlson, S.S., O'Conner, S.D., Hulsebus, H.J., Ho, M.M., and Fraser, D.A. (2014). Complement, c1q, and c1q-related molecules regulate macrophage polarization. Front Immunol *5*, 402. 10.3389/fimmu.2014.00402.
189. Pisu, D., Johnston, L., Mattila, J.T., and Russell, D.G. (2024). The frequency of CD38. Nat Commun *15*, 8522. 10.1038/s41467-024-52846-w.
190. Pisu, D., Huang, L., Narang, V., Theriault, M., Lê-Bury, G., Lee, B., Lakudzala, A.E., Mzinza, D.T., Mhango, D.V., Mitini-Nkhoma, S.C., et al. (2021). Single cell analysis of M. tuberculosis phenotype and macrophage lineages in the infected lung. J Exp Med *218*. 10.1084/jem.20210615.
191. Lubbers, R., Sutherland, J.S., Goletti, D., de Paus, R.A., van Moorsel, C.H.M., Veltkamp, M., Vestjens, S.M.T., Bos, W.J.W., Petrone, L., Del Nonno, F., et al. (2018). Complement Component C1q as Serum Biomarker to Detect Active Tuberculosis. Front Immunol *9*, 2427. 10.3389/fimmu.2018.02427.
192. Ugur, M., Labios, R.J., Fenton, C., Knöpper, K., Jobin, K., Imdahl, F., Golda, G., Hoh, K., Grafen, A., Kaisho, T., et al. (2023). Lymph node medulla regulates the spatiotemporal unfolding of resident dendritic cell networks. Immunity *56*, 1778-1793.e1710. 10.1016/j.immuni.2023.06.020.
193. Haldar, M., Kohyama, M., So, A.Y., Kc, W., Wu, X., Briseño, C.G., Satpathy, A.T., Kretzer, N.M., Arase, H., Rajasekaran, N.S., et al. (2014). Heme-mediated SPI-C induction promotes monocyte differentiation into iron-recycling macrophages. Cell *156*, 1223-1234. 10.1016/j.cell.2014.01.069.
194. Murray, P.J., and Wynn, T.A. (2011). Protective and pathogenic functions of macrophage subsets. Nat Rev Immunol *11*, 723-737. 10.1038/nri3073.
195. Schyns, J., Bai, Q., Ruscitti, C., Radermecker, C., De Schepper, S., Chakarov, S., Farnir, F., Pirottin, D., Ginhoux, F., Boeckxstaens, G., et al. (2019). Non-classical tissue monocytes and two functionally distinct populations of interstitial macrophages populate the mouse lung. Nat Commun *10*, 3964. 10.1038/s41467-019-11843-0.
196. Vrieling, F., Kostidis, S., Spaink, H.P., Haks, M.C., Mayboroda, O.A., Ottenhoff, T.H.M., and Joosten, S.A. (2020). Analyzing the impact of Mycobacterium tuberculosis infection on primary human macrophages by combined exploratory and targeted metabolomics. Sci Rep *10*, 7085. 10.1038/s41598-020-62911-1.
197. Jianjun Yang, Zhang, R., Lu, G., Shen, Y., Peng, L., Zhu, C., Cui, M., Wang, W., Arnaboldi, P., Tang, M., et al. (2013). T cell–derived inducible nitric oxide synthase switches off Th17 cell differentiation. J Exp Med *210*, 1447-1462. 10.1084/jem.20122494.
198. Pearl, J.E., Saunders, B., Ehlers, S., Orme, I.M., and Cooper, A.M. (2001). Inflammation and lymphocyte activation during mycobacterial infection in the interferon-gamma-deficient mouse. Cell Immunol *211*, 43-50. 10.1006/cimm.2001.1819.
199. Vermaelen, K.Y., Carro-Muino, I., Lambrecht, B.N., and Pauwels, R.A. (2001). Specific migratory dendritic cells rapidly transport antigen from the airways to the thoracic lymph nodes. J Exp Med *193*, 51-60. 10.1084/jem.193.1.51.

200. Hagan, N.B., Inaku, C., Kunder, N., White, T., Iraguha, T., Meyer, A., Pauken, K.E., and Schenkel, J.M. (2025). In vivo antibody labeling route and fluorophore dictate labeling efficiency, sensitivity, and longevity. J Immunol *214*, 828-838. 10.1093/jimmun/vkae051.
201. Shanahan, S.L., Kunder, N., Inaku, C., Hagan, N.B., Gibbons, G., Mathey-Andrews, N., Anandappa, G., Soares, S., Pauken, K.E., Jacks, T., and Schenkel, J.M. (2024). Longitudinal Intravascular Antibody Labeling Identified Regulatory T Cell Recruitment as a Therapeutic Target in a Mouse Model of Lung Cancer. J Immunol *213*, 906-918. 10.4049/jimmunol.2400268.
202. Mortlock, R.D., Wu, C., Potter, E.L., Abraham, D.M., Allan, D.S.J., Hong, S.G., Roederer, M., and Dunbar, C.E. (2021). Tissue Trafficking Kinetics of Rhesus Macaque Natural Killer Cells Measured by Serial Intravascular Staining. Front Immunol *12*, 772332. 10.3389/fimmu.2021.772332.
203. Salmond, R.J., Emery, J., Okkenhaug, K., and Zamoyska, R. (2009). MAPK, phosphatidylinositol 3-kinase, and mammalian target of rapamycin pathways converge at the level of ribosomal protein S6 phosphorylation to control metabolic signaling in CD8 T cells. J Immunol *183*, 7388-7397. 10.4049/jimmunol.0902294.
204. Gern, B.H., Adams, K.N., Plumlee, C.R., Stoltzfus, C.R., Shehata, L., Moguche, A.O., Busman-Sahay, K., Hansen, S.G., Axthelm, M.K., Picker, L.J., et al. (2021). TGFβ restricts expansion, survival, and function of T cells within the tuberculous granuloma. Cell Host Microbe *29*, 594-606.e596. 10.1016/j.chom.2021.02.005.
205. Pepper, M., Pagán, A.J., Igyártó, B.Z., Taylor, J.J., and Jenkins, M.K. (2011). Opposing signals from the Bcl6 transcription factor and the interleukin-2 receptor generate T helper 1 central and effector memory cells. Immunity *35*, 583-595. 10.1016/j.immuni.2011.09.009.
206. Daniel, L., Bhattacharyya, N.D., Counoupas, C., Cai, Y., Chen, X., Triccas, J.A., Britton, W.J., and Feng, C.G. (2022). Stromal structure remodeling by B lymphocytes limits T cell activation in lymph nodes of Mycobacterium tuberculosis-infected mice. J Clin Invest *132*. 10.1172/JCI157873.
207. Athie-Morales, V., Smits, H.H., Cantrell, D.A., and Hilkens, C.M. (2004). Sustained IL-12 signaling is required for Th1 development. J Immunol *172*, 61-69. 10.4049/jimmunol.172.1.61.
208. Rogge, L., Barberis-Maino, L., Biffi, M., Passini, N., Presky, D.H., Gubler, U., and Sinigaglia, F. (1997). Selective expression of an interleukin-12 receptor component by human T helper 1 cells. J Exp Med *185*, 825-831. 10.1084/jem.185.5.825.
209. Escobar, G., Mangani, D., and Anderson, A.C. (2020). T cell factor 1: A master regulator of the T cell response in disease. Sci Immunol *5*. 10.1126/sciimmunol.abb9726.
210. Izumi, G., Nakano, H., Nakano, K., Whitehead, G.S., Grimm, S.A., Fessler, M.B., Karmaus, P.W., and Cook, D.N. (2021). CD11b + lung dendritic cells at different stages of maturation induce Th17 or Th2 differentiation. Nat Commun *12*, 5029. 10.1038/s41467-021-25307-x.

211. Min, J., Yang, D., Kim, M., Haam, K., Yoo, A., Choi, J.H., Schraml, B.U., Kim, Y.S., Kim, D., and Kang, S.J. (2018). Inflammation induces two types of inflammatory dendritic cells in inflamed lymph nodes. Exp Mol Med *50*, e458. 10.1038/emm.2017.292.
212. Khan, N., Downey, J., Sanz, J., Kaufmann, E., Blankenhaus, B., Pacis, A., Pernet, E., Ahmed, E., Cardoso, S., Nijnik, A., et al. (2020). M. tuberculosis Reprograms Hematopoietic Stem Cells to Limit Myelopoiesis and Impair Trained Immunity. Cell *183*, 752-770.e722. 10.1016/j.cell.2020.09.062.
213. Behr, M.A., Wilson, M.A., Gill, W.P., Salamon, H., Schoolnik, G.K., Rane, S., and Small, P.M. (1999). Comparative genomics of BCG vaccines by whole-genome DNA microarray. Science *284*, 1520-1523. 10.1126/science.284.5419.1520.
214. Zheng, W., Limberis, J.D., Howard, Z.P., Mohapatra, A., Takagi, E., and Ernst, J.D. (2025). Impaired IFNγ responsiveness of monocyte-derived lung cells limits immunity to. bioRxiv. 10.1101/2025.10.06.680719.
215. Cruz, A.T., and Starke, J.R. (2007). Clinical manifestations of tuberculosis in children. Paediatr Respir Rev *8*, 107-117. 10.1016/j.prrv.2007.04.008.
216. Zhang, G., deWeerd, N.A., Stifter, S.A., Liu, L., Zhou, B., Wang, W., Zhou, Y., Ying, B., Hu, X., Matthews, A.Y., et al. (2018). A proline deletion in IFNAR1 impairs IFN-signaling and underlies increased resistance to tuberculosis in humans. Nat Commun *9*, 85. 10.1038/s41467-017-02611-z.
217. Branchett, W.J., Stavropoulos, E., Shields, J., Al-Dibouni, A., Cardoso, M., Fernandes, A.I., Moreira-Teixeira, L., Slawinski, H., Mikolajczak, A., Rodgers, A., et al. (2025). Type I IFN drives neutrophil swarming, impeding lung T cell-macrophage interactions and TB control. J Exp Med *222*. 10.1084/jem.20250466.
218. Moreira-Teixeira, L., Stimpson, P.J., Stavropoulos, E., Hadebe, S., Chakravarty, P., Ioannou, M., Aramburu, I.V., Herbert, E., Priestnall, S.L., Suarez-Bonnet, A., et al. (2020). Type I IFN exacerbates disease in tuberculosis-susceptible mice by inducing neutrophil-mediated lung inflammation and NETosis. Nat Commun *11*, 5566. 10.1038/s41467-020-19412-6.
219. Berry, M.P., Graham, C.M., McNab, F.W., Xu, Z., Bloch, S.A., Oni, T., Wilkinson, K.A., Banchereau, R., Skinner, J., Wilkinson, R.J., et al. (2010). An interferon-inducible neutrophil-driven blood transcriptional signature in human tuberculosis. Nature *466*, 973-977. 10.1038/nature09247.
220. Ji, D.X., Yamashiro, L.H., Chen, K.J., Mukaida, N., Kramnik, I., Darwin, K.H., and Vance, R.E. (2019). Type I interferon-driven susceptibility to Mycobacterium tuberculosis is mediated by IL-1Ra. Nat Microbiol *4*, 2128-2135. 10.1038/s41564-019-0578-3.
221. Nish, S.A., Zens, K.D., Kratchmarov, R., Lin, W.W., Adams, W.C., Chen, Y.H., Yen, B., Rothman, N.J., Bhandoola, A., Xue, H.H., et al. (2017). CD4+ T cell effector commitment coupled to self-renewal by asymmetric cell divisions. J Exp Med *214*, 39-47. 10.1084/jem.20161046.
222. Howard, N.C., and Khader, S.A. (2020). Immunometabolism during Mycobacterium tuberculosis Infection. Trends Microbiol *28*, 832-850. 10.1016/j.tim.2020.04.010.

223. Dang, B., Gao, Q., Zhang, L., Zhang, J., Cai, H., Zhu, Y., Zhong, Q., Liu, J., Niu, Y., Mao, K., et al. (2023). The glycolysis/HIF-1α axis defines the inflammatory role of IL-4-primed macrophages. Cell Rep *42*, 112471. 10.1016/j.celrep.2023.112471.
224. Egen, J.G., Rothfuchs, A.G., Feng, C.G., Horwitz, M.A., Sher, A., and Germain, R.N. (2011). Intravital imaging reveals limited antigen presentation and T cell effector function in mycobacterial granulomas. Immunity *34*, 807-819. 10.1016/j.immuni.2011.03.022.
225. Gehring, A.J., Rojas, R.E., Canaday, D.H., Lakey, D.L., Harding, C.V., and Boom, W.H. (2003). The Mycobacterium tuberculosis 19-kilodalton lipoprotein inhibits gamma interferon-regulated HLA-DR and Fc gamma R1 on human macrophages through Toll-like receptor 2. Infect Immun *71*, 4487-4497. 10.1128/IAI.71.8.4487-4497.2003.
226. Georgieva, M., Sia, J.K., Bizzell, E., Madan-Lala, R., and Rengarajan, J. (2018). Mycobacterium tuberculosis GroEL2 Modulates Dendritic Cell Responses. Infect Immun *86*. 10.1128/IAI.00387-17.
227. Mittal, E., Skowyra, M.L., Uwase, G., Tinaztepe, E., Mehra, A., Köster, S., Hanson, P.I., and Philips, J.A. (2018). Mycobacterium tuberculosis Type VII Secretion System Effectors Differentially Impact the ESCRT Endomembrane Damage Response. mBio *9*. 10.1128/mBio.01765-18.
228. Portal-Celhay, C., Tufariello, J.M., Srivastava, S., Zahra, A., Klevorn, T., Grace, P.S., Mehra, A., Park, H.S., Ernst, J.D., Jacobs, W.R., and Philips, J.A. (2016). Mycobacterium tuberculosis EsxH inhibits ESCRT-dependent CD4. Nat Microbiol *2*, 16232. 10.1038/nmicrobiol.2016.232.
229. Grace, P.S., and Ernst, J.D. (2016). Suboptimal Antigen Presentation Contributes to Virulence of Mycobacterium tuberculosis In Vivo. J Immunol *196*, 357-364. 10.4049/jimmunol.1501494.
230. McCaffrey, E.F., Donato, M., Keren, L., Chen, Z., Delmastro, A., Fitzpatrick, M.B., Gupta, S., Greenwald, N.F., Baranski, A., Graf, W., et al. (2022). The immunoregulatory landscape of human tuberculosis granulomas. Nat Immunol *23*, 318-329. 10.1038/s41590-021-01121-x.
231. Lewinsohn, D.M., Swarbrick, G.M., Cansler, M.E., Null, M.D., Rajaraman, V., Frieder, M.M., Sherman, D.R., McWeeney, S., and Lewinsohn, D.A. (2013). Human Mycobacterium tuberculosis CD8 T Cell Antigens/Epitopes Identified by a Proteomic Peptide Library. PLoS One *8*, e67016. 10.1371/journal.pone.0067016.
232. Lindestam Arlehamn, C.S., Gerasimova, A., Mele, F., Henderson, R., Swann, J., Greenbaum, J.A., Kim, Y., Sidney, J., James, E.A., Taplitz, R., et al. (2013). Memory T cells in latent Mycobacterium tuberculosis infection are directed against three antigenic islands and largely contained in a CXCR3+CCR6+ Th1 subset. PLoS Pathog *9*, e1003130. 10.1371/journal.ppat.1003130.
233. Lindestam Arlehamn, C.S., McKinney, D.M., Carpenter, C., Paul, S., Rozot, V., Makgotlho, E., Gregg, Y., van Rooyen, M., Ernst, J.D., Hatherill, M., et al. (2016). A Quantitative Analysis of Complexity of Human Pathogen-Specific CD4 T Cell Responses in Healthy M. tuberculosis Infected South Africans. PLoS Pathog *12*, e1005760. 10.1371/journal.ppat.1005760.

234. Scriba, T.J., Carpenter, C., Pro, S.C., Sidney, J., Musvosvi, M., Rozot, V., Seumois, G., Rosales, S.L., Vijayanand, P., Goletti, D., et al. (2017). Differential Recognition of Mycobacterium tuberculosis-Specific Epitopes as a Function of Tuberculosis Disease History. Am J Respir Crit Care Med *196*, 772-781. 10.1164/rccm.201706-1208OC.
235. Leddy, O., Ogongo, P., Huffaker, J., Gan, M., Milligan, R., Mahmud, S., Yuki, Y., Bobosha, K., Wassie, L., Carrington, M., et al. (2024). Immunopeptidomics informs discovery and delivery of *Mycobacterium tuberculosis* MHC-II antigens for vaccine design. bioRxiv. 10.1101/2024.10.02.616386.
236. Leddy, O., White, F.M., and Bryson, B.D. (2023). Immunopeptidomics reveals determinants of *Mycobacterium tuberculosis* antigen presentation on MHC class I. Elife *12*. 10.7554/eLife.84070.
237. Bian, Y., Shang, S., Siddiqui, S., Zhao, J., Joosten, S.A., Ottenhoff, T.H.M., Cantor, H., and Wang, C.R. (2017). MHC Ib molecule Qa-1 presents Mycobacterium tuberculosis peptide antigens to CD8+ T cells and contributes to protection against infection. PLoS Pathog *13*, e1006384. 10.1371/journal.ppat.1006384.
238. Caccamo, N., Pietra, G., Sullivan, L.C., Brooks, A.G., Prezzemolo, T., La Manna, M.P., Di Liberto, D., Joosten, S.A., van Meijgaarden, K.E., Di Carlo, P., et al. (2015). Human CD8 T lymphocytes recognize Mycobacterium tuberculosis antigens presented by HLA-E during active tuberculosis and express type 2 cytokines. Eur J Immunol *45*, 1069-1081. 10.1002/eji.201445193.
239. Prezzemolo, T., van Meijgaarden, K.E., Franken, K.L.M.C., Caccamo, N., Dieli, F., Ottenhoff, T.H.M., and Joosten, S.A. (2018). Detailed characterization of human Mycobacterium tuberculosis specific HLA-E restricted CD8. Eur J Immunol *48*, 293-305. 10.1002/eji.201747184.
240. Paterson, R.L., La Manna, M.P., Arena De Souza, V., Walker, A., Gibbs-Howe, D., Kulkarni, R., Fergusson, J.R., Mulakkal, N.C., Monteiro, M., Bunjobpol, W., et al. (2024). An HLA-E-targeted TCR bispecific molecule redirects T cell immunity against Mycobacterium tuberculosis. Proc Natl Acad Sci U S A *121*, e2318003121. 10.1073/pnas.2318003121.
241. Vander Lugt, B., Khan, A.A., Hackney, J.A., Agrawal, S., Lesch, J., Zhou, M., Lee, W.P., Park, S., Xu, M., DeVoss, J., et al. (2014). Transcriptional programming of dendritic cells for enhanced MHC class II antigen presentation. Nat Immunol *15*, 161-167. 10.1038/ni.2795.
242. Bajaña, S., Turner, S., Paul, J., Ainsua-Enrich, E., and Kovats, S. (2016). IRF4 and IRF8 Act in CD11c+ Cells To Regulate Terminal Differentiation of Lung Tissue Dendritic Cells. J Immunol *196*, 1666-1677. 10.4049/jimmunol.1501870.
243. Bosteels, C., Neyt, K., Vanheerswynghels, M., van Helden, M.J., Sichien, D., Debeuf, N., De Prijck, S., Bosteels, V., Vandamme, N., Martens, L., et al. (2020). Inflammatory Type 2 cDCs Acquire Features of cDC1s and Macrophages to Orchestrate Immunity to Respiratory Virus Infection. Immunity *52*, 1039-1056.e1039. 10.1016/j.immuni.2020.04.005.
244. Paterson, R.L., La Manna, M.P., Arena De Souza, V., Walker, A., Gibbs-Howe, D., Kulkarni, R., Fergusson, J.R., Mulakkal, N.C., Monteiro, M., Bunjobpol, W., et al.

(2024). An HLA-E-targeted TCR bispecific molecule redirects T cell immunity against Mycobacterium tuberculosis. Proc Natl Acad Sci U S A *121*, e2318003121. 10.1073/pnas.2318003121.

245. Joosten, S.A., Ottenhoff, T.H.M., Lewinsohn, D.M., Hoft, D.F., Moody, D.B., Seshadri, C., and Collaboration for Tuberculosis Vaccine Discovery - Donor-Unrestricted T-cells Working Group, B.l.a.M.G.F. (2019). Harnessing donor unrestricted T-cells for new vaccines against tuberculosis. Vaccine *37*, 3022-3030. 10.1016/j.vaccine.2019.04.050.
246. Maerz, M.D., Makatsa, M.S., Bucsan, A.N., Sutton, M.S., Bishop, E., Tian, Z., Layton, E.D., Roederer, M., Shalek, A.K., Seder, R.A., et al. (2026). BCG vaccination induces antibacterial effector functions among Vδ1/3 T cells that are associated with protection against tuberculosis. Cell Rep Med *7*, 102536. 10.1016/j.xcrm.2025.102536.
247. Rawat, K., Tewari, A., Li, X., Mara, A.B., King, W.T., Gibbings, S.L., Nnam, C.F., Kolling, F.W., Lambrecht, B.N., and Jakubzick, C.V. (2023). CCL5-producing migratory dendritic cells guide CCR5+ monocytes into the draining lymph nodes. J Exp Med *220*. 10.1084/jem.20222129.
248. León, B., and Ardavín, C. (2008). Monocyte migration to inflamed skin and lymph nodes is differentially controlled by L-selectin and PSGL-1. Blood *111*, 3126-3130. 10.1182/blood-2007-07-100610.
249. Tsai, C.Y., Oo, M., Peh, J.H., Yeo, B.C.M., Aptekmann, A., Lee, B., Liu, J.J.J., Tsao, W.S., Dick, T., Fink, K., and Gengenbacher, M. (2024). Splenic marginal zone B cells restrict Mycobacterium tuberculosis infection by shaping the cytokine pattern and cell-mediated immunity. Cell Rep *43*, 114426. 10.1016/j.celrep.2024.114426.
250. Ahmed, M., Das, S., Rosa, B.A., Rangel Moreno, J., Kaushal, D., Mitreva, M., and Khader, S.A. (2026). Targeting the lung innate pathways during tuberculosis can improve vaccine-induced protection via Th17 responses in diversity outbred mice. mBio, e0323225. 10.1128/mbio.03232-25.
251. TBVAC-HORIZON (2024). Improving understanding of lung immunity in tuberculosis to establish a diverse, innovative TB vaccine pipeline targeting mucosal immunity.
252. Ramanujam, H., Nesakumar, M., Thiruvengadam, K., Kannan, R., Palanisamy, S., Shanmugam, S., and Palaniyandi, K. (2025). Identification of non-tuberculous mycobacteria in slaughtered cattle from Chennai, India. Tuberculosis (Edinb) *154*, 102673. 10.1016/j.tube.2025.102673.
253. Dhama, K., Mahendran, M., Tiwari, R., Dayal Singh, S., Kumar, D., Singh, S., and Sawant, P.M. (2011). Tuberculosis in Birds: Insights into the Mycobacterium avium Infections. Vet Med Int *2011*, 712369. 10.4061/2011/712369.
254. Mulder, K., Patel, A.A., Kong, W.T., Piot, C., Halitzki, E., Dunsmore, G., Khalilnezhad, S., Irac, S.E., Dubuisson, A., Chevrier, M., et al. (2021). Cross-tissue single-cell landscape of human monocytes and macrophages in health and disease. Immunity *54*, 1883-1900.e1885. 10.1016/j.immuni.2021.07.007.
255. Teles, R.M.B., Benabdessalem, C., Perrie, J., Wei, C., West, J., de Andrade Silva, B.J., Andrade, P.R., Mansky, L., Divakar, P., Fischbacher, L., et al. (2025). Spatial profiling reveals TREM2+ macrophages as central to Mycobacterium tuberculosis

pathogenesis in human pulmonary tuberculosis. bioRxiv. 10.1101/2025.07.15.664002.